INVESTIGATION OF INERTIAL PARTICLE SEPERATORS FROM A BROADER PERSPECTIVE

A THESIS SUBMITTED TO
THE GRADUATE SCHOOL OF NATURAL AND APPLIED SCIENCES
OF
MIDDLE EAST TECHNICAL UNIVERSITY

BY

ABDURRAHMAN BURAK DALDAL

IN PARTIAL FULFILLMENT OF THE REQUIREMENTS
FOR
THE DEGREE OF MASTER OF SCIENCE
IN
AEROSPACE ENGINEERING

JANUARY 2023

Approval of the thesis:

INVESTIGATION OF INERTIAL PARTICLE SEPERATORS FROM A BROADER PERSPECTIVE

submitted by **ABDURRAHMAN BURAK DALDAL** in partial fulfillment of the requirements for the degree of **Master of Science** i**n Aerospace Engineering, Middle East Technical University** by,

Prof. Dr. Halil Kalıpçılar
Dean, Graduate School of **Natural and Applied Sciences**

Prof. Dr. Serkan Özgen
Head of the Department, **Aerospace Engineering**

Prof. Dr. Sinan Eyi
Supervisor, **Aerospace Engineering, METU**

Examining Committee Members:

Prof. Dr. Serkan ÖZGEN
Head of Aerospace Engineering, METU

Prof. Dr. Sinan EYİ
Supervisor, Aerospace Engineering, METU

Assoc. Prof. Dr. Nilay SEZER UZOL
Aerospace Engineering, METU

Asst. Prof. Dr. Mustafa PERÇİN
Aerospace Engineering, METU

Asst. Prof. Dr. Sıtkı USLU
Mechanical Engineering, TOBB ETU

Date: 06.01.2023

I hereby declare that all information in this document has been obtained and presented in accordance with academic rules and ethical conduct. I also declare that, as required by these rules and conduct, I have fully cited and referenced all material and results that are not original to this work.

Name Last name : Abdurrahman Burak Daldal

Signature :

ABSTRACT

INVESTIGATION OF INERTIAL PARTICLE SEPERATORS FROM A BROADER PERSPECTIVE

Daldal, Abdurrahman Burak
Master of Science, Aerospace Engineering
Supervisor : Prof. Dr. Sinan Eyi

January 2023, 89 pages

Inertial particle separator (IPS) is an engine integrated device to provide protection for foreign objects such as sand, dust etc. Due to the fact that IPS performance has a direct impact on the engine life, accurate estimation of separation efficiency becomes more important. When an engine is installed on a helicopter, it requires an intake system and aerodynamic characteristics of the incoming flow of the IPS changes significantly according to the intake system design. In this study, intake effect on IPS performance is investigated with the method that provides the most accurate results in the literature which uses unsteady approach and IDDES turbulence model. Results show that swirling flow which is formed due to the intake system design increases the IPS separation performance. The method used in this study requires high computational power and time. However, this kind of power may not be available or this kind of accuracy may not require at the preliminary design stages. For this kind of situations, 2-D approaches and cheaper turbulence models like RANS approach can be used. In the later chapters of this study, RANS turbulence models are investigated for 2-D IPS model. Lag Elliptic Blending k-ε turbulence model provide better results than Spalart-Allmaras, SST k-ω and Realizable k-ε turbulence models but, there is still significant error. A fine-tuning study is performed to increase the accuracy level. $C_{\varepsilon 1}, C_{\varepsilon 2}, \sigma_k$ and σ_ε closure coefficients are tuned and a new set of closure coefficients are obtained with a 24% performance improvement.

Keywords: Annular Inertial Particle Separator Efficiency, Lagrangian Method, Detached Eddy Simulation Turbulence Model, Lag Elliptic Blending Turbulence Model, Turbulence Model Fine-Tuning.

ÖZ

ATALETSEL PARÇACIK AYRIŞTIRICISININ DAHA GENİŞ BİR PERSPEKTİFTEN İNCELENMESİ

Daldal, Abdurrahman Burak
Yüksek Lisans, Havacılık ve Uzay Mühendisliği
Tez Yöneticisi: Prof. Dr. Sinan Eyi

Ocak 2023, 89 sayfa

Ataletsel parçacık ayrıştırıcı (APA), motora entegre olan, kum, toz gibi yabancı maddelere karşı koruma sağlayan bir cihazdır. APA performansının motor ömrü üzerinde doğrudan bir etkiye sahip olması nedeniyle, ayırma verimliliğinin doğru bir şekilde tahmin edilmesi daha önemli hale gelir. Bir motor helikoptere takıldığı zaman uygun bir hava alığına ihtiyaç duymaktadır ve motora giren havanın akış karakteristiği bu hava alığı tasarımına göre önemli ölçüde değişiklik gösterir. Bu çalışmada, hava alığının APA performansına etkisi, IDDES türbülans modelini kullanan ve zamandan bağımsız denklemler çözülerek uygulanan ve literatürde bulunan en doğru yöntem olarak bilinen yöntemle incelenmiştir. Sonuçlar hava alığı sistemi tasarımından dolayı oluşan girdaplı akışın APA performansını artırdığını göstermektedir. Bu analizde kullanılan yöntem yüksek hesaplama gücü ve zaman gerektirmektedir. Ancak bu tür bir güç mevcut olmayabilir veya ön tasarım aşamalarında bu tür bir doğruluk seviyesi gerekmeyebilir. Bu tür durumlarda, iki boyutlu yaklaşım ve daha ucuz olan RANS tabanlı türbülans modelleri kullanılabilir. Bu çalışmanın sonraki bölümlerinde iki boyutlu APA modeli RANS tabanlı türbülans modelleri ile incelenmiştir. Lag Elliptic Blending k-ε türbülans modeli, Spalart-Allmaras, SST k-ω and Realizable k-ε türbülans modellerine göre daha iyi sonuç vermiştir. Ancak sonuçlarda hala bir miktar hata bulunmaktadır. Doğruluk payını artırmak amacıyla türbülans modeline ince ayar çalışması yapılmıştır. Bu çalışmada, $C_{\varepsilon 1}, C_{\varepsilon 2}, \sigma_k$ and σ_ε model katsayıları ayarlanmış ve yeni bir katsayı seti oluşturulmuştur. Bu setle yapılan analiz sonuçlarında 24% oranında iyileştirme elde edilmiştir.

Anahtar Kelimeler: Dairesel Ataletsel Parçacık Ayrıştırma Performansı, Lagrangian Methodu, Detached Eddy Simulation Türbülans Modeli, Lag Elliptic Blending k-ε Türbülans Modeli, Model Katsayısı İnce Ayar.

To My Darkest Night.

ACKNOWLEDGMENTS

First of all, I would like to thank my adviser Prof. Dr. Sinan Eyi for his patience, guidance and support throughout this study. I would also thank to my family Fatih Daldal, Gülseren Daldal, A. Buğra Daldal and G. Alperen Daldal for their spiritual support.

I would specially thank to Emre Sancar, who is not only a colleague but also a friend, for his technical and mental support. I would also thank to my colleagues and friends for their friendship, support and inspiring technical discussions. I also want to express my deepest gratitude to my superiors, İ. Ozan Sert, Kerem Denk, Gökhan Aslan, A. Alper Ezertaş and Yüksel Ortakaya for their guidance, encouragements and supports.

Finally, I want to dedicate this study to my love and my wife M. Leyla Daldal for her endless love and support.

This work is supported by Turkish Aerospace. Software that require any license and high performance cluster are provided by Turkish Aerospace.

TABLE OF CONTENTS

CHAPTERS

APPENDICES

LIST OF TABLES

TABLES

LIST OF FIGURES

FIGURES

LIST OF ABBREVIATIONS

APU	Auxiliary Power Unit
CFD	Computational Fluid Dynamics
DES	Detached Eddy Simulation
DOE	Design of Experiment
EAPS	Engine Advanced Protection Systems
FOD	Foreign Object Damage
IBF	Inlet Barrier Filter
IDDES	Improved Delayed Detached Eddy Simulation
IPS	Inertial Particle Separator
ISG	Inner Surface Geometry
LEB KE	Lag Elliptic Blending k-ε
LWC	Liquid Water Content
MP-PIV	Multi-Phase Particle Image Velocimetry
MVD	Mean Volumetric Diameter
OSG	Outer Surface Geometry
PIV	Particle Image Velocimetry
RANS	Reynolds-Averaged Navier-Stokes
RKE	Realizable k-ε
RST	Reynolds Stress Transport
SA	Spalart-Allmaras
SFC	Specific Fuel Consumption
SST	Shear Stress Transport k-ω
VTS	Vortex Tube Systems

LIST OF SYMBOLS

Symbols

A	area
C_d	drag coefficient
d	diameter
E	total energy per unit mass
e	restitution coefficient
F_1, F_2	blending function for k-ω turbulence model
F_b	body force per unit volume
f_{v1}	damping function for Spalart-Allmaras turbulence model
f_μ	damping function for k-ε turbulence model
$\boldsymbol{I}$	identity tensor
k	turbulent kinetic energy
L	turbulent length scale
$\dot{m}$	mass flow rate
n	decay exponent
p	pressure
P	production term
$\boldsymbol{q}$	heat flux vector
Re	Reynolds number
St	Stokes number
S	mean strain rate tensor
$\boldsymbol{T}$	viscous stress tensor
T	temperature
U_x	axial velocity component
U_θ	circumferential velocity component
v_s	particle slip velocity
$\tilde{\nu}$	modified diffusivity
$\mathbf{V}/\mathbf{U}$	velocity vector

Greek

α	blending function for LEB k-ε turbulence model
α	swirl angle
β	scavenge to core flow ratio
ε	turbulent dissipation rate
μ	dynamic viscosity
κ	Von-Karman constant
ρ	density
φ	normalized wall-normal stress component
ω	specific dissipation rate
ϕ	flow variable
$\boldsymbol{\sigma}$	stress tensor
C_μ	k-ε turbulence model coefficients
$C_{\varepsilon 1}$, $C_{\varepsilon 2}$	
σ_k, σ_ε, α_1	
α_1, α_2	SST k-ω turbulence model coefficients
β_1, β_2, β^*	
$\sigma_{\omega 1}$, $\sigma_{\omega 2}$,	
σ_{k1}, σ_{k2}	
σ, c_{v1}	Spalart-Allmaras turbulence model coefficients
c_{w2}, c_{w3}	
c_{t3}, c_{t4}	
c_{b1}, c_{b2}	
σ_k, σ_ε, σ_φ	Lag Elliptic Blending k-ε turbulence model coefficients
$C_{\varepsilon 1}$, $C_{\varepsilon 2}$, $C_{\varepsilon 2}^*$	
C_1, C_1^*, C_{p3}	
C_3^*, C_4, C_5	
C_μ, C_η, C_L	

Subscripts

0	ambient value
1	incoming component
2	reflected component
2-D	two dimensional
3-D	three dimensional
n	normal
p	particle
t	turbulent/tangential
x	axial component
θ	circumferential component

Superscripts

$\overline{\blacksquare}$	mean term
$\blacksquare'$	fluctuating term
$\widetilde{\blacksquare}$	filtered term
$\widetilde{\blacksquare'}$	sub-filtered term

CHAPTER 1

OVERVIEW

1.1 Background

In many engineering applications, there are numerous undesirable objects known as ‘Foreign Objects’ because of their dangerous effects. Dust, sand, stone, salt spray, bird, ice, snow, and metal part are common examples of foreign objects for air vehicles. Especially sand and dust are two of the foreign object sources, which are responsible from erosion due to large number of dangerous operation areas.

These areas create one of the most dangerous condition which is called as “brownout condition” for a helicopter. An example of a brownout condition is shown in Figure 1.1.

Figure 1.1. CH-53 helicopter in brownout condition. [1]

Brownout condition occurs during take-off, landing and hover in ground effect operations in dusty terrains. Helicopter rotor creates downwash, which interacts with the ground and causes dust clouds surrounding the helicopter. A simple representation of the dust cloud is illustrated in Figure 1.2.

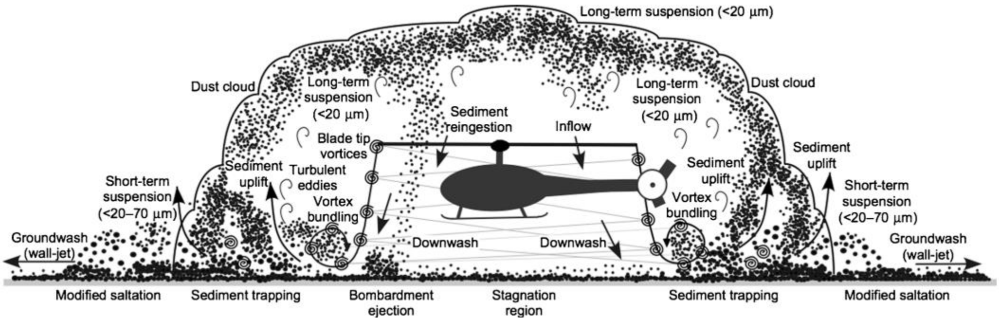

Figure 1.2. Representation of the dust cloud at brownout condition. [4]

One of the most affected part of the helicopter due to these dust clouds is turbine engine. Air demand of the turbine engine is increased during the take-off and landing operations. Even at idle condition, where rotor downwash effect is minimum, dust contaminant still exists within the minimum required amount of air, which is delivered to the engine. As the engine is operating in the dust cloud, engine suction leads to ingestion of the sand/dust particles.

When a foreign object is ingested by a turbine engine, it encounters with the compressor section at first. For this reason, the most affected part of the engines is the first stage of compressor section [2]. Shape of the compressor blades can be deformed due to sand ingestion as presented in Figure 1.3.

Figure 1.3. Damaged compressor blades. [3]

Ingested sand/dust particles reach combustor and they melt immediately due to high temperature. These molten particles impinge on the combustor walls and turbine blades. At the end, these impinged particles can distort the shape of the turbine blades and cause clogging the turbine cooling passages. Its example is shown in Figure 1.4.

Figure 1.4. Molten impurities on turbine blades. [4]

Because of the deformed shapes, flow characteristics in the compressor changes. It results not only with reduced engine power and increased SFC but also reduced lifetime of the related engine sections. For these reason, helicopter engines are equipped with advanced separator systems such as inertial particle separators (IPS), which is the main subject of this study, vortex tube systems (VTS) and inlet barrier filters (IBF) to protect their components.

1.2 The Motivation

IPS is one of the engine protection system, which is integrated to the engine inlet. It separates the dust, sand, rain and another foreign object before they reach the compressor section. When an engine is installed on a helicopter, a proper intake system is needed and it is designed by airframe manufacturer. Aerodynamics of the incoming flow into the engine varies according to the intake system design. In parallel with this variation, particle separation performance of the IPS is going to be different.

The incoming air quality affected by intake design is measured by several parameters, which are pressure recovery, distortion and swirl. These parameters affect the IPS efficiency by changing the incoming flow properties. Swirl effect will be the main consideration of this study. Compressor rotation, helicopter attitudes (sideslip and pitch angle), rotor interactions and gust affect the swirl type (bulk, twin and offset swirl), angle, and direction in conjunction with the intake design. In the literature, all studies assume that the incoming flow to the IPS is uniform and straight; however, this is not true for installed engines.

Significant amount of experiments and computational studies have performed for both two and three-dimensional IPS geometries; however, intake effects have not studied yet. There are only a few studies analyzing vaned type IPS where artificial swirl effect is created with guide vanes before bifurcation and de-swirling the core flow. When even vaned type IPS is integrated to the helicopter, aerodynamics characteristics of the guide vanes will be changed due to the swirling incoming flow, which is related with the intake system design.

IPS performance has a direct impact on the engine life. If separation efficiency of an EAPS increases from 85% to 92%, engine life increases 10 times [5]. Maintenance and inspection intervals of the several engine sections depend on the IPS efficiency. Keeping the time between inspections/maintenance operations shorter brings loss of time, supplies and money. However, keeping it longer may results with loss of equipment or even loss of aircraft. The motivation of this work is minimizing the losses in a safe condition and increasing the engine life.

1.3 Objectives

This thesis presents a look from a broad perspective to the IPS investigations. All studies in the open literature investigate isolated IPS geometry; however, this dissertation examines the performance of the IPS when it is installed on a helicopter.

The main objectives of this study are listed below:

1. Performing validation study of the CFD model for both air and particle flows and analyze 3-D axisymmetric IPS geometry with and without intake effects.

This objective will provide more information about engine life. When engine life simulations/calculations are performed, particle trajectories are used. Particle trajectories will be affected by the intake design. Hence, more realistic deformation calculations can be performed. It is important to note that 3-D axisymmetric IPS geometry will be investigated for the first time with the method that provides the most accurate results in the literature, which uses IDDES turbulence model and Lagrangian method.

2. Investigating the RANS turbulence models and conducting a fine-tuning study for 2-D IPS flow, which has highly adverse pressure gradients.

High fidelity turbulence models like LES/DES require a lot of computational power and promise higher accuracy than RANS turbulence models. If a project is in a preliminary design process, a lot of geometry should be investigated. However, this amount of computational power may not be available or it may not required at this level. Both RANS based turbulence models and 2-D approach can be used for this kind of design process. These approaches are commonly used in the literature and industry. They provide less accuracy; however, it can be improved by using new approaches such as fine-tuning the turbulence model.

CHAPTER 2

INTAKE EFFECTS INVESTIGATION ON IPS PERFORMANCE

2.1 Introduction

As it mentioned in the Background section, compressor is the first critical element of an engine and it is exposed to foreign object damage at most according to the other engine sections. Crucial parts of the engine like compressor, combustor and turbine are negatively affected regarding to foreign object damage. Sand and dust are the two common foreign object debris for helicopters due to severe operational environments. Shorter engine life, reduced engine power and increase in maintenance operations are common outcomes for helicopters operating in the harsh environments. Hence, intake must be protected to prolong the engine lifetime and to reduce the operational and maintenance costs.

There are several protection systems for helicopter engines and these systems are generally known as engine advanced protection systems (EAPS). Vortex tube systems, inlet barrier filters and inertial particle separators are three well-known examples for EAPS. Vortex tube systems and inlet barrier filters are external equipment for helicopters; however, inertial particle separators are integrated in the turboshaft engine. In this chapter, a brief information is given for VTS and IBF. Only IPS is investigated in details.

2.1.1 Vortex Tube System (VTS)

The first protection system is vortex tube systems, which separate particles by using centrifugal force. As it can be seen from Figure 2.1, dirty air is coming into the vortex tube and it starts to rotate as it encounters the vortex generator. Particles with higher inertia will be subject to higher centrifugal force and their movement is dominated by bouncing on tube walls. Hence larger particles moves towards the outer wall of the tube. In this process, dirty air leaves the tube from the scavenge outlet and sand/dust particles are collected in a zone, which is between outlet and inlet tube plates, and ejected from the system by the help of a scavenge fan or bleed air connected to this zone. Particles with lower inertia will be subject to lower centrifugal force and their movement is dominated by drag force. Hence, clean air and smaller particles moves center of the tube and engine core.

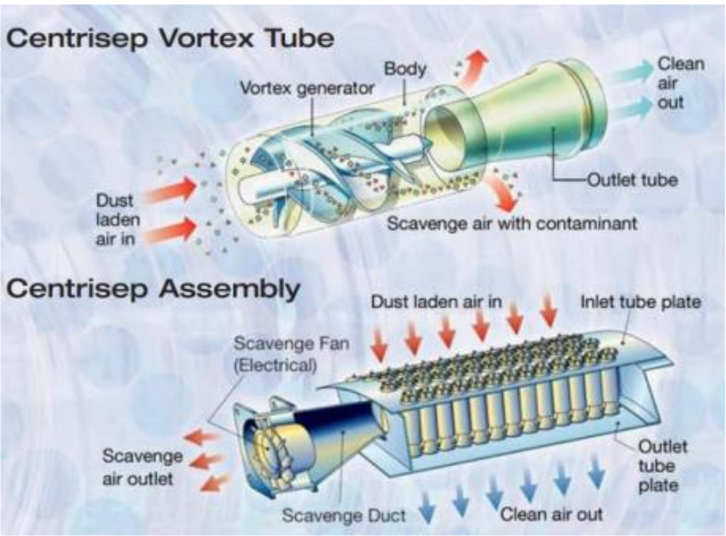

Figure 2.1. Vortex tube system working principle. [6]

A basic example of a vortex tube system, which is designed for Mi-8/17 helicopter intake, is presented in Figure 2.2.

Figure 2.2. Mi-8/17 helicopter intake Vortex tube system. [6, 7]

Vortex tube systems have several advantages. It significantly reduces maintenance costs. It is self-cleaning system and it is generally known as “fit and forget” system. In addition to the dust and sand protection, it provides protection against ice, snow, heavy rain, and salt spray. Pressure loss of the VTS is low due to uniform airflow distribution [7]. Despite its advantages, it has several disadvantages. For example, VTS requires scavenge mass flow as 5-10% of the core mass flow. Bleed air or a fan, which requires electrical power, is used to supply the required scavenge mass flow. It also creates high amount of drag since it is an externally installed device and it requires large area to supply enough mass flow for engine [8]. Moreover, integration is hard due to both structural and aerodynamic interfaces. Sometimes engine intakes need to be able to be inspected for flight safety. For these cases, accessibility of the intake must be easy and a mechanism might be needed for this type of requirements.

2.1.2 Inlet Barrier Filters (IBF)

The second protection system is inlet barrier filters, which separates particles by using filter elements, which have smaller gaps than the particle size on it; hence, only the clean air can pass through the downstream of the IBF. It consists of several components such as wire mesh, pleated filter element, by-pass door, electrical equipment and structural parts for ease of installation and replacement. Figure 2.3 shows IBF components of AS 350 helicopter.

Filter assembly is the main part of the IBF. As dirty air encounters with the filter assembly, which behaves as a physical barrier, particles stop on the filter element and clean air moves into the engine. As time passed by, particles accumulate on the filter element and gaps on the filter element start to fill. In general, IBF has low pressure loss and very high separation efficiency, which reaches up to 99.3% [4]. Accumulation on the filter element increases separation efficiency; however, having higher separation efficiency brings some disadvantages such as pressure loss. Pilot controlled by-pass door is need to be opened if pressure loss reached to a critical value. When by-pass door is opened, engine becomes vulnerable to foreign object damage.

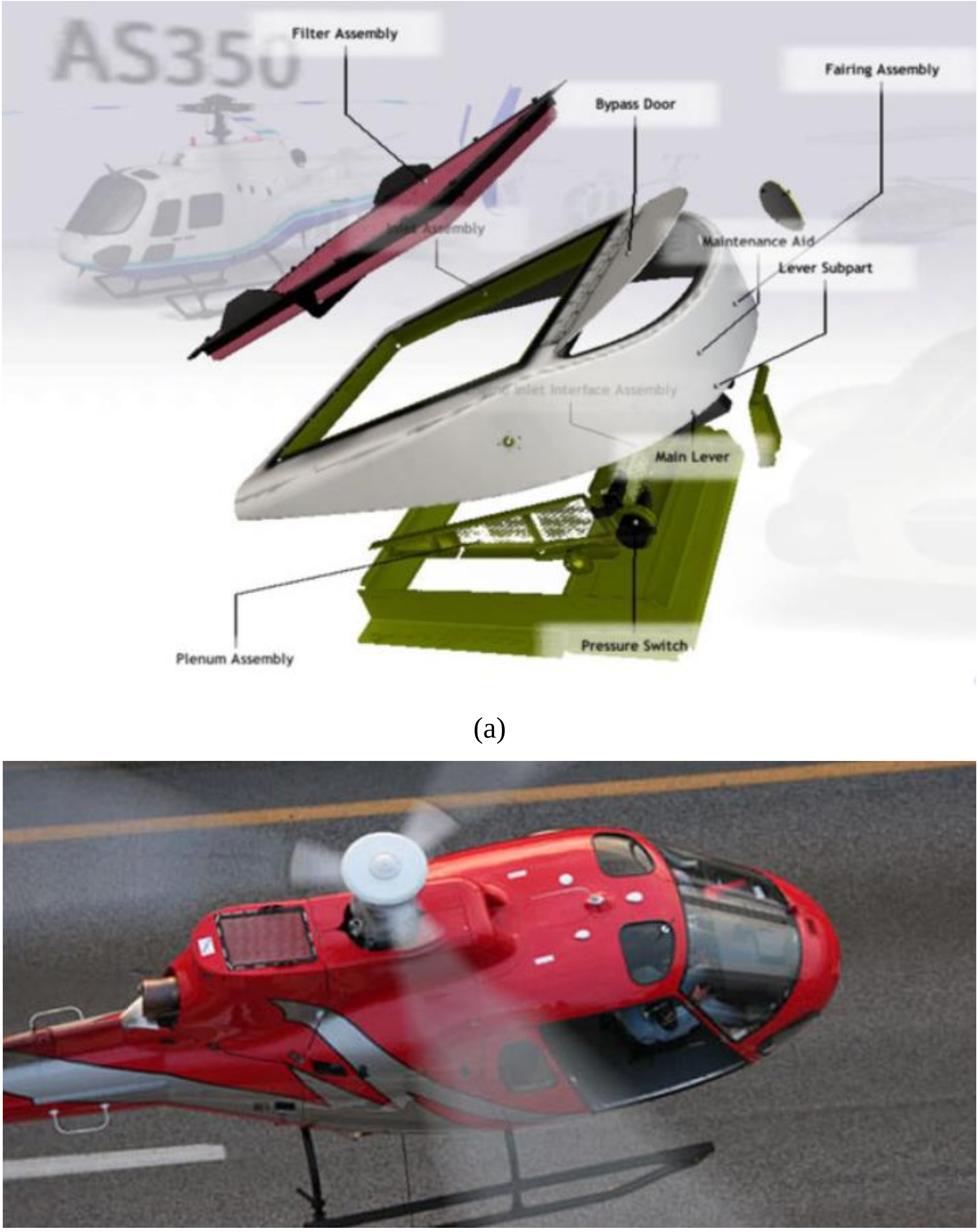

(a)

(b)

Figure 2.3. IBF components (a) and installation (b) on Eurocopter AS 350 helicopter. [9, 10]

One of the other disadvantages of the IBF is integration issues. IBF requires large surface area due to its nature of the separation technique to reduce pressure loss. If IBF is integrated on a helicopter as an external equipment, it creates high drag to satisfy the intake requirements. One of the example of this type of installation is shown in Figure 2.4.

Figure 2.4. H-60 Black Hawk Helicopter IBF system. [11]

In addition to the high separation efficiency, IBF has more advantages. It does not require any scavenge flow for particle separation unlike VTS. Moreover, IBF creates less distorted flow for intake. [4]

2.1.3 Inertial Particle Separators (IPS)

Inertial particle separator (IPS) is the last protection system and the main subject of this study; hence, it will be investigated in details. It uses a similar method of the VTS to separate particles. A simple representation of an IPS cross-section is shown in Figure 2.5.

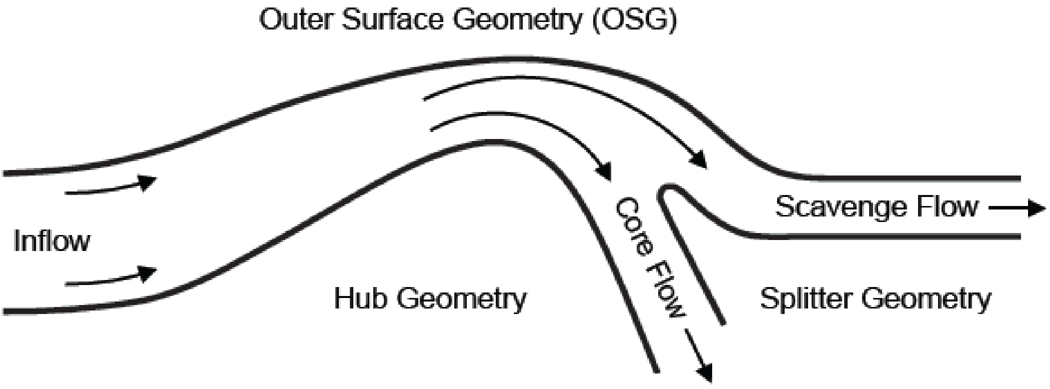

Figure 2.5. Inertial Particle Separator cross-section. [12]

IPS is a device located at the frontmost of an engine which provides protection by deflecting both air and particle flows outward direction, where dust/sand particles, which have higher inertia, move into the scavenge duct and air, which has lower inertia, turns back to the core engine. Scavenge flow is derived with a fan; hence, some part of the incoming air evacuated with the particles. The ratio of the scavenge mass flow and incoming mass flow is defined as β and it is given in Equation 1

$$\beta = \frac{\dot{m}_{\text{scavenge}}}{\dot{m}_{\text{scavenge}} + \dot{m}_{\text{core}}} \tag{1}$$

Increasing the β, increases the scavenge flow and separation performance. However, this situation yields to the increased electrical power demand for scavenge fan and lower engine performance due to lower ram recovery. Separation efficiency of an IPS can reach up to 94% when scavenge fan is active [13]. IPS is an integrated system of an engine and it brings several advantages such as compactness, low external drag, and low pressure loss with high separation efficiency. Despite of these advantages, IPS has several disadvantages. It requires electrical power to drive scavenge fan and it has lower separation efficiency compared to the VTS and IBF. An example of an IPS on T700 engine is presented in Figure 2.6. IPS blower is marked with red rectangle and IPS scroll, where particles move after scavenge duct, is marked with blue rectangle.

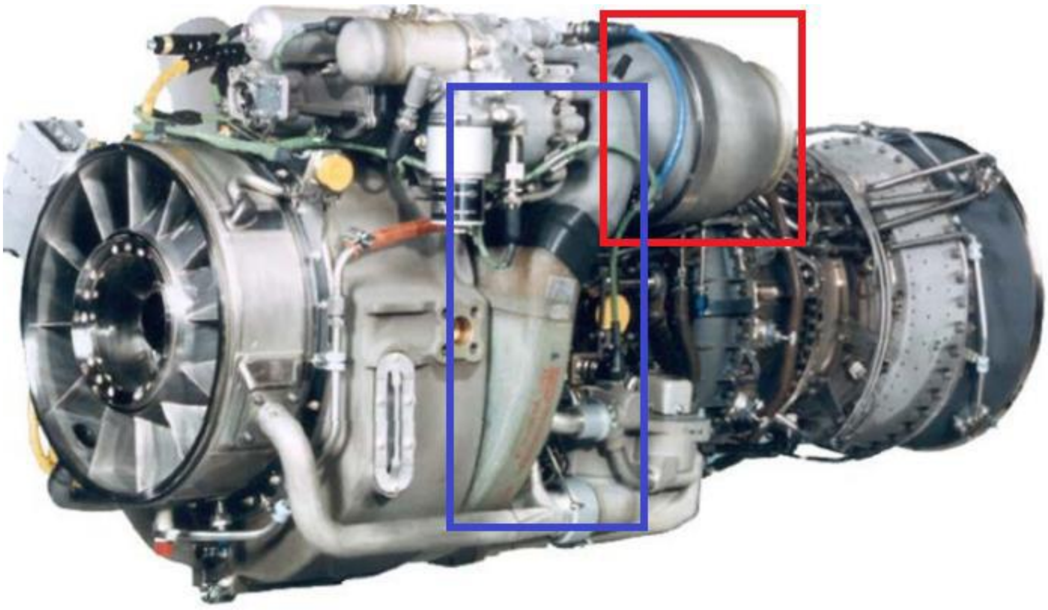

Figure 2.6. T700 engine IPS [4]

IPS performance is studied with experimentally and computationally in literature. While there are few experimental studies on this topic, computational studies are more common due to lower costs. Firstly, previous experimental studies are investigated about IPS.

- <u>Previous Experimental Studies:</u>

Vittal *et al.* [14] performed one of the oldest experimental study for a vaneless type IPS that has lower pressure loss, cost and weight than the vaned type IPS. Particle separation efficiency and pressure loss are investigated during tests for vaneless type IPS. It is concluded that 85% separation efficiency can be obtained by using 16% scavenge flow for AC Coarse sand with the low pressure loss.

Barone *et al.* [12, 15-21] performed experimental studies at University of Virginia IPS Research Facility. A planar vaneless type IPS geometry is studied, which is given in Figure 2.5. Outer surface geometry (OSG) of the scavenge duct is examined with varying β to determine the separation efficiency. Particle Image Velocimetry (PIV) and Multi-Phase Particle Image Velocimetry (MP-PIV) are used during experiments to obtain the flow-field and particle trajectories. Unsteady flow characteristics with a huge separation bubble around bifurcating region is observed. It is stated that this separation bubble has an enormous impact on the separation efficiency at low β values.

Connolly *et al.* [22-26] studied the same geometry with Barone *et al.* at the same facility. In addition to the new OSG geometries, inner surface geometry (ISG) of the scavenge duct with varying β is investigated to determine the separation efficiency by using PIV and MP-PIV. Drag force and bounce two important phenomenon that affects particle motion, hence separation efficiency. Connolly did a research on these topics and came up with new bounce and drag model for irregular particles. AC Coarse, C-Spec and AFRL03 test dusts are examined. In addition to the separation bubble that is shown previously in Barone's experiments, a wall normal vortex that blocks the entrance of the scavenge duct is observed.

Chen *et al.* [27] conduct an experiment with 50° section of annular vaneless type IPS. The particles are not included in the experiment and only the flow field is investigated with PIV. Similar results with the Barone and Connolly are obtained during the experiments. Moreover, high scavenge flow ratios up to around 50% are studied and results show that the separation bubbles at the OSG side change position to the hub side. This position change may increase pressure loss through the core side and reduce the available engine power.

Paoli and Wang [28] experimented a vaneless type annular IPS geometry; however, study involves only flow analysis but not the particles. Experiment is performed for several Reynold's number and β values to visualize the flow-filed with the high-speed CCD camera. It is stated that a very similar vortices are observed with similar experiments.

- Previous Computational Studies:

Many computational studies are performed to obtain IPS flow-field and particle trajectories for a long time. One of the oldest studies are conducted by Hamed *et al.* [29, 30] in 1981-93. 2-D, steady CFD analyses of T700 Engine IPS are performed with in-house codes without comparing any experimental data. It is stated that swirling vanes increase separation efficiency of 50-500 μm particles at most.

Ghenaiet *et al.* [31] studied 30° annular IPS section of RTM322 Engine by using TASCflow code. 3-D, steady CFD analyses are performed with RANS approach and particle separation efficiency is investigated for various β and inlet mass flow rates. Moreover, hub, shroud and splitter geometries are manipulated to increase system performance. However, there is not any experimental data to compare the results.

Taslim *et al.* [32, 33] studied 2° annular IPS geometry by using STAR-CD software. 3-D, steady CFD analyses are conducted with several hub geometries. Particle separation efficiency is calculated with AC Coarse, AC Fine and C-Spec sand distributions. Moreover, the effects of particle distribution uniformity at the IPS inlet, particle density and shape factor on separation efficiency are investigated without experimental data.

Smith [34] applied Six-Sigma method to IPS and aimed to find the most important parameters that affects the IPS. An optimization study, which includes 2-D flow analysis and particle trajectory investigations, is performed with a response surface approach to observe performance characteristics such as pressure loss, separation efficiency, IPS length, diameter etc.

Jiang *et al.* [35] performed a numerical study for a twisted IPS geometry by using Fluent solver. 3-D, steady analyses are conducted to investigate the gravity, inlet velocity, shape factor, rebound characteristics and particle diameter effects on separation efficiency performance with the lack of experimental data.

As mentioned before, Paoli and Wang [28] experimented 3-D fully annular IPS geometry; however, numerical study with the same geometry is also performed by using steady approach. Shape modifications are investigated to obtain better performance in terms of pressure loss.

Zhang *et al.* [36] investigated both vaned and vaneless type IPS geometries with AC Coarse sand and C-Spec sand. Several rebound models are compared with the experimental data for both vaned and vaneless type IPS.

As mentioned earlier, Chen *et al.* [27] experimented 50° section of annular IPS. 2-D, axisymmetric CFD analysis with RANS approach is also performed. Only airflow is investigated in the CFD analyses. Results show that CFD overestimates the velocity near wall and underestimates other regions.

Chen *et al.* [37] studied vaneless type IPS geometry for water flow and water impingement with various β values. Eulerian-Eulerian approach is used to simulate the air and water droplets in the CFD analyses. As air assumed to be turbulent where RANS approach is used, water droplets assumed to be laminar. Moreover, cloud properties (LWC, MVD) and incoming flow effects on IPS performance are investigated.

Connolly *et al.* [22-26] performed extensive study to obtain more accurate numerical model for IPS analysis. 3-D, unsteady CFD analysis for a planar IPS geometry is conducted for the first time by using Improved Delayed Detached Eddy Simulation (IDDES) turbulence model. Moreover, particle motion is investigated for various β values with the new bounce and drag model, which is developed by Connolly, to obtain separation efficiency. Results show that re-ingestion of the particles from scavenge duct to the core duct is observed. It is stated that results show a good agreement with the experimental data for both flow-field and particle trajectories. In addition, Connolly studied scaling effects and axisymmetric effects on IPS performance with 2-D geometry by using RANS approach. It is stated that 2-D RANS simulations overestimate the separation efficiency.

The previous studies show that 2-D and 3-D RANS simulations incapable to capture the unsteady effects, which has a large impact on small particles. 3-D, unsteady analysis should be performed with a high fidelity turbulence model to obtain accurate separation efficiency results and flow-field calculations. High fidelity models bring disadvantages like computational cost and required long times to obtain a result; hence, cheaper models are required to get a foresight. Although 2-D RANS simulations give poor performance, it is sufficient for preliminary performance evaluations.

2.2 Methodology

As previously mentioned, Barone and Connolly performed experiments with a planar IPS. A validation study is performed for both airflow and particle trajectory calculations by using these experimental results. The analyzed validation geometry and boundary conditions [22] are given in Figure 2.7.

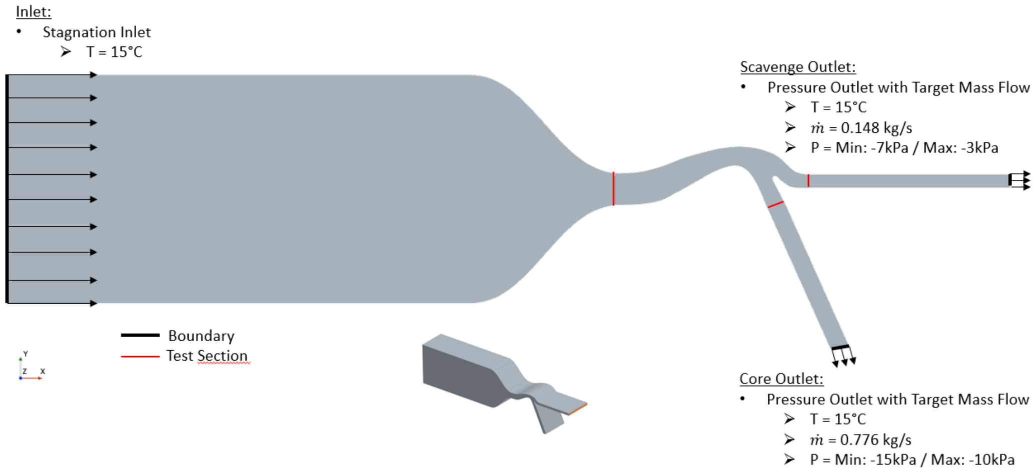

Figure 2.7. Validation geometry and boundary conditions [22]

The geometry shown in Figure 2.7 is used for CFD analysis, but there is a difference between original test and CFD geometry. Inlet and outlets are extruded in boundary normal direction to prevent pressure reflections at the boundaries. The boundary condition of the extruded walls are chosen as slip-wall. Star-CCM+ software is used for CFD analyses. Inlet boundary condition is selected as stagnation inlet with zero Pascal gauge pressure. Core outlet and scavenge outlet boundaries are set as pressure outlet with target mass flow option. Pressure and mass flow rate values given in Figure 2.7 are implemented on these boundaries. Temperature is constant and 15°C at the all boundaries.

Fluid domain is discretized with unstructured polyhedral elements by using the same software. Regarding to the turbulence model, mesh is created by obeying the y+ < 1 law. Mesh study is performed to visualize the solutions independency from the mesh size. Three different meshes are created with 4 million (coarse), 8 million (baseline) and 16 million (fine) elements. Both surface meshes and volume meshes at the mid-section are presented in Figure 2.8.

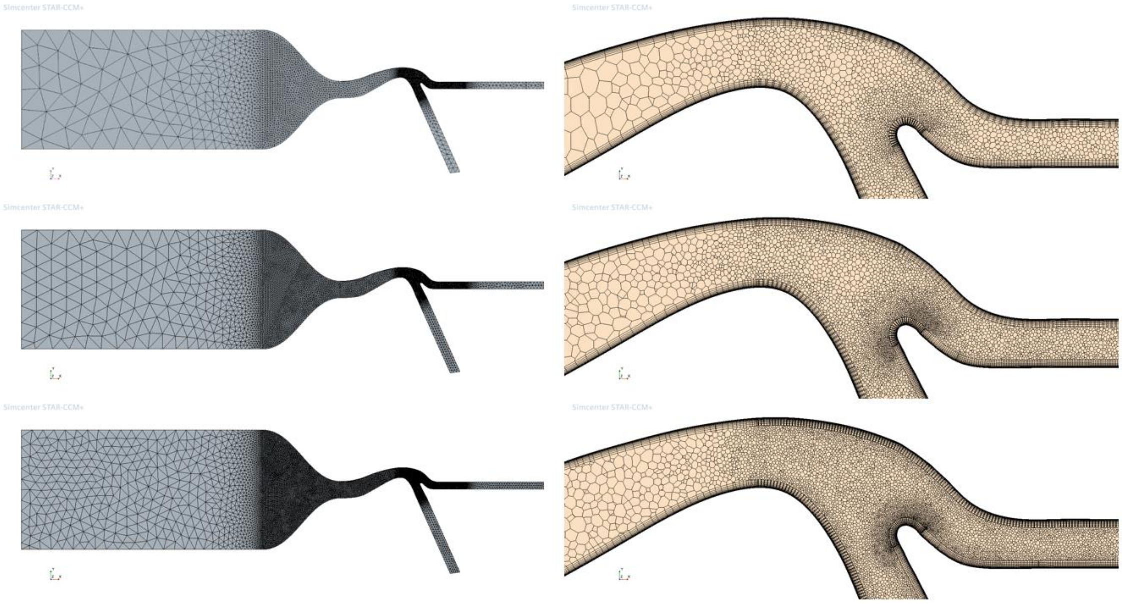

Figure 2.8. Surface mesh (left) and volume mesh at mid-plane (right).

According to the mesh study, since baseline and fine meshes have similar results, baseline mesh is used for flow and particle analysis. Detailed results of the mesh study will be presented in “Result” section.

For this study, analyses are accomplished in three parts which are:

- Steady flow analysis
- Unsteady flow analysis
- Unsteady flow analysis with particle injection

At the first part, analysis is started with the steady approach and it converged in 5000 iterations. Convergence is monitored by checking pressure and mass flow rate values at the core and scavenge outlet boundaries. Coupled implicit flow solver, which solves continuity and momentum conservation equations simultaneously, is used and these equations are presented in Equations 2-4 by including the energy equation. [37] Fluxes are evaluated by using second order upwind discretization scheme. Air is used as material with ideal gas model.

$$\frac{\partial \rho}{\partial t} + \nabla \cdot (\rho \boldsymbol{V}) = 0 \tag{2}$$

$$\frac{\partial (\rho \boldsymbol{V})}{\partial t} + \nabla \cdot (\rho \boldsymbol{V} \times \boldsymbol{V}) = \nabla \cdot \boldsymbol{\sigma} + \boldsymbol{F}_b \tag{3}$$

$$\frac{\partial (\rho E)}{\partial t} + \nabla \cdot (\rho E \boldsymbol{V}) = \boldsymbol{F}_b \cdot \boldsymbol{V} + \nabla \cdot (\boldsymbol{V} \cdot \boldsymbol{\sigma}) - \nabla \cdot \boldsymbol{q} \tag{4}$$

where, ρ is density, $\boldsymbol{V}$ is the velocity vector, $\boldsymbol{\sigma}$ is the stress tensor, $\boldsymbol{F_b}$ is the body force per unit volume, E is the total energy per unit mass and $\boldsymbol{q}$ is the heat flux vector.

Stress tensor can also written as sum of normal and shear stresses.

$$\boldsymbol{\sigma} = -p\boldsymbol{I} + \boldsymbol{T} \tag{5}$$

where, p is the pressure, $\boldsymbol{I}$ is the identity tensor and $\boldsymbol{T}$ is the viscous stress tensor which is given in Eq. 6.

$$\boldsymbol{T}_{RANS} = \begin{pmatrix} \tau_{xx} & \tau_{xy} & \tau_{xz} \\ \tau_{yx} & \tau_{yy} & \tau_{yz} \\ \tau_{zx} & \tau_{zy} & \tau_{zz} \end{pmatrix} \tag{6}$$

Each flow variable, ϕ, (such as velocity, pressure etc.) have mean, $\overline{\phi}$, and fluctuating, ϕ', components as shown in Equation 6.

$$\phi = \overline{\phi} + \phi' \tag{7}$$

Reynolds-Averaged Navier-Stokes equations can be re-written by using the only averaged term and additional modelling the fluctuating term of the flow variables as shown in Equations 7-9.

$$\frac{\partial \rho}{\partial t} + \nabla \cdot \left(\rho \overline{\boldsymbol{V}}\right) = 0 \tag{8}$$

$$\frac{\partial (\rho \overline{\boldsymbol{V}})}{\partial t} + \nabla \cdot \left(\rho \overline{\boldsymbol{V}} \times \overline{\boldsymbol{V}}\right) = -\nabla \cdot \overline{p}\boldsymbol{I} + \nabla \cdot (\overline{\boldsymbol{T}} + \boldsymbol{T}_{\boldsymbol{RANS}}) + \boldsymbol{F}_b \tag{9}$$

$$\frac{\partial (\rho \overline{E})}{\partial t} + \nabla \cdot \left(\rho \overline{E}\, \overline{\boldsymbol{V}}\right) = \nabla \cdot \left(\overline{\boldsymbol{T}} + \boldsymbol{T}_{RANS}\right)\overline{\boldsymbol{V}} + \boldsymbol{F}_b \overline{\boldsymbol{V}} - \nabla \cdot \overline{\boldsymbol{q}} - \nabla \cdot \overline{p}\overline{\boldsymbol{V}} \tag{10}$$

where, variables with overbar used for the mean value and one additional stress tensor $\boldsymbol{T}_{RANS}$ for the modelling of the fluctuating term is added. It is given in Equation 10.

$$\boldsymbol{T}_{RANS} = -\rho \begin{pmatrix} \overline{u'u'} & \overline{u'v'} & \overline{u'w'} \\ \overline{u'v'} & \overline{v'v'} & \overline{v'w'} \\ \overline{u'w'} & \overline{v'w'} & \overline{w'w'} \end{pmatrix} + \frac{2}{3}\rho k \boldsymbol{I} \tag{11}$$

where, k is the turbulent kinetic energy.

These fluctuating terms are modeled in terms of mean flow variables and turbulent viscosity and it is known as Boussinesq approximation. It links the Reynolds stresses with the mean strain rate by using eddy viscosity.

$$\boldsymbol{T}_{RANS} = 2\mu_t \boldsymbol{S} - \frac{2}{3}\left(\mu_t \nabla \cdot \overline{\boldsymbol{V}}\right)\boldsymbol{I} \tag{12}$$

where, μ_t is the turbulent viscosity and $\boldsymbol{S}$ is the mean strain rate tensor.

In this study, turbulence is modeled by using k-ω SST turbulence model with low y+ approach and curvature correction option. In k-ω SST turbulence model, turbulent viscosity is modelled in terms of mean flow variables by solving additional transport equations for kinetic energy and specific dissipation rate.

At the second part, unsteady approach is used for time discretization. Time step is chosen as 5x10^{-6} seconds and 10 inner iterations which sufficient for continuity, three momentum and energy residuals to reach 1x10^{-4}. Additionally, the DES turbulence model is used to model the turbulence. DES is a hybrid model that uses LES at the separated flow regions and it uses RANS at the walls/boundary layers and irrotational regions. In LES turbulence model, a special filter is used to solve the Navier-Stokes (NS) equations. The flow variables have a filtered, $\tilde{\phi}$, and sub-filtered (or sub-grid), ϕ'', components as shown in Equation 12.

$$\phi = \widetilde{\phi} \ + \phi'' \tag{13}$$

Navier-Stokes equations can be re-written by inserting the filtered and sub-filtered variables as shown in Equations 13-15.

$$\frac{\partial \rho}{\partial t} + \nabla \cdot \left(\rho \widetilde{\boldsymbol{V}}\right) = 0 \tag{14}$$

$$\frac{\partial (\rho \widetilde{\boldsymbol{V}})}{\partial t} + \nabla \cdot \left(\rho \widetilde{\boldsymbol{V}} \times \widetilde{\boldsymbol{V}}\right) = -\nabla \cdot \tilde{p} \boldsymbol{I} + \nabla \cdot (\widetilde{\boldsymbol{T}} + \boldsymbol{T_{SGS}}) + \boldsymbol{F}_b \tag{15}$$

$$\frac{\partial (\rho \widetilde{E}\ )}{\partial t} + \nabla \cdot \left(\rho \widetilde{E}\, \widetilde{\boldsymbol{V}}\right) = \nabla \cdot \left(\widetilde{\boldsymbol{T}} + \boldsymbol{T}_{SGS}\right) \widetilde{\boldsymbol{V}} + \boldsymbol{F}_b \widetilde{\boldsymbol{V}} - \nabla \cdot \widetilde{\boldsymbol{q}} - \nabla \cdot \tilde{p} \widetilde{\boldsymbol{V}} \tag{16}$$

where, variables with over-tilde used for the filtered value and one additional stress tensor T_{SGS} for the modelling of the sub-grid scale stress term is added. It is given in Equation 16.

$$\boldsymbol{T}_{SGS} = 2\mu_t \boldsymbol{S} - \frac{2}{3}\left(\mu_t \nabla \cdot \widetilde{\boldsymbol{V}}\right)\boldsymbol{I} \tag{17}$$

As LES requires very fine grid, solver may divert to RANS method due to coarse cells at the separation region. Moreover, if prims layer mesh is refined unnecessarily, solver may diverts from RANS to LES and results with artificial separation. While DDES method differs from DES by adding a delay factor, IDDES method differs from DES by adding dependence on the wall distance for sub-grid length scale to prevent this unrealistic phenomenon. In addition to those changes in models, bounded-central convection discretization scheme, which is recommended for LES is used. This part of the analysis is continued until steady effects disappears which takes approximately 0.03 seconds.

At the last part of the analysis, Lagrangian Multiphase model is activated to analyze particle motion. One-way coupling, where particles are affected by fluid but do not have effects on the fluid flow, is used by assuming particles have negligible impact on the airflow. Particles are modelled as solid glass sphere with constant 2500 kg/m^3 density. Particle diameter is varied from 2µm to 200µm as defined in A4 Coarse Arizona test dust. [38] Pressure gradient force given in Equation 17 and drag force given in Equation 18 are the main forces acting on the particles.

$$\boldsymbol{F_p} = -V_p \nabla p_{static} \tag{18}$$

where V_p is the particle volume and ∇p_{static} is the gradient of the air static pressure.

$$\boldsymbol{F_d} = \frac{1}{2} C_d \rho A_p |\boldsymbol{v_s}| \boldsymbol{v_s} \tag{19}$$

where C_d is the drag coefficient, ρ is the air density, A_p is the projected particle area and $\boldsymbol{v_s}$ is the particle slip velocity. Drag coefficient can be estimated by using Schiller-Naumann correlation, which is suitable for spherical solid particles, and it is given in Equation 19.

$$C_d = \begin{cases} \frac{24}{Re_p}\left(1 + 0.15 Re_p^{0.687}\right) & Re_p \leq 10^3 \\ 0.44 & Re_p > 10^3 \end{cases} \tag{20}$$

where Re_p is defined as particle Reynolds number that is also defined in Equation 20.

$$Re_p = \frac{\rho |\boldsymbol{v_s}| D_p}{\mu} \tag{21}$$

where μ is defined as air dynamic viscosity, D_p is the particle diameter.

One of the main parameter affecting the particle motion is restitution coefficients. Particles leaves the domain if they encounter the outlet boundaries and they bounce if they encounter with a wall boundary. Restitution coefficients define how particles move when they hit the wall boundary. A simple representation of the rebound event is shown in Figure 2.9.

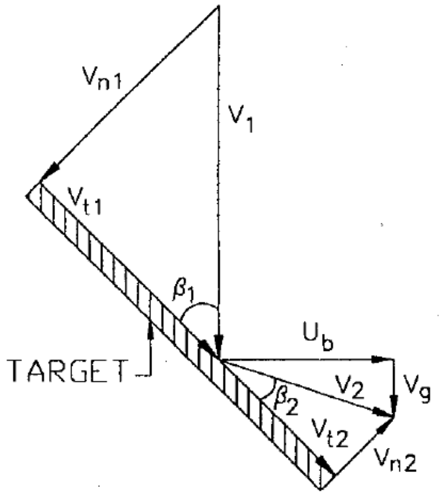

Figure 2.9. Rebound event [42]

There are two coefficients defined as normal and tangential restitution coefficients. Normal restitution coefficient is the ratio of the particle velocity after impact to particle velocity before impact in normal direction and tangential restitution coefficient is the same ratio in tangential direction. These coefficients are presented in Equations 21-22.

$$e_n = \frac{V_{n2}}{V_{n1}} \tag{22}$$

$$e_t = \frac{V_{t2}}{V_{t1}} \tag{23}$$

There are several bounce model that are created with experimental results. Bounce model created by Tabakoff [39, 40], which is given in Equations 23-24 is used in this study. This bounce model is created with AM-355 material with 150μm sand particles where incoming particle velocity is 90.85 m/s.

$$e_v = \frac{V_2}{V_1} = 0.65810 - 0.00877\beta_1 + 0.11954x10^{-3}\beta_1^2 - 7.80954x10^{-7}\beta_1^3 \tag{24}$$

$$e_\beta = \frac{\beta_2}{\beta_1} = 1.68634 - 0.06447\beta_1 + 1.35709x10^{-3}\beta_1^2 - 8.70497x10^{-7}\beta_1^3 \tag{25}$$

Tangential and normal restitution coefficients can be calculated by using Equations 25-27.

$$\beta_2 = \frac{\beta_2}{\beta_1} * \beta_1 \tag{26}$$

$$\frac{V_{n2}}{V_{n1}} = \frac{V_2}{V_1} * \frac{\sin(\beta_2)}{\sin(\beta_1)} \tag{27}$$

$$\frac{V_{t2}}{V_{t1}} = \frac{V_2}{V_1} * \frac{\cos(\beta_2)}{\cos(\beta_1)} \tag{28}$$

The calculated restitution coefficients vary with incoming angle and their result from 5° to 80° is presented in Figure 2.10.

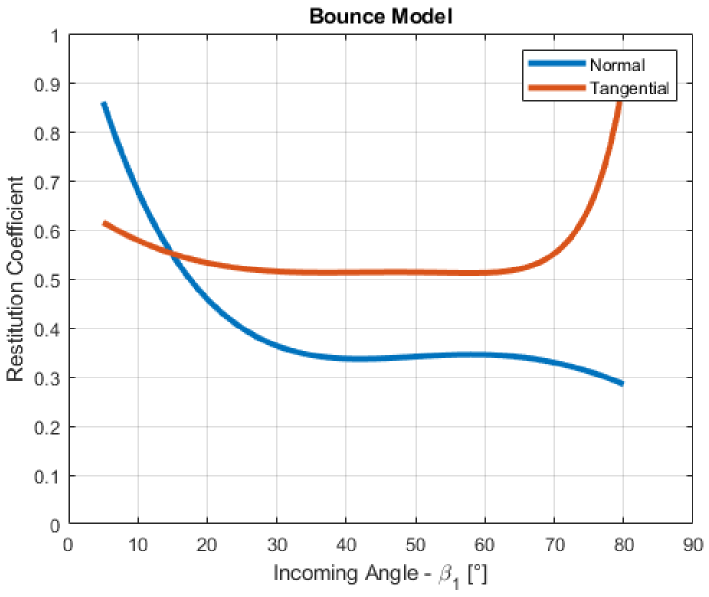

Figure 2.10. Bounce model

When all parameters in the model setup were arranged, particle analysis is started. Particles are released from the entrance of the test section shown in Figure 2.7 with zero initial velocity. Particles are added by using a line probe at the mid-section of the IPS. 10 particles are injected at each time step and particle injection is stopped after 0.006 seconds to reduce computational power. In total, 12,000 particles are injected. Analysis continued until particles leave the flow domain or they are stuck. Increasing the particle number to 40,000 and 120,000 does not affect the separation efficiency results. For each particle size, different analyses are conducted and separation efficiency results are obtained separately. These results are multiplied with a weighting factor [31] and final separation efficiency is calculated.

All the work up to here is used for planar IPS analysis. The same methodology will also be used for the investigation of intake effects. As mentioned in Chapter 1, only swirl effect is investigated at this study.

Swirl can be defined as flow angularity and it is one of the most common phenomenon observed at engine intakes after installation. Swirling flow at the intake may be generated due to several reasons or combination of them. Compressor rotation, intake type, aircraft attitude (angle of attack, sideslip angle etc.), gust and rotor interactions are the parameters affecting the swirl type and swirl angle. There are several swirl types such as bulk swirl, twin swirl and offset swirl. A simple representation of these swirl types are presented in Figure 2.11.

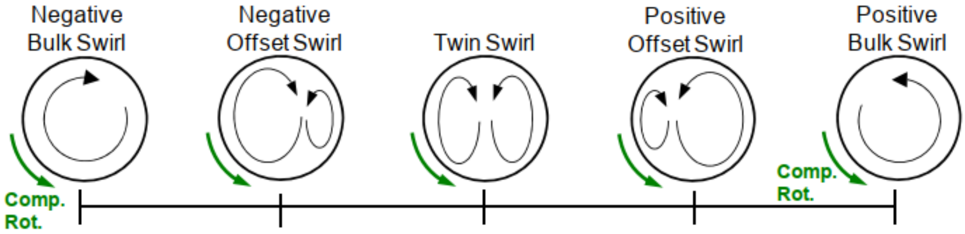

Figure 2.11. Swirl types [41]

If entire flow is rotating in one direction, it is called as bulk swirl. If flow is rotating in two opposite direction with the same magnitude, it is called as twin swirl. If flow is rotating in two opposite direction with different magnitude, it is called as offset swirl. Only bulk swirl will be investigated at this study for ease of modelling.

Swirl angle is defined as the invers tangent of the ratio of circumferential velocity to axial velocity. It is defined as positive if it is in the same direction with the compressor rotation. Swirl angle is given in Equation 28 and illustrated in Figure 2.12.

$$\alpha = \tan^{-1}\left(\frac{\boldsymbol{U_\theta}}{\boldsymbol{U_x}}\right) \tag{29}$$

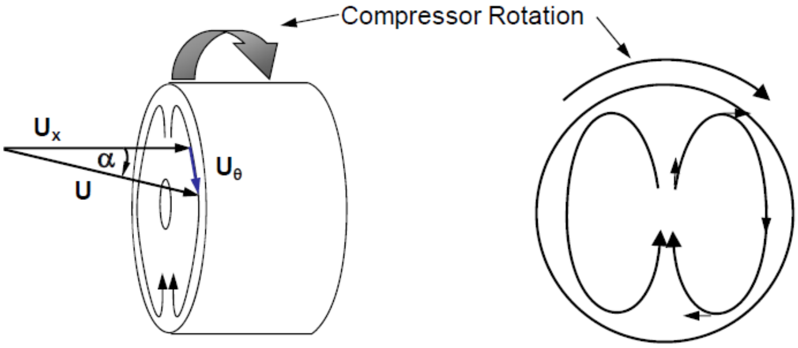

Figure 2.12. Swirl angle [41]

Since planar geometry is not suitable for swirling flow investigation, an annular IPS geometry is needed. A new annular IPS geometry is obtained by revolving the 2-D geometry around the axis of the engine center, where engine radius is 0.5m. The new geometry is created by using Siemens NX software with an effort maintaining the flow field characteristics. For this purpose, core to scavenge area ratio is preserved with the original test geometry. When preserving the area ratio, some necessary geometry modifications such as directing the core leg to the axial direction are accomplished. When core leg is directed in both axial and vertical directions (as in validation geometry), core flow outlet gets closer to the rotation center. Hence, area of the core outlet becomes smaller than the scavenge outlet, where it is vice versa at the original geometry, at the end of the revolving operation. Moreover, in real engines core leg stands in axial direction. At last, intake geometry is simplified and hub, splitter and OSG geometries remain the same.

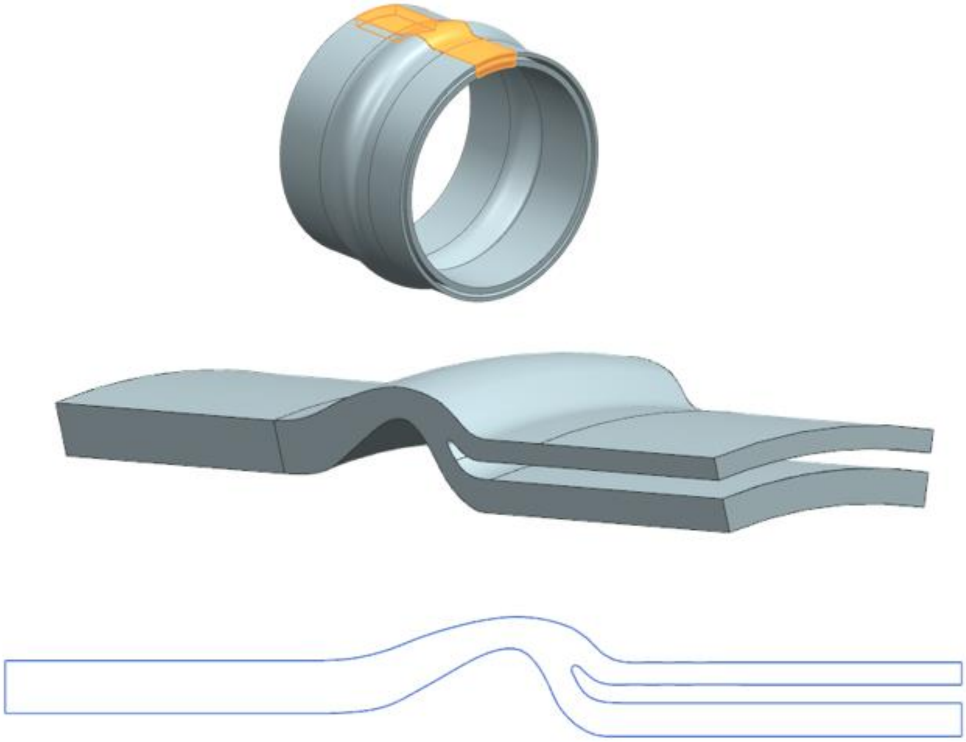

Figure 2.13. Annular IPS geometry, 24° slice and 2-D cross-section.

CFD analysis are performed with 24° slice of the annular IPS geometry, which is given in Figure 2.13, to reduce the mesh size and computational time. Periodic boundary condition is applied at the sidewalls of the IPS. Target mass flow rate values at the core and scavenge outlet boundaries are set as 0.818kg/s and 0.156kg/s respectively for 16% scavenge flow ratio case. The same pressure intervals are used for minimum and maximum values. A reference frame is defined to model the swirling flow and it is applied at the inlet boundary. Swirl angle is chosen as 15° regarding the auxiliary power unit (APU) side intake example in [41].

Baseline mesh configuration is used for meshing the annular IPS geometry and new mesh study is not performed. Both surface and volume meshes are presented in Figure 2.14.

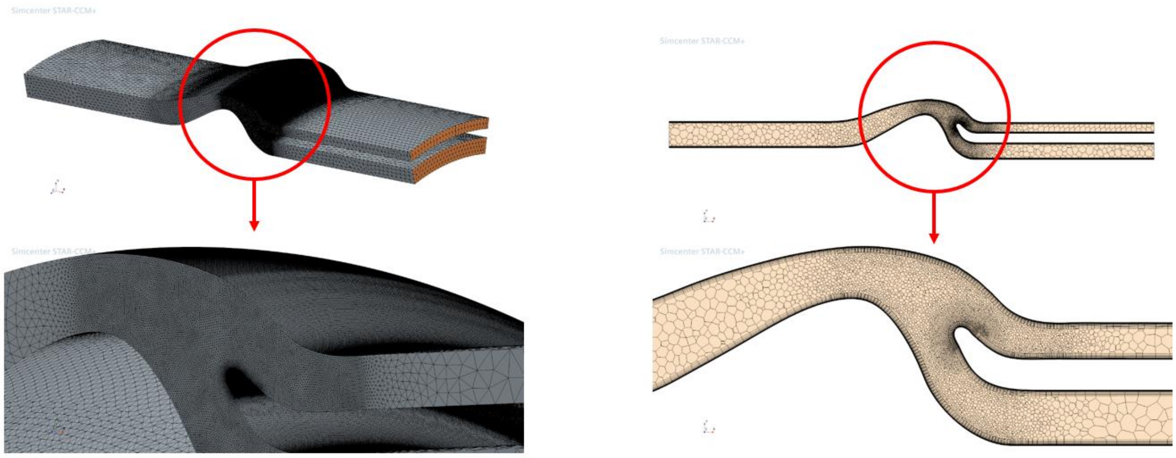

Figure 2.14. Annular IPS surface mesh (left) and volume mesh (right).

In order to make a correct comparison, the new geometry is solved without swirling incoming flow at the beginning. Then, swirling flow is analyzed at the same conditions. The three steps mentioned at the beginning of this chapter are used to obtain flow field and separation efficiency results.

2.3 Results

2.3.1 Validation – Planar IPS Analysis

As mentioned in the Methodology section, a mesh study is performed with three different mesh size (4, 8 and 16 million cell elements) and their results are compared in terms of stability and accuracy. Analyses for all grids are run with 16% scavenge flow ratio condition. Stability of the flows can be estimated from β, which is given in Figure 2.15, and it is measured during the whole analysis.

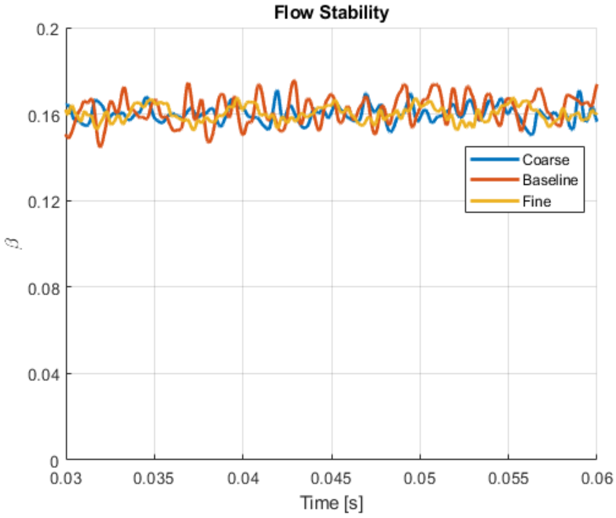

Figure 2.15. Flow stability for each grid.

As it can be seen from Figure 2.15, β oscillates around 0.16 and stability increases with mesh size. When coarse and baseline grids are oscillating about 10%, oscillation reduces to 5% for fine grid. The analyses with all grids are still stable. As mean value of the baseline grid is 0.161, mean of the other grids are 0.1601. Mean total pressures of the scavenge and core outlets differs less than 0.5% for each grid and this condition shows that variations in core and scavenge flows are not significant.

PIV data is also used to compare velocity profiles at core and scavenge channels around splitter. Axial velocity (V_x) is measured for scavenge flow at x=20cm plane and vertical velocity (V_y) is measured for core flow at y=4.8cm plane. Measurement locations for both core and scavenge channels are also illustrated in Figure 2.16.

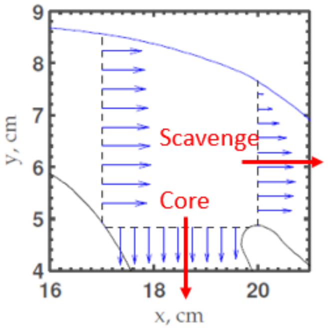

Figure 2.16. Velocity measurement locations. [21]

Velocity profiles are plotted according to the planes given in Figure 2.16 for different times and presented in Figure 2.17.

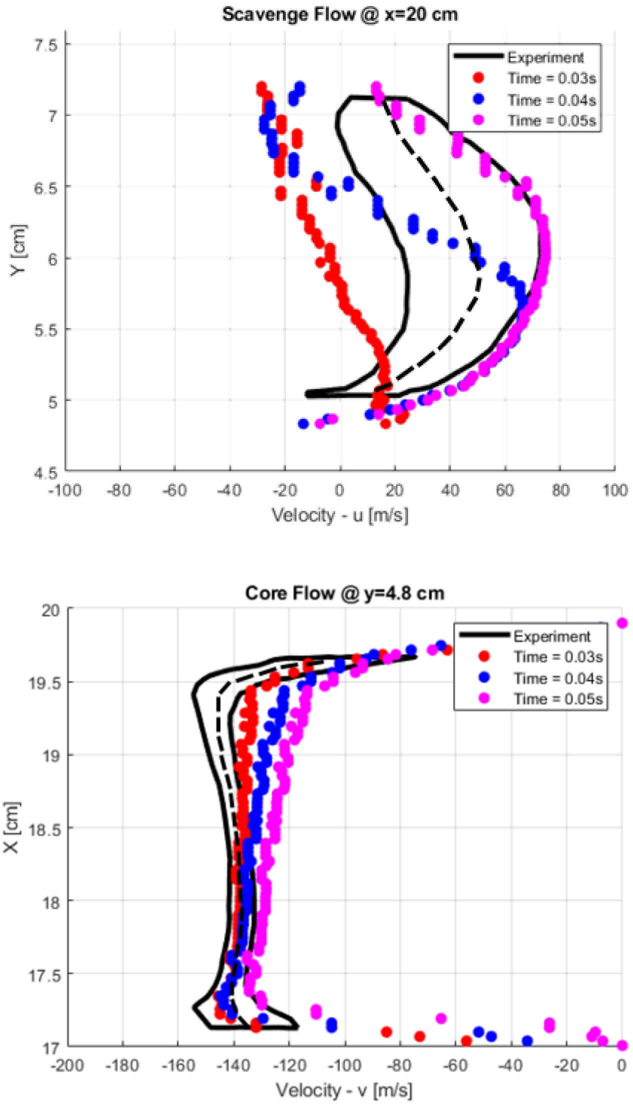

Figure 2.17. Scavenge and core flow velocity profiles at different times.

As it can be seen from Figure 2.17, velocity profiles changes dramatically in time for both scavenge and core flows. Since velocity profile oscillates due to unsteady characteristics of the flow, an envelope is obtained with the time dependent data.

Core and Scavenge velocity profile envelopes and their comparison with the experimental data [21, 26], which has 2% uncertainty for β, with different grids are shown in Figure 2.18.

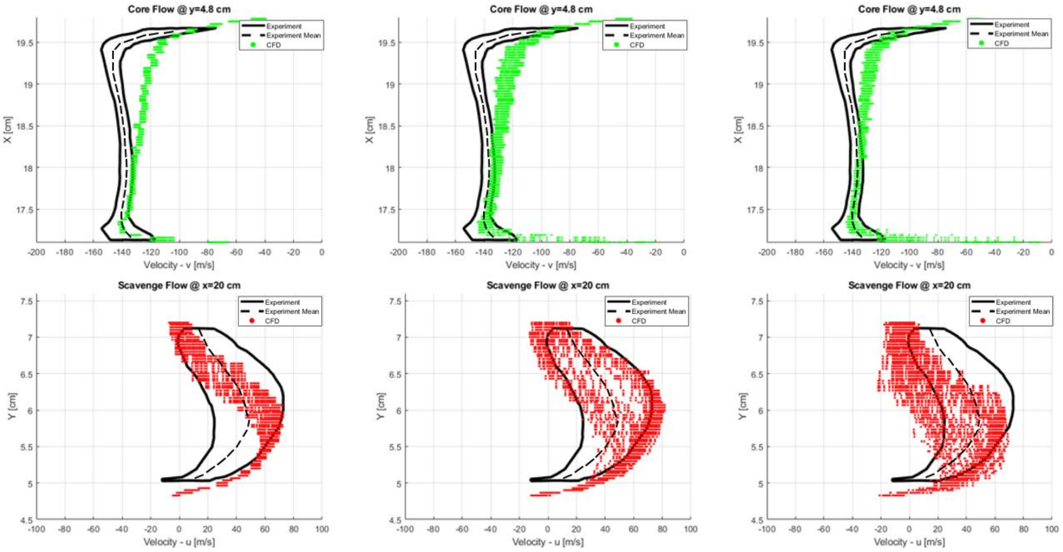

Coarse Baseline Fine

Figure 2.18. Velocity measurement comparison for different grids.

As it can be seen from Figure 2.18, none of the results match with the experimental flow-field around splitter (lower-left side of the scavenge flow envelope and upper-right side of the core flow envelope) due to lack of experimental data which cannot be obtained regarding the laser reflections around the wall. In addition, coarse grid oscillates in a smaller envelope than the experimental envelope. It cannot solve most of the regions in scavenge & core flow envelopes correctly. As baseline grid cover more area in scavenge flow, the fine grid cover more area in core flow. Baseline and fine grid provide similar results and their results' sweep many regions in the experimental envelope. Hence, further studies will be performed with baseline grid.

Moreover, flow-fields of experiment and CFD results with baseline grid are compared in order to make sure the CFD model is appropriate. Velocity contours around splitter region from CFD analysis (left) are compared with the experimental data (right) in Figure 2.19.

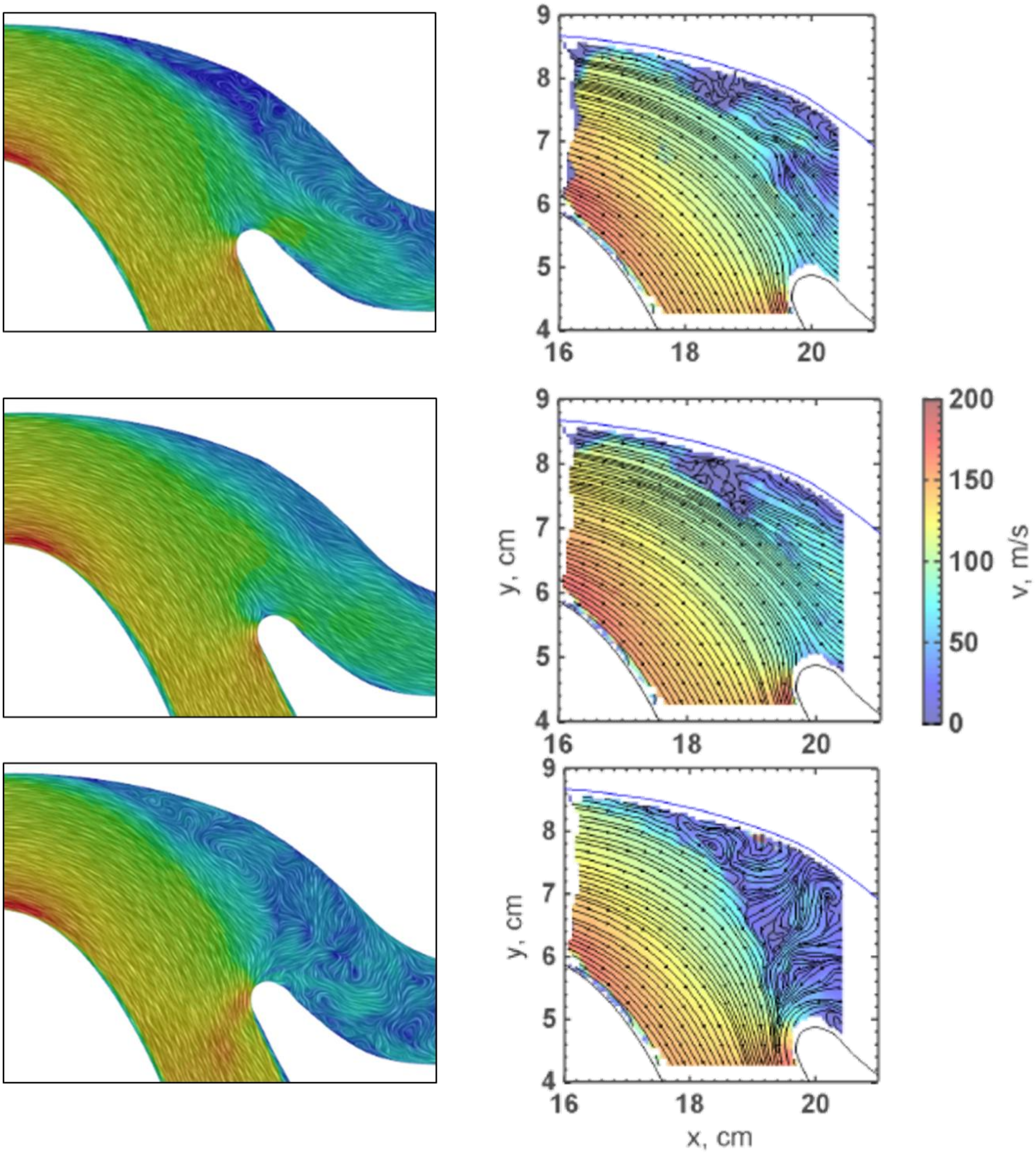

Figure 2.19. Flow-field around splitter at different time steps. CFD result (left) comparison with experimental data (right) [19].

As it can be seen from Figure 2.19, velocity contours around splitter are presented at three different time. At each time, flow behave differently. At the top, scavenge flow is partially blocked due to separation on the OSG. At the middle, separation is disappeared and scavenge channel is open. At the bottom, scavenge flow is completely blocked due to huge vortices in the scavenge channel and flow is directed to core channel. These three flow phase occur periodically in the IPS.

At the same time, oil streak visualizations on OSG and core side of the OSG are compared with the CFD results in Figure 2.20 and Figure 2.21. [12]

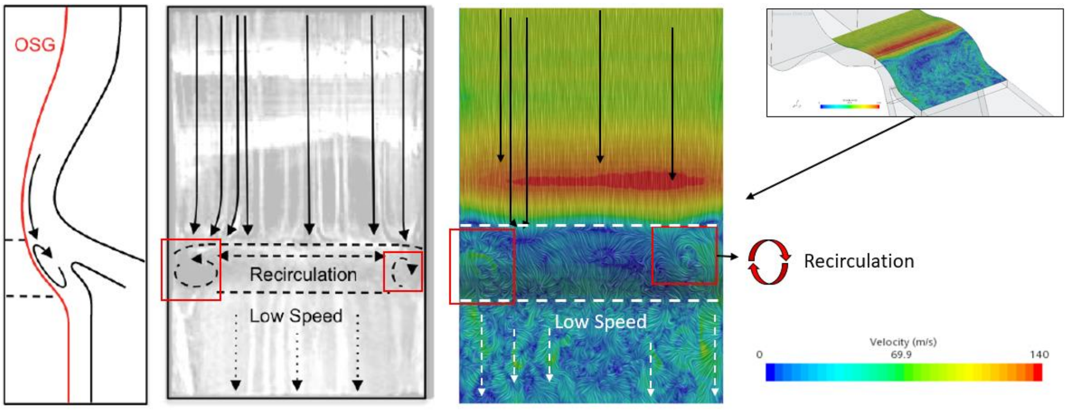

Figure 2.20. Velocity contour on OSG. Experimental oil streak (left) comparison with CFD result (right).

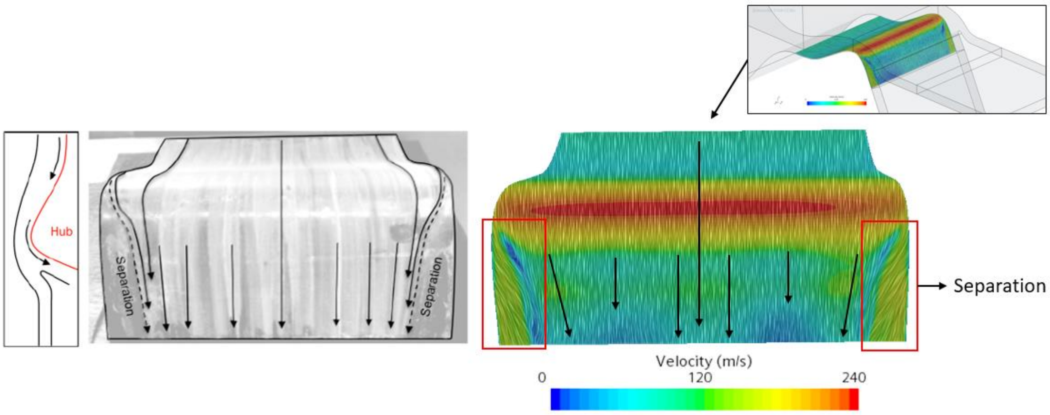

Figure 2.21. Velocity contour on core side of the OSG. Experimental oil streak (left) comparison with CFD result (right).

According to Figure 2.20, very similar velocity fields are obtained at the CFD results with the experimental oil streak visualization. The same recirculation zone, which are marked with red rectangles, can be seen at the sidewalls on OSG. Low speed region at the end of the recirculation zone is also clearly observed. In CFD results, local vortices are observed at low speed region, which is not seen in the experiment.

According to Figure 2.21, again very similar velocity fields are obtained at the CFD results with the experimental oil streak visualization. The same separations, which are marked with red rectangles, can be seen at the sidewalls on the core side of the OSG.

In general, CFD results have a good agreement with the experimental data in terms of flow-field comparison. Particle analysis is also performed with A4 Coarse test dust for 10%, 16% and 20% scavenge flow ratio. Figure 2.22 shows separation efficiency of each particle size.

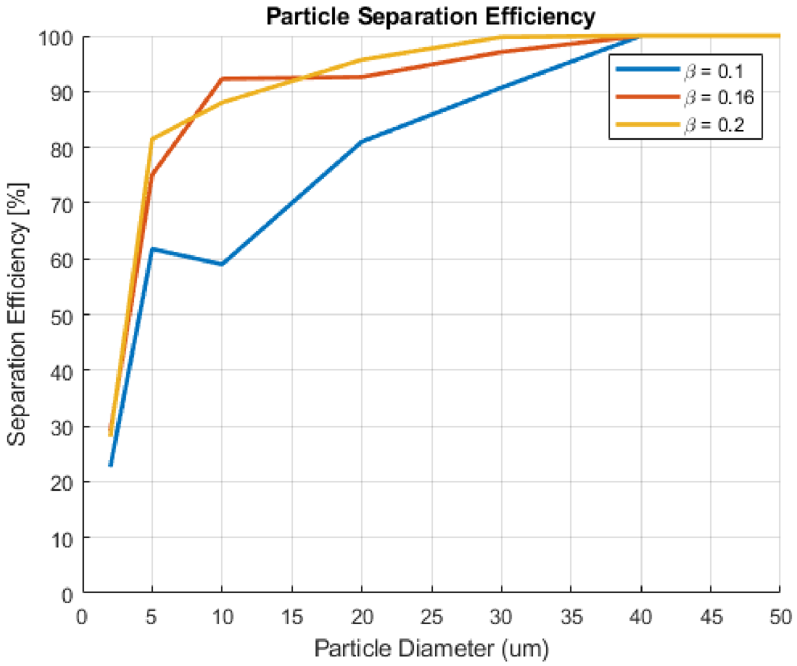

Figure 2.22. Particle separation efficiency for each particle size with different scavenge flow ratio.

As it can be seen from Figure 2.22, particle diameter and scavenge flow ratio proportional to separation efficiency except for 10µm particles. Separation efficiency of particles with 10µm diameter behave in a strange manner for β=0.1 and β=0.16. As Stokes number <1, which is valid for a 10µm particle, drag dominated forces influence the particle more than the bounce forces. This phenomenon makes the prediction of particle motion complicated at low β due to the increased turbulence effects. Moreover, particles with size bigger than 50µm are separated 100% and they are not included in the Figure 2.22. Connolly [22] mentioned that particles with high inertia (ex: 100µm) impact the splitter and lost their momentum. These particles are ingested by the engine and separation efficiency of these particles are less than 100%. This situation is not observed in this study and the difference may be observed due to the position of the particles where they released.

Separation efficiency results for each individual particle are multiplied with the weighting factor and overall separation efficiency for A4 test dust is obtained. Results are compared with the experimental data for three scavenge flow ratio and presented in Figure 2.23.

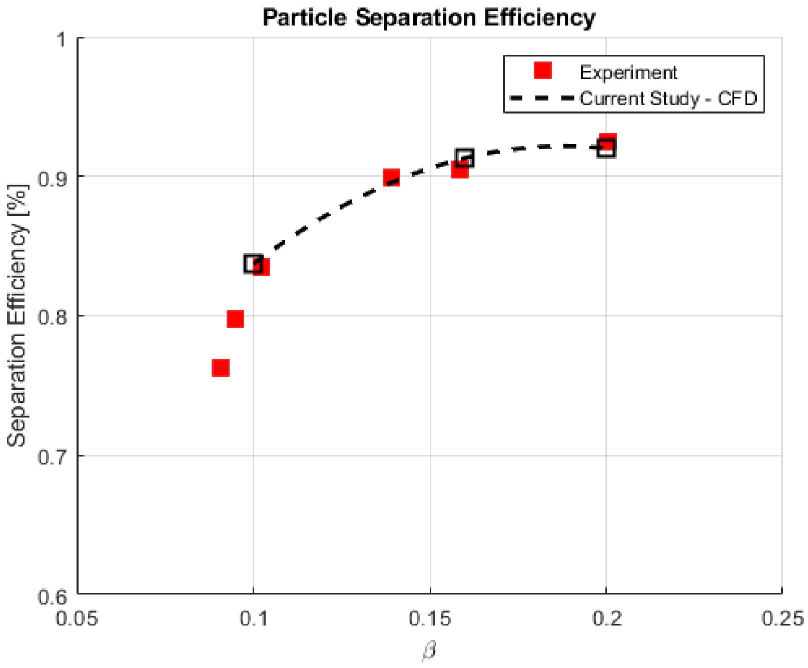

Figure 2.23. Particle separation efficiency for A4 Coarse test dust with different scavenge flow ratio.

According to the Figure 2.23, it is clear to see that particle separation results match with the experimental results perfectly. Error is found less than 1% for each condition where the experiment uncertainty was 1-2%. The method used for particle motion prediction is validated and further studies can be performed with this method.

2.3.2 Annular IPS Analysis

Annular IPS is analyzed with both straight and swirling flow condition to observe the intake effects on separation efficiency more clearly. Before separation efficiency results, flow-field is investigated. Flow-field of the new IPS geometry for straight and swirling flow condition is plotted at the center plane when the massive flow separation is occurred on the OSG and it is shown in Figure 2.24.

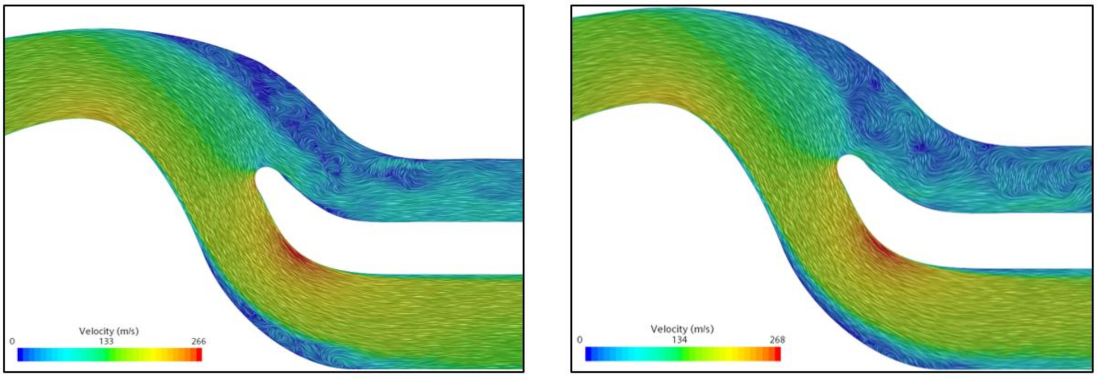

Figure 2.24. Flow-field for straight (left) and swirling (right) flow.

According to the Figure 2.24, a new separation region is occurred at the bottom wall of the core channel due to the increase in the core channel height in a short distance. This separation may be reduced by modifying the surface curvature. Comparison between straight and swirling flows is hard with a two dimensional plane visualization; hence, flow-fields are visualized in 3-D with streamlines. Streamlines (plotted when the massive flow separation is occurred) of both core and scavenge flows are presented separately in Figure 2.25 for straight flow condition.

As it can be seen from Figure 2.25, recirculation regions around OSG, marked with red rectangle and red circle, can be seen easily in the scavenge flow streamlines. In addition, a re-ingestion event is observed in the core flow. Some part of the scavenge flow, marked with white circles, rotated back to the core flow which will also cause re-ingestion of the particles into the engine. Moreover, an empty region (low-pressure region), marked with black circle, is occurred due to this event and a huge circulation in the scavenge flow, marked with red circle, is appeared regarding the high-pressure to low-pressure movement tendency of the flow.

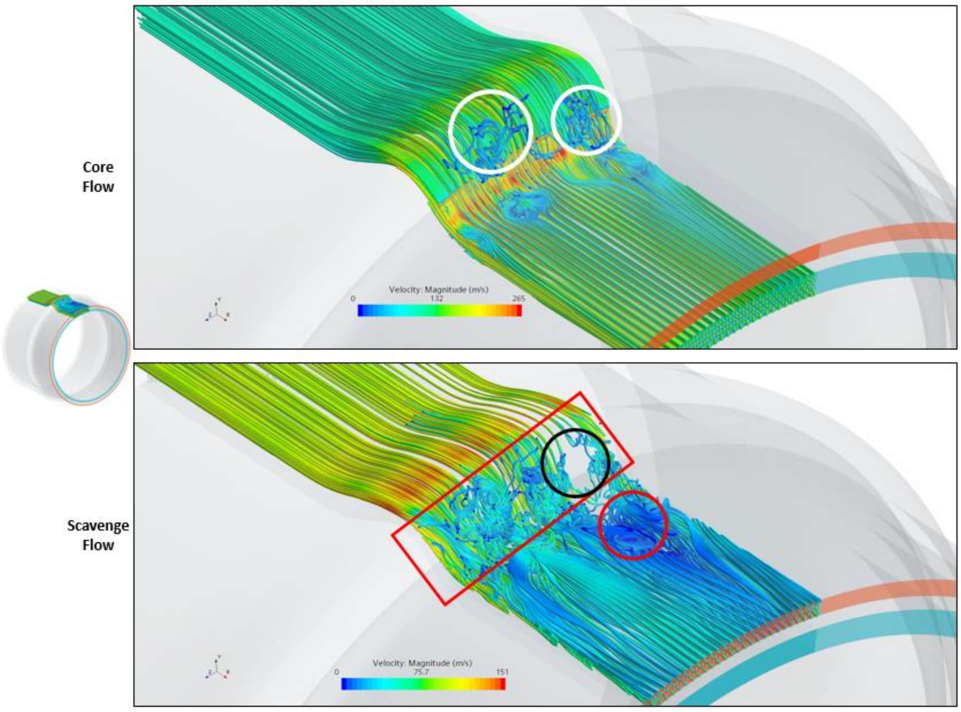

Figure 2.25. Streamlines for straight flow.

Streamlines of both core and scavenge flows are presented separately in Figure 2.26 for swirling flow condition. Swirling flow boundary is implemented successfully which can be seen from incoming flow angle. Swirl angle is reduced in the core flow after the bifurcation part and it is increased in the scavenge flow. This phenomenon is occurred due to the boundary condition implementation. Flow direction of the core and scavenge flow outlet boundaries are implemented with the boundary normal option. Because of this implementation, swirl angle in the core flow is reduced due to its higher inertia however, swirl angle in the scavenge flow is increased to conserve the angular momentum. Moreover, re-ingestion event is disappeared in the swirling flow condition. This is probably due to the less inertia in the longitudinal direction of the core flow where some amount of its longitudinal inertia transferred to the lateral direction to swirl the flow. When the longitudinal inertia of the flow decreases, axial velocity of the flow decreases and pressure of the flow increases. This situation yields with less pressure difference between flow at the bifurcation and the core flow boundary. At the end flow moves to the scavenge and cannot re-ingested by the core flow.

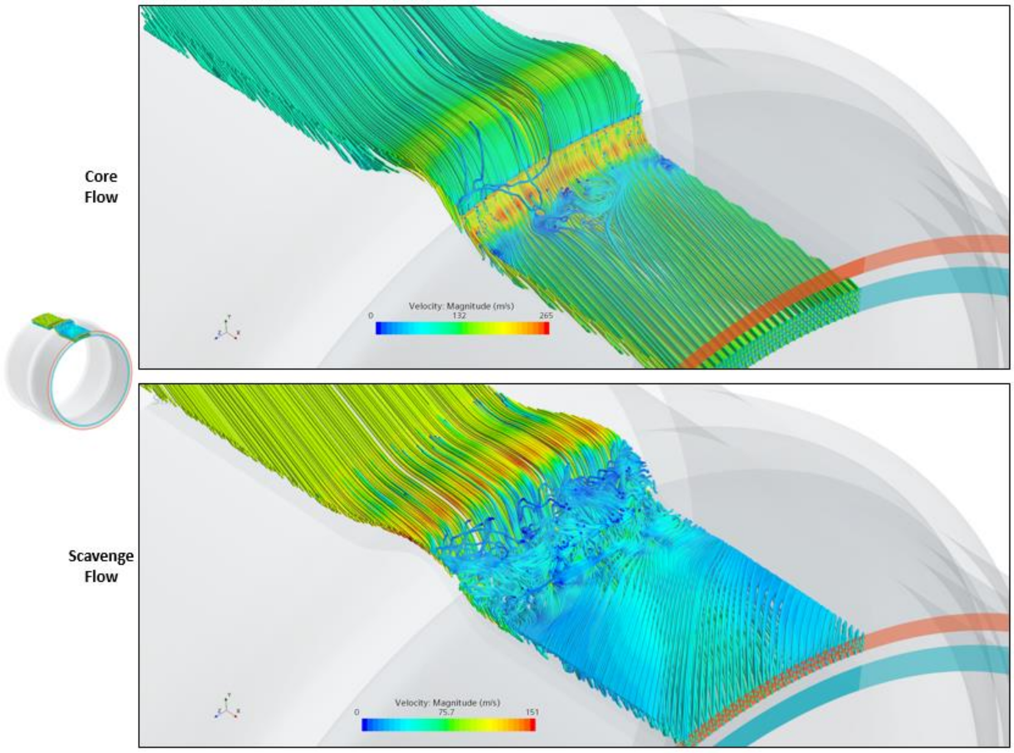

Figure 2.26. Streamlines for swirling flow.

After the flow-field investigations, particle trajectories are analyzed. Particle trajectories and particle velocity are presented in Figure 2.27 for 2μm, 10μm and 20μm particles.

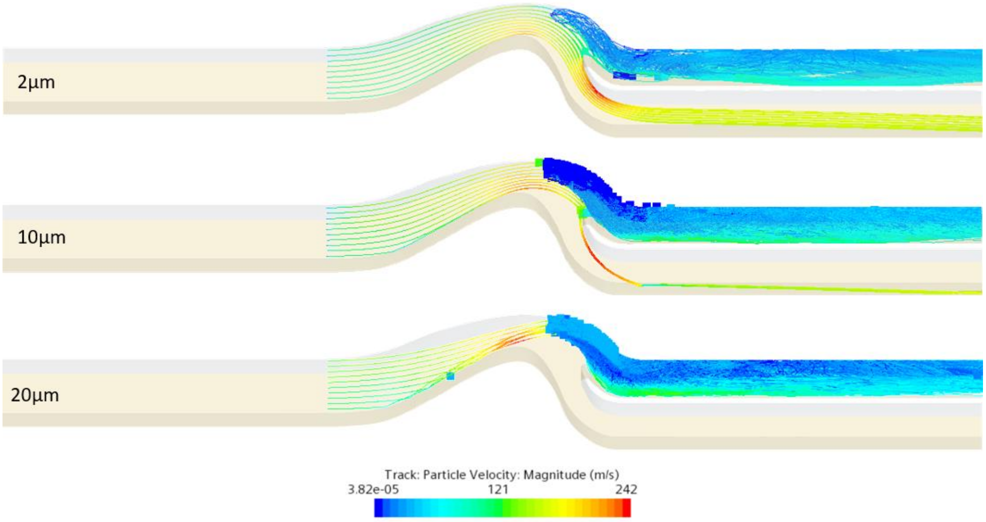

Figure 2.27. Particle trajectories and particle velocity for swirling flow.

As it can be seen from Figure 2.27, particle separation efficiency increases as particle size increases which is an expected phenomenon. The bigger particles have higher inertia and they tend to follow the ballistic trajectory. However, the smaller particles have less inertia and they tend to follow the streamline trajectory. One of the other reason for the particle ingestion is recirculation region on the OSG. When the scavenge side is clogged due to the huge recirculation and flow separation, particles with St<1 get into the recirculation region and re-ingested by the core flow. Before they re-ingested by the core flow, they also interact with the splitter. An example of the re-ingested 10µm particles and their interaction with the splitter wall are presented in Figure 2.28.

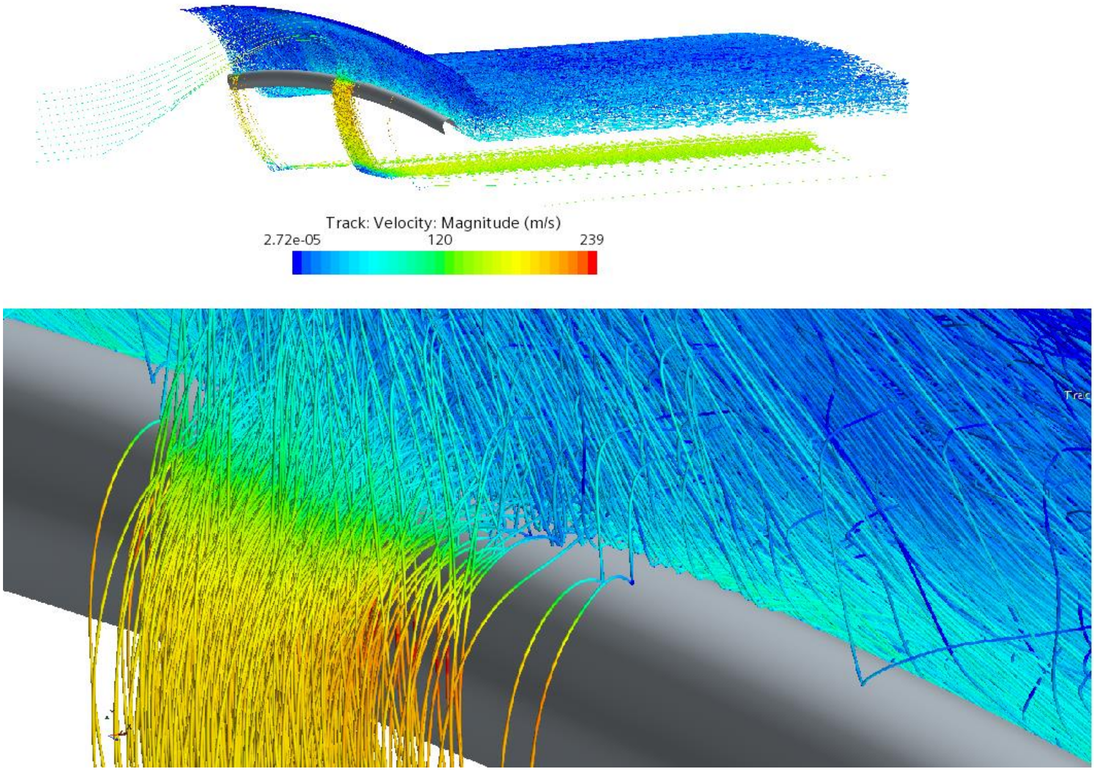

Figure 2.28. 10μm particle trajectories and splitter interaction.

As presented in Figure 2.28, many particles interact with the splitter due to the blocked scavenge channel and move to the core channel. A similar re-ingestion case is also shown in Connolly’s study [22]. However, some particles can be captured by circulation region in the scavenge channel and they stuck in the separated zone. Their speed may reach near zero until the separation disappear.

Moreover, particle separation efficiency of each particle size is presented in Figure 2.29 for both straight and swirling flow.

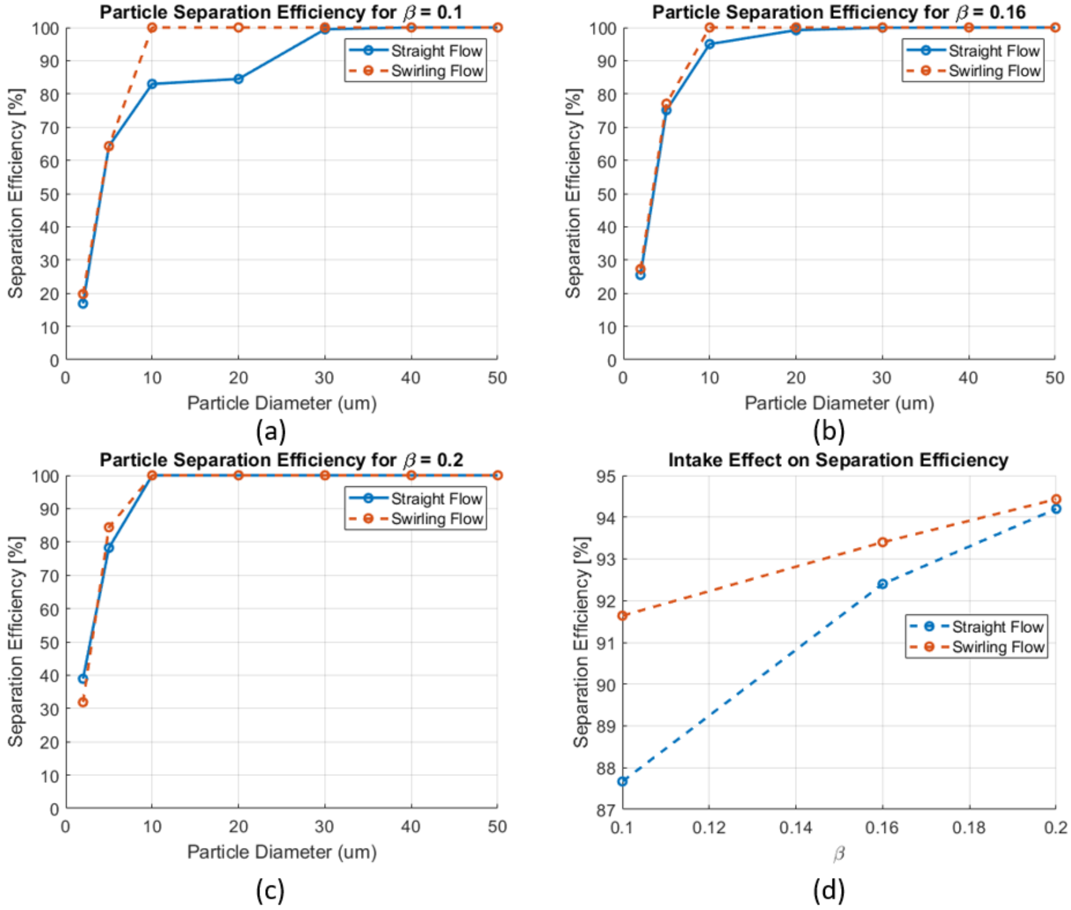

Figure 2.29. Separation efficiency comparison of each particle for both straight and swirling flow for β=0.1 (a), for β=0.16 (b), for β=0.2 (c). Cumulative separation efficiency (d).

According to Figure 2.29.a-c, it is easy to say that swirl affects the separation efficiency in a positive way. Separation efficiency of the all particles is higher when the flow swirls except 2μm particles with β=0.2 condition. Adding a swirl effect to the flow increases the centrifugal force acting on the particle. However, linear momentum of the flow and particle reduces at the same time. When increased centrifugal force leads the particle to be scavenged, reduced particle momentum leads the particle to be affected by bounce forces more than drag forces and results with ingestion by the core flow. There is a balance at this point.

According to Figure 2.29.d, as β increases, the difference between the separation efficiencies of straight and swirling flow decreases. When β=0.1, the highest difference between the separation efficiencies is observed which is approximately 4%. When β=0.2, the difference between the separation efficiencies reduces to approximately 0.2%. In addition, separation efficiency of the particles larger than 30μm have not affected by the flow where separation efficiency of the particles with high inertia is dominated by the bouncing forces.

2.4 Conclusion

In this study, one of the intake effects, swirl effect, on the IPS separation performance is investigated with CFD. 3-D unsteady analyses are performed with a high fidelity turbulence model due to incapability of the RANS methods to capture the entire physical phenomenon. Particle motion is estimated with the Lagrangian approach. At the beginning, the computational models for flow-field and particle motion are validated with the experiment, which performed with a planar IPS geometry. A new IPS geometry is created to implement the swirling flow, which requires annular geometry. When creating the new IPS geometry, a special study is paid attention to preserve the flow-field characteristics. The new geometry is analyzed with the straight flow and then the swirling flow. Results show that swirling flow increase the separation efficiency approximately 4% when β=0.1 and 0.2% when β=0.2. According to [5], 4% efficiency increase (approximately from 88% to 92%) will result with 7 times engine life increase. Maintenance and inspection intervals of the several engine sections depend on the IPS efficiency. Keeping the time between inspections/maintenance operations shorter brings loss of time, supplies and money. However, keeping it longer may result with loss of equipment or even loss of aircraft.

CHAPTER 3

RANS TURBULENCE MODEL INVESTIGATION WITH 2-D IPS GEOMETRY

3.1 Introduction

In the previous chapter, highly accurate CFD analyses are performed for a 3-D IPS, which requires enormous computational power and time. However, this accuracy level is not required if the study is only in a preliminary stage or this kind of computational power may not be available. For these kind of situations, 2-D modelling and RANS based turbulence models are very helpful and they are commonly used in literature and industry.

Many computational IPS studies in the literature including 2-D geometries and RANS based turbulence models, which are the most commonly used models for IPS analysis, are investigated in the previous chapter with details. Although eddy viscosity models (Spalart-Allmaras, k-ε, k-ω, υ^2-f etc.) are commonly used [28, 30-33, 35, 37], Reynolds Stress Transport (RST) models are also used in the literature [27] for IPS analysis.

Each turbulence model has advantages and disadvantages when compared to others. Although RST models are more accurate than the eddy viscosity models, they are computationally more expensive and numerically stiffer. They are not commonly used due to these drawbacks.

On the other side, many studies are performed to increase the accuracy of the eddy viscosity models. Beside wall treatments like two-layer approach, high/low-Reynolds number approach, new turbulence models like Realizable k-ε, AKN k-ε, k-ω SST etc. are created for this purpose. Moreover, compressibility correction, curvature correction, non-linear constitutive relations and lag models are other improvements that are studied in RANS based turbulence world.

In spite of those improvements, results are not satisfactory enough. In the turbulence models, there are several closure coefficients which are predicted by using previous experiments and some assumptions. Hence, a new approach known as fine-tuning or sensitivity analysis is recently started to use in the literature. In this approach, closure coefficients are calibrated to increase the accuracy. However, calibrated closure coefficients are case dependent, which means that each set of coefficients can be used especially for the studied case.

Previous Studies:

Narjisse et al. [43] studied atmospheric boundary layer in hilly terrain problem. C_μ, $C_{\varepsilon 1}$, $C_{\varepsilon 2}$, σ_k, σ_ε and κ coefficients in k-ε turbulence model and β^*, α_1, α_2, β_1, β_2, $\sigma_{\omega 1}$, $\sigma_{\omega 2}$, σ_{k1}, σ_{k2} and a_1 coefficients in SST k- ω turbulence model are recalibrated to a new value. The coefficients given in this and the following paragraphs will be introduced later. It was observed that recalibrated SST k-ω turbulence model provided more accurate results than other models in recirculation regions.

Bounds et al. [44] performed a fine-tuning study to improve the flow over the Ahmad body and real car body. β^*, $\sigma_{\omega 1}$, $\sigma_{\omega 2}$, σ_{k1} and σ_{k2} coefficients are investigated within a range for SST k-ω turbulence model. Effect of each coefficient is investigated one by one. Results are compared with the experimental data in terms of downforce/drag coefficients. It is noted that as the most effective coefficient is β^*, σ_{k1} and σ_{k2} coefficients have almost no effect on the results.

Fu et al. [45] investigated β^*, $\sigma_{\omega 1}$, $\sigma_{\omega 2}$, σ_{k1} and σ_{k2} closure coefficients of SST k-ω turbulence model within a range for NASCAR racecar model. Again, effect of each coefficient is investigated one by one. The similar outcomes about the coefficients are obtained with the [44]. Better results are obtained with the modified coefficients.

Ronch et al. [46] studied transonic airfoil case by using machine learning, which uses adaptive design of experiment (DOE) algorithm. σ, k, c_{v1}, c_{w3}, c_{t3}, c_{t4}, c_{b1}, c_{b2} and c_{w2} closure coefficients of the Spalart-Allmaras turbulence model are studied within a range.

Taghizadeh et al. [47] perform a study on turbulent channel flow by using machine learning to obtain an optimized closure coefficient set. β, β^*, σ, σ^* and α closure coefficients of standard k-ω turbulence model are examined. Instead of a range, three specific cases with different closure coefficients are used. It is stated that, significant improvements are observed.

Shirzadi et al. [48] analyzed the atmospheric boundary layer for high buildings by using Monte Carlo sampling and stochastic optimization method. C_μ, $C_{\varepsilon 1}$, $C_{\varepsilon 2}$ and σ_k coefficients of k-ε turbulence model studied within a range. Results are improved in a significant manner.

Erb et al. [49] worked on canonical flow cases, which are well known cases investigated by NASA. Wilcox k-ω (2006), SST k-ω and Spalart-Allmaras turbulence models are studied to enhance the accuracy of the results. The most sensitive closure coefficients are determined for each turbulence model.

Stefano [50] performed a sensitivity analysis for scramjet combustor flow by using nonintrusive polynomial chaos theory. Wilcox k-ω (2006), SST k-ω, baseline k-ω (Menter) and Spalart-Allmaras turbulence models are studied. Again, the most sensitive closure coefficients are determined for each turbulence model.

Dangeti [51] investigated β^*, $\sigma_{\omega 1}$ and $\sigma_{\omega 2}$ closure coefficients of SST k-ω turbulence model within a range for a simplified car model. Effect of each coefficient is investigated one by one. The similar outcomes about the coefficients are obtained with the [44] and [45].

Previous studies show that, closure coefficients in the RANS turbulence models are not constants and these coefficients are case dependent. If there is enough experimental data, uncertainty of the closure coefficients can be studied to obtain more accurate results. At the beginning of this study, several turbulence models were investigated to find out, which is more appropriate for 2-D IPS flow. According to the results, a sensitivity analysis was performed for the best-fitted turbulence model by using optimization methods.

3.2 Methodology

The 2-D IPS geometry, which has the same dimensions with the geometry that is used in Chapter 2, is generated by using Siemens NX software. Then, the geometry is imported into Star-CCM+ software and fluid domain is discretized with unstructured polyhedral elements. In this study, SST k-ω (SST), Spalart-Allmaras (SA), Realizable k-ε Two Layer (RKE) and Lag Elliptic Blending k-ε (LEB KE) turbulence models are examined. According to the results, the best-resulted model is investigated with a fine-tuning approach. For this purpose, mesh is generated by obeying the y+ < 1 law where, all turbulence models mentioned above works well with it (each turbulence model uses all y+ approach). Mesh study, which is performed with SST turbulence model, shows that the solutions are independent from the grid size. Grids are consist of 22,000 (coarse), 44,000 (baseline) and 91,000 (fine) elements. These grids used in the mesh study are shown in Figure 3.1.

As boundary types given in Chapter 2 remain the same, outlet boundary conditions are modified to preserve the similar flow fields according to the 2-D geometry. At the inlet, stagnation inlet boundary is set to zero Pascal gauge pressure. Scavenge outlet and core outlet boundaries are set to pressure outlet with target mass flow option. The target mass flow rates are calculated with the original mass flow rates dividing by the width of the geometry and scavenge and core mass flow rates are 0.727 $\frac{kg}{s}\frac{1}{m}$and 3.817$\frac{kg}{s}\frac{1}{m}$, respectively [25]. Temperature is set to 15°C at the inlet and outlet boundaries. All other settings are leaved as default.

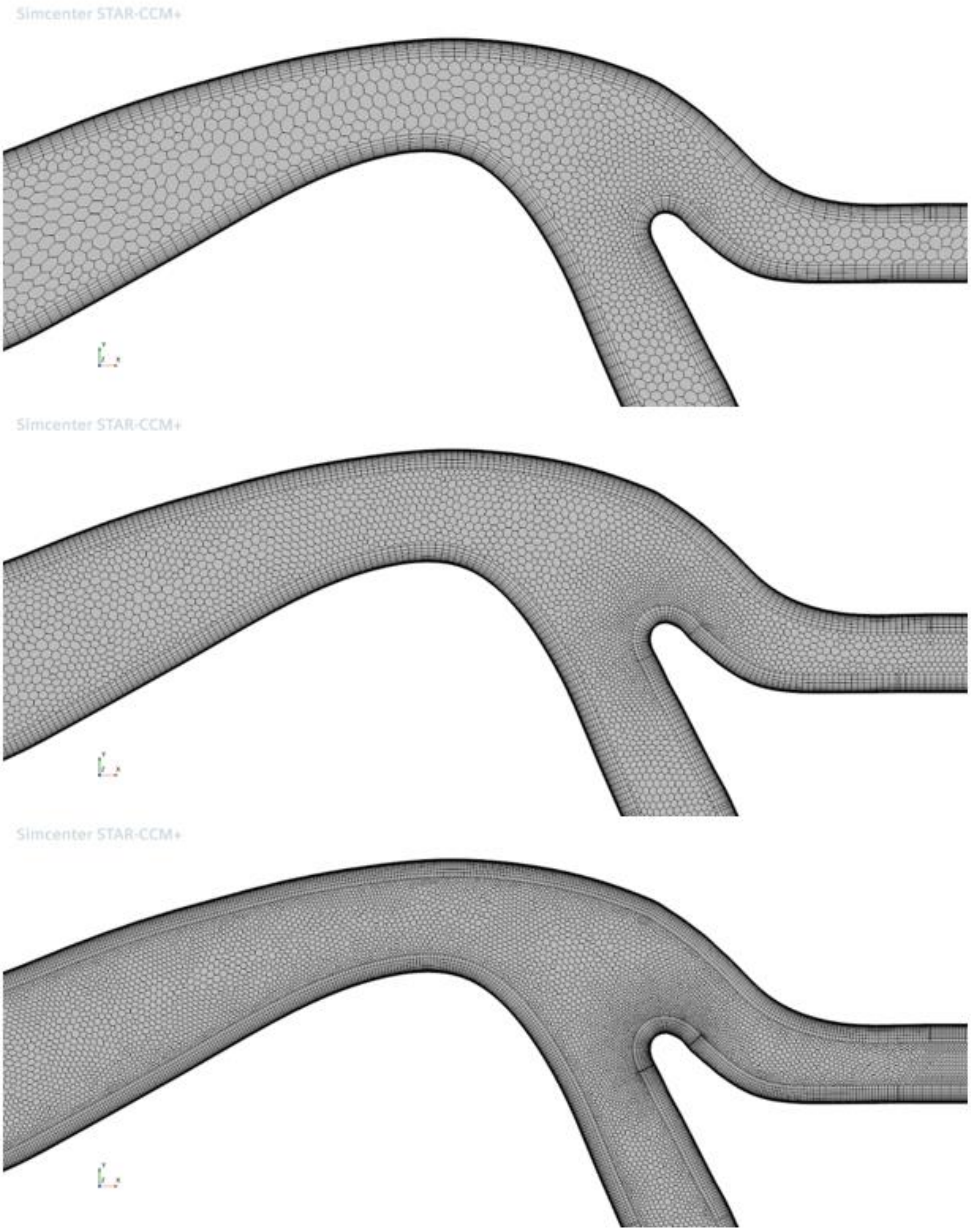

Figure 3.1. 2-D IPS grids

This study is accomplished in two parts, which are:

- Turbulence model investigation
- Fine-tuning study.

At first, analyses are performed with steady approach and they converged in 2000 iterations. Convergence is monitored by checking residuals, pressure and mass flow rate values at the core and scavenge outlet boundaries. Coupled implicit flow solver is used to conserve the continuity and momentum. Fluxes are evaluated by using second order upwind discretization scheme. Air is used as material with ideal gas model.

Turbulence model investigation:

In this study, four turbulence models are investigated to obtain the most accurate results for 2-D IPS problem.

Spalart-Allmaras Turbulence Model [52, 38]:

The first model is the one-equation model, which is the standard Spalart-Allmaras (SA) turbulence model. It solves modified diffusivity ($\tilde{\nu}$) in the transport equation to obtain eddy viscosity. The relation between the modified diffusivity and the eddy viscosity is given in Eq. 29.

$$\mu_t = \rho f_{v1} \tilde{\nu} \tag{30}$$

where, f_{v1} is a damping function and it is given in Eq. 30.

$$f_{v1} = \frac{\left(\frac{\tilde{\nu}}{\nu}\right)^3}{\left(\frac{\tilde{\nu}}{\nu}\right)^3 C_{v1}^3} \tag{31}$$

where, C_{v1} is a model coefficient.

The transport equation for the SA model is given in Eq. 31.

$$\frac{\partial}{\partial t}(\rho\tilde{\nu}) + \nabla \cdot \left(\rho\tilde{\nu}\overline{\boldsymbol{V}}\right) = \frac{1}{\sigma_{\tilde{\nu}}} \nabla \cdot [(\mu + \rho\tilde{\nu})\nabla\tilde{\nu}] + P_{\tilde{\nu}} \tag{32}$$

where, $\sigma_{\tilde{\nu}}$ is a model coefficient and $P_{\tilde{\nu}}$ is the production term. $P_{\tilde{\nu}}$ is given in Eq. 32.

$$P_{\tilde{\nu}} = \begin{array}{c} Turbulent \\ Production \end{array} + \begin{array}{c} Non-linear \\ Production \end{array} + \begin{array}{c} \text{Non} - \text{conservative} \\ \text{Diffusion} \end{array} - \begin{array}{c} Turbulent \\ Dissipation \end{array} \tag{33}$$

SA turbulence model designed for attached boundary layer problems such as flow over airfoil/wing. If it is used with separated flow, turbulence model starts to struggle. It is also not suitable for jet flow in free-shear zones.

Realizable k-ε Turbulence Model with Two-Layer Approach [53, 54, 38]:

The second model is a two-equation model, which is Realizable k-ε (RKE) turbulence model with two-layer approach. It solves turbulent kinetic energy (k) and the turbulent dissipation rate (ε) in the transport equation to obtain eddy viscosity. Transport variables and eddy viscosity relation is given in Eq. 33.

$$\mu_t = \rho C_\mu f_\mu \frac{k^2}{\varepsilon} \tag{34}$$

where, C_μ is a model coefficient and f_μ is the damping function.

In RKE turbulence model, transport equation of turbulent dissipation rate is modified and f_μ is used to damp the C_μ. In this process, normal stresses are calculated with a more realistic manner (realizability).

Moreover, two-layer approach allows the turbulence model to be applied in boundary layer calculations where it is accomplished in two parts. In the first part, eddy viscosity and turbulent dissipation rate are defined as a function of wall distance at the first cell located next to the wall. In the cells located away from the wall, the turbulent dissipation rate is calculated and its values are found by using the blending functions for the cells that are located between these two zones. At the second part, the turbulent kinetic energy is calculated for the whole flow domain. Consequently, different equations are solved at the near wall for one or two variables.

The transport equations for the RKE turbulence model with two-layer approach are given in Eq. 34-35.

$$\frac{\partial}{\partial t}(\rho k) + \nabla \cdot \left(\rho k \overline{\boldsymbol{V}}\right) = \nabla \cdot \left[\left(\mu + \frac{\mu_t}{\sigma_k}\right)\nabla k\right] + P_k - \rho(\varepsilon - \varepsilon_0) \tag{35}$$

$$\frac{\partial}{\partial t}(\rho \varepsilon) + \nabla \cdot \left(\rho \varepsilon \overline{\boldsymbol{V}}\right) = \nabla \cdot \left[\left(\mu + \frac{\mu_t}{\sigma_\varepsilon}\right)\nabla \varepsilon\right] + \frac{\varepsilon}{k} C_{\varepsilon 1} P_\varepsilon - C_{\varepsilon 2} f_2 \rho (\frac{\varepsilon^2}{k} - \frac{\varepsilon_0}{T_0}) \tag{36}$$

where, σ_k, σ_ε, $C_{\varepsilon 1}$ and $C_{\varepsilon 2}$ are model coefficients. f_2 is the damping function and it is given in Eq. 36. ε_0 is the ambient turbulence value and T_0 is specific time-scale which is given in Eq. 37.

$$\frac{k}{k+\sqrt{\nu\varepsilon}} \tag{37}$$

$$T_0 = \max\left(\frac{k_0}{\varepsilon_0}, C_t\sqrt{\frac{\nu}{\varepsilon_0}}\right) \tag{38}$$

P_k and P_ε are the production terms which are given in Eq. 38-39

$$P_k = \frac{Turbulent}{Production} + \frac{Bouyancy}{Production} - \frac{Compressibility}{Modification} \tag{39}$$

$$P_\varepsilon = \frac{Turbulent}{Production} + C_{\varepsilon 3} * \frac{Bouyancy}{Production} \tag{40}$$

where, $C_{\varepsilon 3}$ is a model coefficient.

Realizable k-ε turbulence model ensures the positivity of normal stresses and Schwarz’s inequality unlike standard k-ε turbulence model. As standard k-ε turbulence model struggle for rotational flows and flows in boundary layer under strong adverse pressure gradient or separation, RKE turbulence model improves the performance for planar round jets, strong streamline curvature in addition to rotational flows and flows in boundary layer under strong adverse pressure gradient or separation.

SST k-ω Turbulence Model: [55, 38]:

The third model is another two-equation model, which is SST k-ω turbulence model. The standard k-ω turbulence model has a drawback known as freestream sensitivity. In freestream (external flow) or inlet (internal flow), boundary layer calculations are sensitive to specific dissipation rate. Menter introduced a new blending approach to overcome this problem. In the new approach, he uses k-ω model in the boundary layer and k-ε model in the free-shear regions. Menter also introduced another modification known as linear constitutive relation, which assumes relation between the mean strain rate and stress tensor is linear. This new model is called Shear-Stress

Transport k-ω (SST) turbulence model. Today, non-linear constitutive relations, which satisfies Reynold stress anisotropy, are available in most of the commercial solvers.

SST turbulence model solves the turbulent kinetic energy (k) and specific dissipation rate (ω) in transport equations. Transport variables and eddy viscosity relation is given in Eq. 40.

$$\mu_t = \rho k \min\left(\frac{\alpha^*}{\omega}, \frac{a_1}{SF_2}\right) \tag{41}$$

where, α^* *and* a_1 are model coefficients. **S** is the mean rate tensor and F_2 is the blending function which is given in Eq. 41.

$$F_2 = \tanh\left(\left(max\left(\frac{2\sqrt{k}}{\beta^*\omega d}, \frac{500\nu}{d^2\omega}\right)\right)^2\right) \tag{42}$$

where, β^* is a model coefficient and d is the wall distance.

Transport equations of turbulent kinetic energy and specific dissipation rate are presented in Eq. 42-43.

$$\frac{\partial}{\partial t}(\rho k) + \nabla \cdot \left(\rho k \overline{\boldsymbol{V}}\right) = \nabla \cdot [(\mu + \sigma_k \mu_t)\nabla \mathrm{k}] + P_k - \rho\beta^*\omega \mathrm{k} \tag{43}$$

$$\frac{\partial}{\partial t}(\rho \omega) + \nabla \cdot \left(\rho \omega \overline{\boldsymbol{V}}\right) = \nabla \cdot [(\mu + \sigma_\omega \mu_t)\nabla \omega] + P_\omega - \rho\beta\omega^2 \tag{44}$$

where, σ_k and σ_ω are model coefficients. P_{k} and P_ω are production terms which are given in Eq. 44-45.

$$P_k = \begin{matrix} Turbulent \\ Production \end{matrix} + \begin{matrix} Non-linear \\ Production \end{matrix} + \begin{matrix} Bouyancy \\ Production \end{matrix} \tag{45}$$

$$P_\omega = \begin{matrix} Specific\ Dissipation \\ Production \end{matrix} + \begin{matrix} Cross-difusion \\ Term \end{matrix} \tag{46}$$

The cross-diffusion term includes another blending function, F_1 and its formula is given in Eq. 46.

$$\begin{matrix} Cross-difusion \\ Term \end{matrix} = 2\rho(1-F_1)\sigma_{\omega 2}\frac{1}{\omega}\nabla \mathrm{k} \cdot \nabla \omega \tag{47}$$

where, $\sigma_{\omega 2}$ is a model coefficient and F_1 is given in Eq. 47.

$$F_1 = \tanh\left(\left[min\left(max\left(\frac{\sqrt{k}}{\beta^{*}\omega d},\frac{500\nu}{d^2\omega}\right),\frac{2k}{d^2 CD_{k\omega}}\right)\right]^4\right) \tag{48}$$

where, $CD_{k\omega}$ is cross-diffusion constant.

SST turbulence model is one of the most commonly used model in aerospace applications. It provides better estimations than k-ε turbulence model for separations and reattachments. However, it fails in complex internal flow problems.

<u>Lag Elliptic Blending k-ε Turbulence Model</u> [56, 38]:

The last model is a four-equation model, which is Lag Elliptic Blending k-ε (LEB KE) turbulence model. It solves turbulent kinetic energy (k), turbulent dissipation rate (ε), normalized wall-normal stress component ($\varphi = \frac{\overline{\vartheta^2}}{k}$) and elliptic blending factor (α) in the transport equations to obtain eddy viscosity. The relation for the eddy viscosity is given in Eq. 48.

$$\mu_t = \rho C_\mu \varphi k \min\left(\sqrt{\frac{k^2}{\varepsilon^2}+C_t^2\frac{\nu}{\varepsilon}},\frac{C_T}{\sqrt{3}C_\mu \varphi S}\right) \tag{49}$$

where, C_t, C_μ and C_T are model coefficients.

The transport equations for LEB KE turbulence model are given in Eq. 49-52.

$$\frac{\partial}{\partial t}(\rho k) + \nabla\cdot\left(\rho k\overline{\boldsymbol{V}}\right) = \nabla\cdot\left[\left(\frac{\mu}{2}+\frac{\mu_t}{\sigma_k}\right)\nabla k\right] + P_k - \rho(\varepsilon-\varepsilon_0) \tag{50}$$

$$\frac{\partial}{\partial t}(\rho\varepsilon) + \nabla\cdot\left(\rho\varepsilon\overline{\boldsymbol{V}}\right) = \nabla\cdot\left[\left(\frac{\mu}{2}+\frac{\mu_t}{\sigma_\varepsilon}\right)\nabla\varepsilon\right] + \frac{\varepsilon}{k}C_{\varepsilon 1}P_\varepsilon - C_{\varepsilon 2}^{*}\rho\left(\frac{\varepsilon^2}{k}-\frac{\varepsilon_0}{T_0}\right) \tag{51}$$

$$\frac{\partial}{\partial t}(\rho\varphi) + \nabla\cdot\left(\rho\varphi\overline{\boldsymbol{V}}\right) = \nabla\cdot\left[\left(\frac{\mu}{2}+\frac{\mu_t}{\sigma_\varphi}\right)\nabla\varphi\right] + P_\varphi \tag{52}$$

$$\nabla\cdot\left(L^2\nabla\alpha\right) = \alpha - 1 \tag{53}$$

where, σ_k, σ_ε, σ_φ, $C_{\varepsilon 1}$, $C_{\varepsilon 2}^*$ are model coefficients and L is the turbulent length scale which is given in Eq. 53.

$$L = C_L \sqrt{\frac{k^3}{\varepsilon^2} + C_\eta^2 \sqrt{\frac{\nu^3}{\varepsilon}}} \tag{54}$$

Where, C_L and C_η are model coefficients.

P_k, P_ε and P_φ are the production terms and they are given in Eq. 54-56.

$$P_k = \frac{Turbulent}{Production} + \frac{Bouyancy}{Production} + \frac{Compressibility}{Modification} \tag{55}$$

$$P_\varepsilon = \frac{Turbulent}{Production} + C_{\varepsilon 3} * \frac{Bouyancy}{Production} + \frac{Additional}{Production} \tag{56}$$

$$P_\varphi = -(2 - C_{\varepsilon 1})\frac{\varphi}{k}\left(\frac{Turbulent}{Production} + \frac{Bouyancy}{Production}\right) + \rho(1-\alpha^3)f_w + \rho\alpha^3 f_h \tag{57}$$

where, f_w and f_h are functions of $\varphi, \varepsilon, k, \rho, \nu,$ mean strain rate tensor and some model constants ($C_{\varepsilon 2}, C_\mu, C_1, C_1^*, C_{p3}, C_3^*, C_4, C_5$).

The elliptic blending approach solves two additional equations to obtain more accurate results in the near wall region without using wall functions. The standard elliptic blending model came up with a more accurate result in boundary layer calculations according to the RKE turbulence model. Moreover, its stability was improved on SST turbulence model. In the Lag Elliptic Blending concept, the standard elliptic blending approach is combined with the stress-strain lag model. The lag model obtains better results when the stress-strain misalignment is dominant in the flow regime. It prevents the over prediction of production of the turbulent kinetic energy unlike linear models. The LEB KE turbulence model enhanced the results of flow with separation, rotation and unsteady characteristics.

The performance comparison of turbulence models, which is evaluated by using root mean squared error, is presented in the “Results” section in details. Because, the error cannot be calculated with a realistic manner by using average error method due to low velocity regions in the recirculation zone. In this zone, velocity is found around 0.1 m/s for some points; however, the velocity is 0-10 m/s in the experiment which means that high amount of error is observed in the results. By using this approach, correct comparison cannot be made, hence root mean squared error method is used. Root mean squared error (RMSE) formula is given in Eq. 57.

$$RMSE = \sqrt{\frac{1}{n}\sum_{i=1}^{n}\left(V_{experiment,i} - V_{CFD,i}\right)^2} \tag{58}$$

where, n is the total number of data points, $V_{CFD,i}$ and $V_{experiment,i}$ are the velocity data at the ith point.

The LEB KE turbulence model resulted with most accurate results. Hence, the second part focused on LEB KE turbulence model.

Fine Tuning Study:

At the second part, a fine-tuning study is performed for the LEB KE turbulence model to improve the results for the specific IPS case. For this purpose, closure coefficients are investigated. There are many coefficients used in this turbulence model; however, some of them, taken from the Elliptic Blending Reynolds-Stress model [57], do not require any further calibration. The other closure coefficients are suitable for the calibration and four of them, $C_{\varepsilon 1}, C_{\varepsilon 2}, \sigma_k$ and σ_ε, are examined in this study. Their original values are modified with a great care to prevent the creation of unphysical condition. For this purpose, a communication is performed with the Mr. Sylvain Lardeau (author of the turbulence model) via e-mail. He provided direct modification ranges for σ_k and σ_ε closure coefficients and he guided to found a proper range for the other coefficients. The $C_{\varepsilon 1}$ and $C_{\varepsilon 2}$ coefficients are generally considered together. As $C_{\varepsilon 2}$ is calibrated with decaying homogeneous-isotropic turbulence, $C_{\varepsilon 1}$ is calibrated with homogeneous shear flows. [58]

According to decaying homogeneous-isotropic turbulence, $C_{\varepsilon 2}$ can be found as in Eq. 58.

$$C_{\varepsilon 2} = \frac{n+1}{n} \tag{59}$$

where, n is the decay exponent and its value takes place between 1.1 and 1.5 according to the experimental grid turbulence measurements in wind tunnel. Hence, $C_{\varepsilon 2}$ gets value between 1.667 and 1.909.

According to homogeneous shear flows $C_{\varepsilon 1}$ can be found as in Eq. 59.

$$\frac{\mathcal{P}}{\varepsilon} = \frac{C_{\varepsilon 2} - C_{\varepsilon 1}}{C_{\varepsilon 1} - 1} + 1 \tag{60}$$

where, $\frac{\mathcal{P}}{\varepsilon}$ is ratio of production to dissipation and its value is between 1.4 and 1.8 according to the experimental data. Hence, $C_{\varepsilon 1}$ gets value between 1.37 and 1.65.

Closure coefficients, their ranges and resolutions used in this study are presented in Table 3.1. The three of the closure coefficients are investigated with high resolution; however, σ_k is investigated with a low resolution. According to lots of the studies mentioned in the Introduction section, σ_k variation has almost no effect on the solution.

Table 3.1. Closure coefficient ranges

	$C_{\varepsilon 1}$	$C_{\varepsilon 2}$	σ_k	σ_ε
Lower Value	1.37	1.667	0.8	0.75
Baseline	**1.44**	**1.9**	**1**	**1.2**
Upper Value	1.65	1.909	1.2	1.5
Resolution	15	13	5	16

After the decision process of the closure coefficient ranges, preliminary analyses are performed to see how closure coefficient change affects the results. However, σ_k did not included to these analysis set due to its expected ineffectiveness on the result. These preliminary analysis set is shown in Table 3.2 and baseline values are indicated as bold.

Table 3.2. Preliminary analysis set

$C_{\varepsilon 1}$	$C_{\varepsilon 2}$	σ_{ε}
1.37	1.67	0.75
1.44	1.78	**1.2**
1.65	**1.9**	1.5

At the end of the preliminary analysis, the whole closure coefficient matrix is investigated. The closure coefficients given in Table 3.1 are used as design variables in Siemens HEEDS MDO software to perform an optimization study. As a search algorithm, SHERPA is used to find an optimum solution within the shortest time. SHERPA has adaptive & hybrid optimization algorithms, which utilizes many search procedures and learns the problem & its design space. [59]

SHERPA has two option for optimization according to the objective function. The first option is “Weighted sum of all objectives” which checks the summation of all the objectives are reduced or not. The second option is “Multiple objective tradeoff study” and it is used with conflicting objectives. In the optimization study, there is only one objective function; hence, weighted sum of all objectives option is used.

The objective function is obtained by using the root mean squared error. The optimization process is adjusted to minimize this objective function. A simple representation of the determination of the objective function is given in Figure 3.2 and the objective function is described in Eq. 60.

$$Objective = \sqrt{\frac{1}{n}\sum_{i=1}^{n}(\Delta p - i)^2} = \sqrt{\frac{1}{n}\sum_{i=1}^{n}\left(V_{experiment,i} - V_{CFD,i}\right)^2} \qquad (61)$$

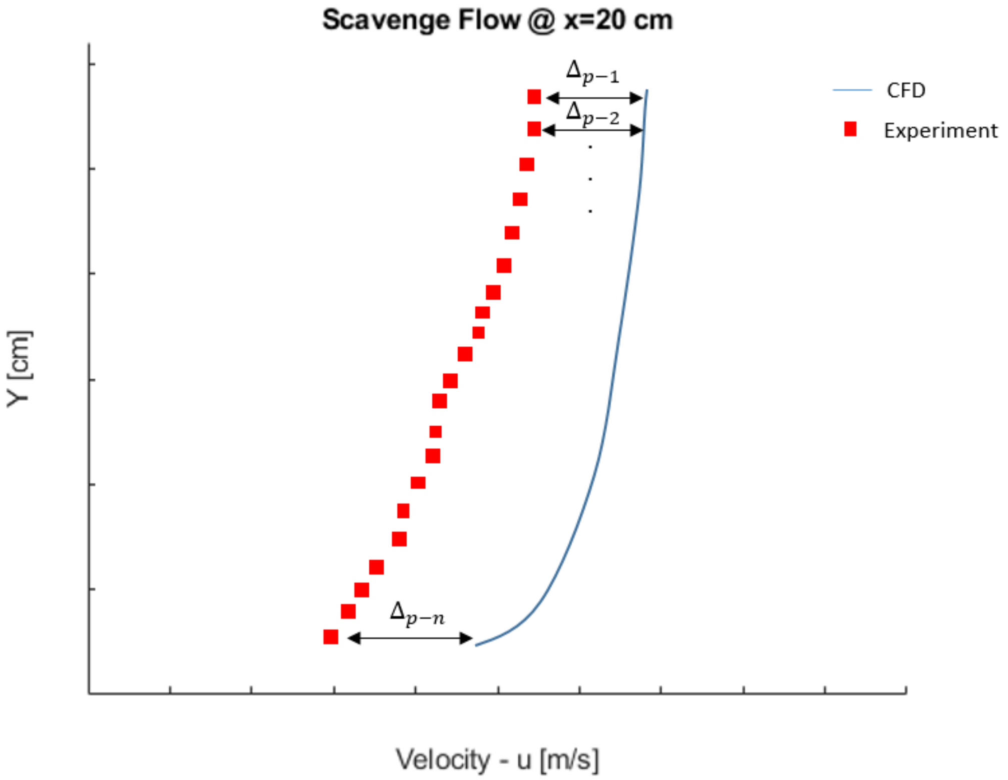

Figure 3.2. A fictive representation of objective function determination way

Weighted sum of all objectives approach uses both local and global search methods simultaneously. SHERPA processes the result of each method and it learns the design space. As it gains experience from the design spaces, SHERPA modifies its internal parameters and it creates the most effective optimization algorithm for the specific problem. SHERPA requires only one input, which is the number of analysis, from the user. In this study, 15600 analyses are required to cover all of the closure coefficients' resolution; however, only 100 analyses are given as an input. Moreover, a constraint is used to hold β close to the 16%; since, it is impossible to holdβ at 16%. For this purpose, the range of β is set from 15% to 17%.

3.3 Results

At the beginning, mesh study is performed and results are presented in Figure 3.3. Velocity profile at the scavenge leg at x=20 cm is used for the result comparison. The place where the velocity data is analyzed is presented in Figure 2.16.

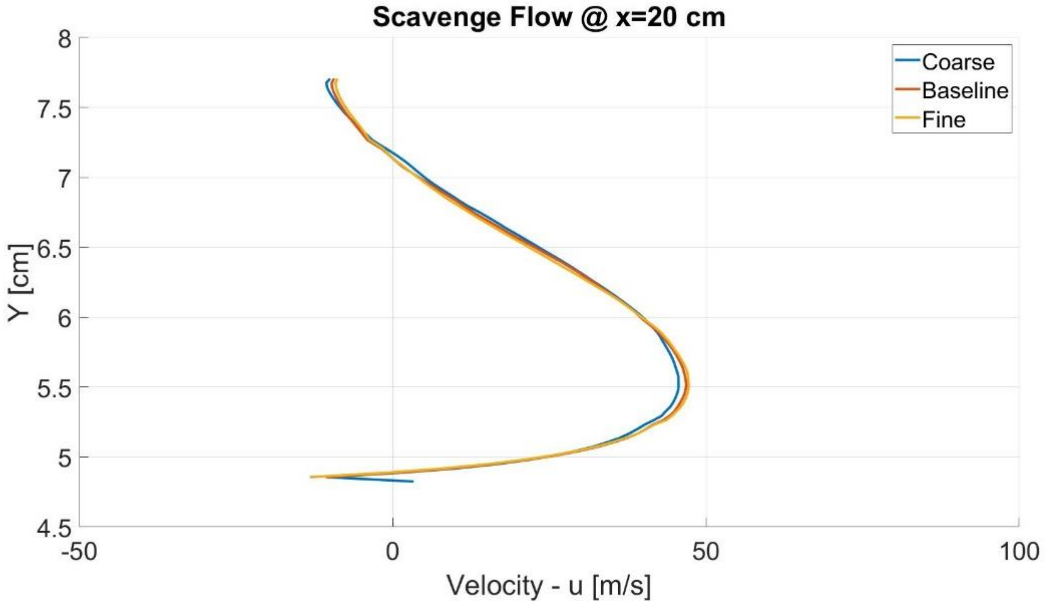

Figure 3.3. 2-D IPS Mesh Study

As it can be seen from Figure 3.3, as mesh size increases, velocity profile at the scavenge leg changes. Although the results are similar for all grids, results of the coarse mesh slightly deviates from the rest. Therefore, the baseline mesh is used for the further studies.

<u>Turbulence model investigation:</u>

Velocity profiles at the scavenge channel are compared with the mean of the experimental data for the comparison of the turbulence model results. As the experimental data consist of an envelope, showed in Figure 2.18, it is not possible to compare the steady analysis results and the experimental data. Hence, mean of the experimental data is used for comparison.

As mentioned in the Methodology section, SA, SST k-ω SST, RKE and LEB KE turbulence models are examined in this study. As a start, velocity profiles are compared with the mean of the experimental data in Figure 3.4.

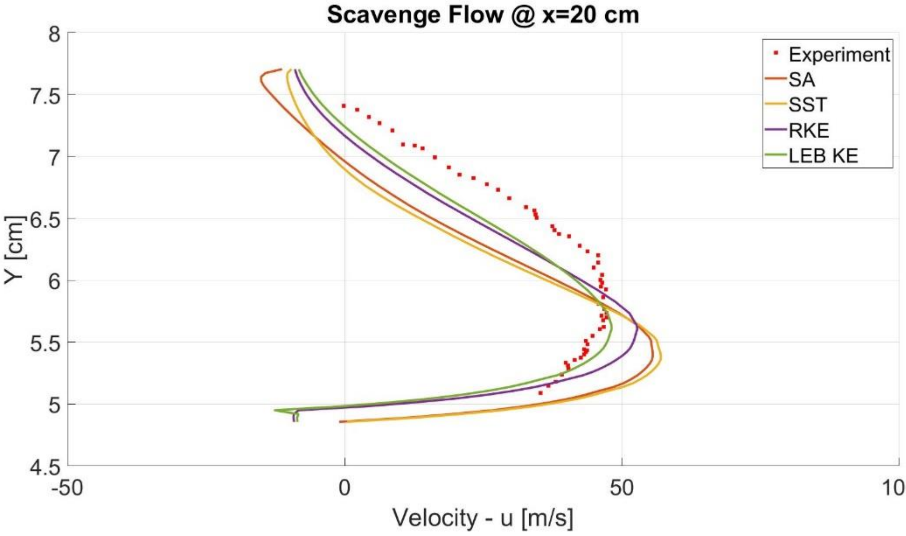

Figure 3.4. Velocity profiles at the scavenge leg for different turbulence models and mean of the experimental data.

Figure 3.4 shows that all of the turbulence models overestimate the velocity at the pick point and they under estimate the velocity at the other regions. As SST and SA estimates the velocity profile with a larger error, k-ε turbulence models provide better results. LEB KE turbulence model ends up with the most accurate result. Discrepancy of the results might be explained with the anisotropy of the turbulence. As IPS flow has strong curvature and high adverse pressure gradient, LEB KE turbulence model, which uses an approach similar to anisotropic turbulence, provided the most accurate result.

The flow-field is investigated in terms of several parameters and the first of them is velocity. When velocity contours of each turbulence model illustrated side by side, it is not easy to understand the difference between them. For this reason, the velocity difference contours are presented in Figure 3.5 for each of the turbulence models according to the LEB KE turbulence model. Moreover, the color bar is changed from blue-red to high-contrast for ease of recognition of the differences.

As it can be seen from Figure 3.5, similar flow-field is obtained with the one given in Chapter 2. There is almost no velocity difference around the whole domain except the recirculation region and the scavenge channel for all of the turbulence models. The largest positive difference is observed at the region where separation starts and reattachment occurs for all of the turbulence models. The largest negative difference is observed in the recirculation region on the OSG wall for SA turbulence model, which estimates the velocity in the recirculation zone less than 100% according to the LEB KE. The velocity distribution in the circulation region is very low. For this reason, the difference becomes very large in this region. The largest negative difference in SST turbulence model is obtained at the shear zone that is located between recirculation and scavenge flow. Again, the velocity difference is more than 100% but in a smaller region. In the RKE turbulence model, it can be said that the largest negative difference is observed after the reattachment zone in the scavenge channel. The smallest difference is obtained with this model.

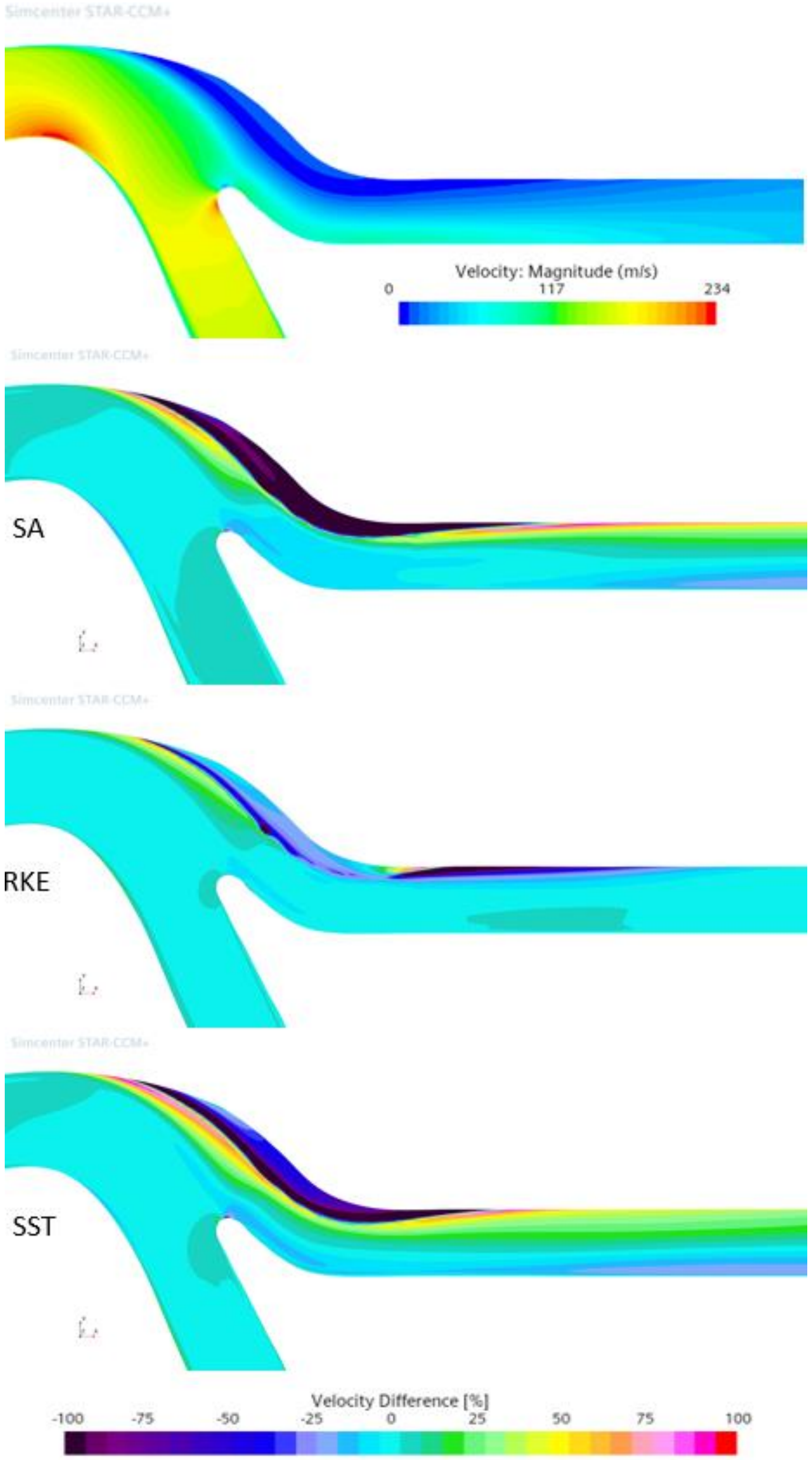

Figure 3.5. Velocity contour of LEB KE turbulence model and velocity difference contours according to LEB KE turbulence model

Streamlines around the bifurcation region are depicted in Figure 3.6 for all turbulence models.

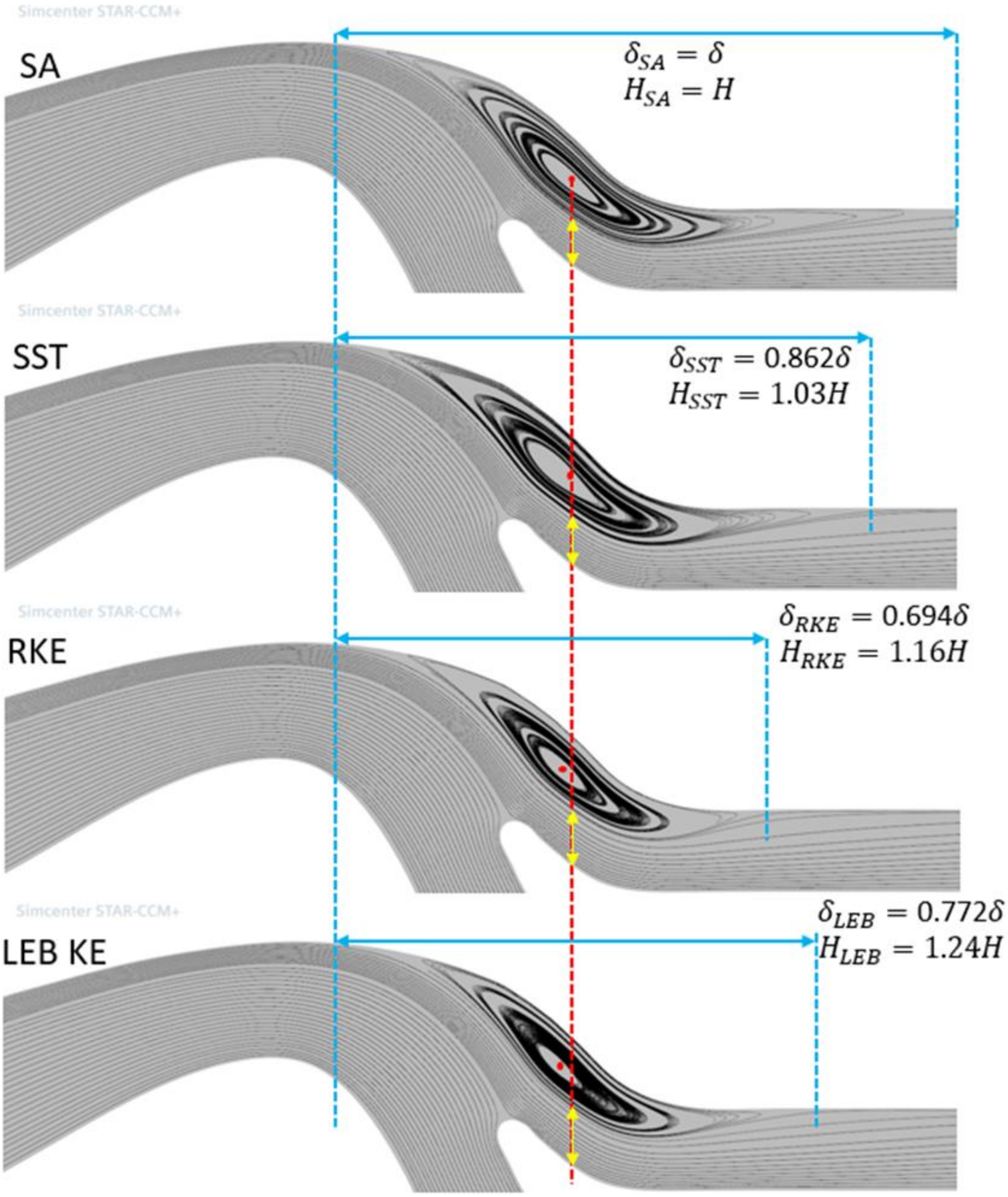

Figure 3.6. Streamlines around the bifurcation region for different turbulence models

It is clear to see that separation starts at the same location for all of the turbulence models in Figure 3.6. As SA and SST overestimate reattachment length, RKE underestimates it. When the SA model is taken as reference, the reattachment length of the SST, RKE and LEB KE turbulence models are shorter 14%, 31% and 23%, respectively. The center of the recirculation is almost the same for SA and SST turbulence models. However, center of the recirculation is slightly moved backward in axial direction for RKE and LEB KE turbulence models. The last parameter investigated for the recirculation region is the scavenge flow height which is indicated with the yellow arrow in the Figure 3.6. Scavenge flow height of the SA turbulence model is taken as reference. The scavenge flow height increases 3%, 16% and 24% for SST, RKE and LEB KE turbulence models, respectively.

Another investigated parameter in the flow-field is turbulent viscosity ratio. Contours are shown in Figure 3.7 for all turbulence models.

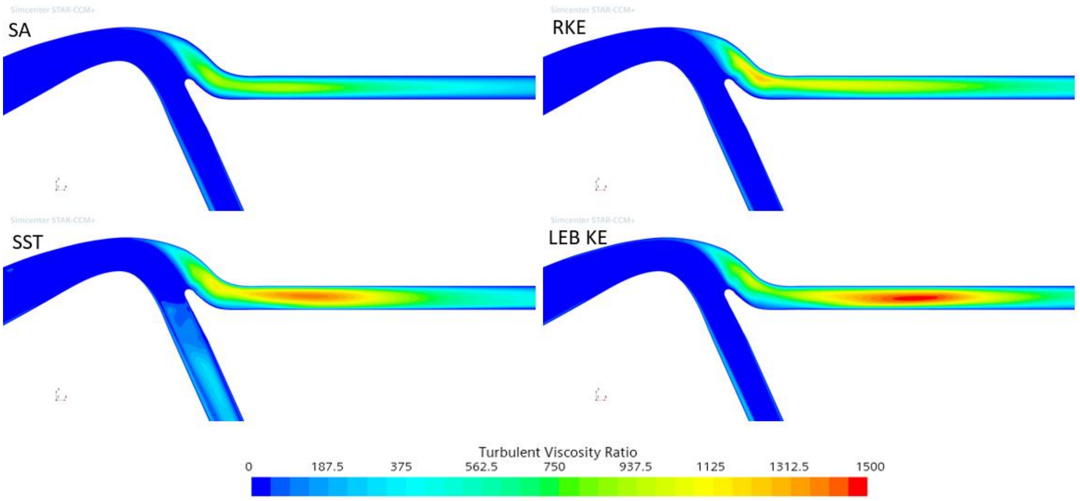

Figure 3.7. Turbulent viscosity ratio contours for different turbulence models

According to the Figure 3.7, turbulent viscosity ratio in the core channel and the region behind the bifurcation is around zero, which means that flow does not have turbulent characteristics at these regions. In the core channel, a small thin zone occurred with higher turbulent viscosity ratio due to separation after the hump for all of the turbulence models except SST. In the result of SST, turbulent viscosity ratio is higher in the whole core channel. At the scavenge channel, turbulent viscosity ratio gradually increases from SA to LEB KE turbulence model. In terms of velocity profile and velocity distribution in the flow-field, SA and SST results are similar. At the same time, RKE and LEB KE provide analogous results. However, SST results are closer than RKE to LEB KE results in terms of turbulent viscosity ratio. Each turbulence model calculates eddy viscosity with a different approach and this is the main reason of the turbulent viscosity ratio difference.

The last parameter investigated in the flow-field is turbulent kinetic energy. Contours are illustrated in Figure 3.8 for all turbulence models except SA turbulence model, which does not calculate it.

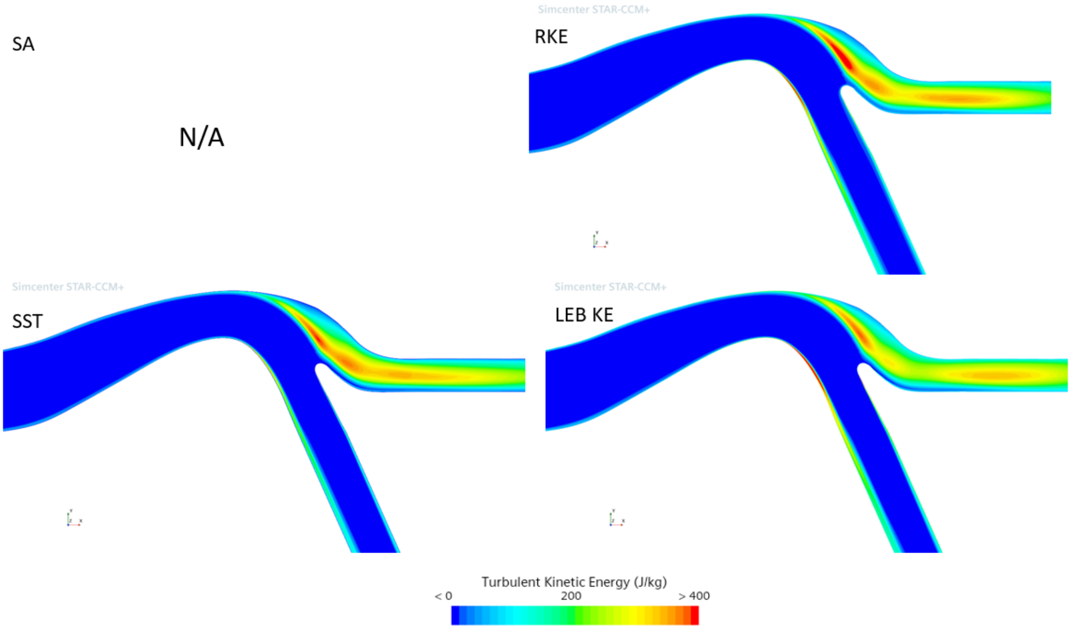

Figure 3.8. Turbulent kinetic energy contours for different turbulence models

As shown in Figure 3.8, turbulent kinetic energy of the flow becomes maximum in front of the scavenge channel for all of the turbulence models. It shows that the higher velocity fluctuations occur at this region. Another region where high turbulent kinetic energy is observed is the region after hump. At this region, flow starts to separate and this separation creates turbulence. As all of the turbulence models resulted with similar flow-field in terms of turbulent kinetic energy, SST and RKE estimates it a little bit higher than the LEB KE turbulence model.

Root mean squared error of the each turbulence model is shown in Figure 3.9.

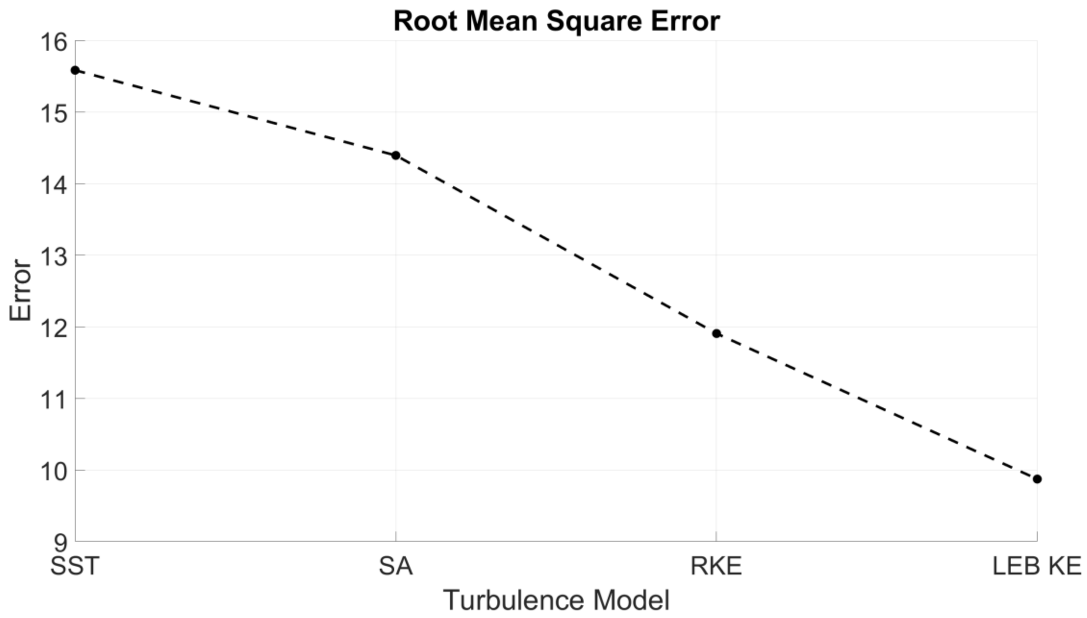

Figure 3.9. Root mean squared error of each turbulence model.

According to the Figure 3.9, results of SA, RKE and LEB KE models are improved 7.6%, 23.4% and 36.5% according to SST model, respectively.

Fine Tuning Study:

The best-resulted turbulence model is found as LEB KE in the turbulence study for 2-D IPS problem which consists of high adverse pressure gradient. LEB KE turbulence model estimates the solution with reduced error. However, this level of error is still high for a CFD analysis. Therefore, a fine-tuning study for LEB KE turbulence model is performed to enhance the solution. For this purpose, four closure coefficients are investigated within several ranges.

At the beginning, preliminary analyses, which are given in Table 3.2, are performed to see the effect of each closure coefficients on the result. First, velocity profiles are compared for each closure coefficients and results are presented in Figure 3.10.

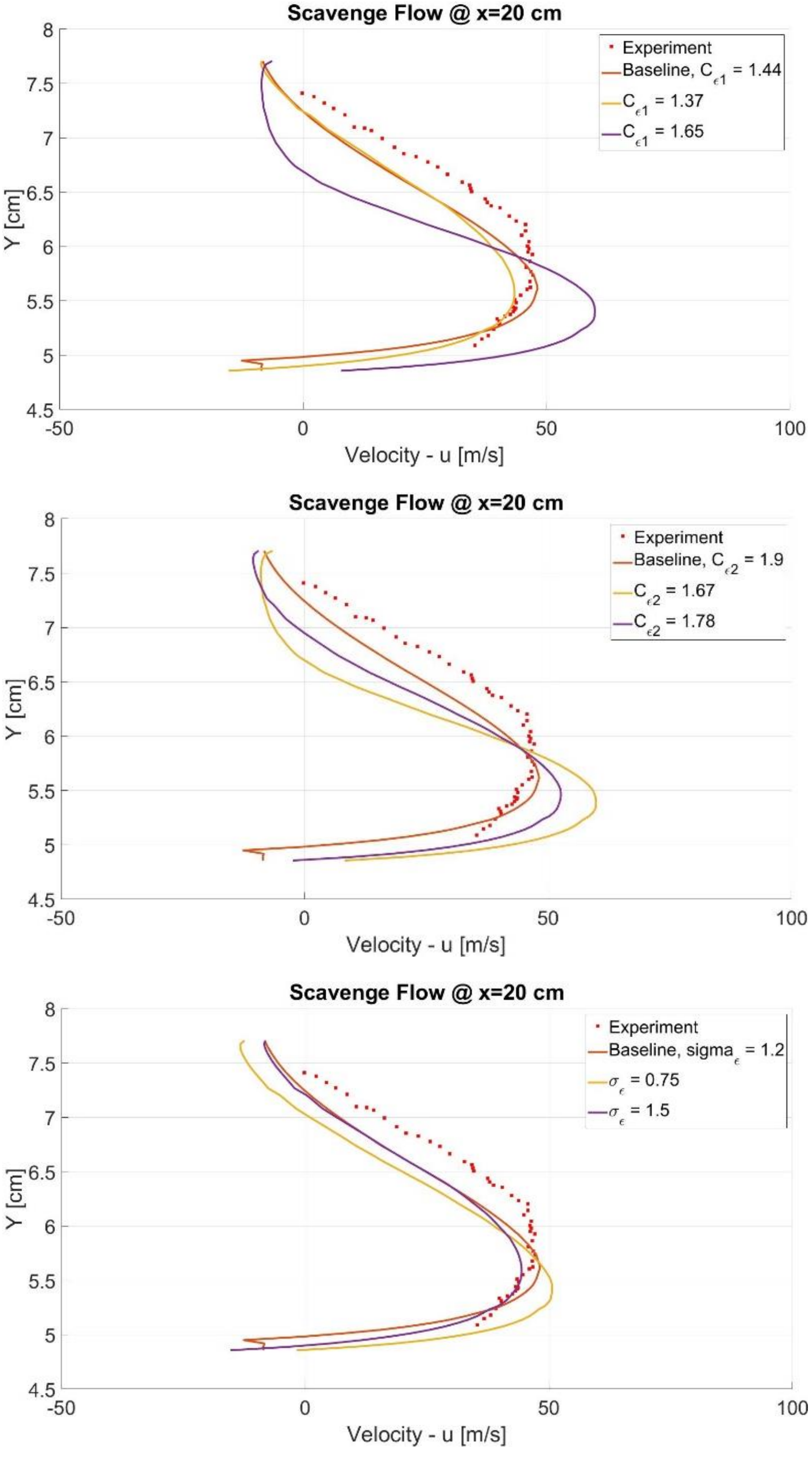

Figure 3.10. Velocity profile results of the preliminary analyses.

According to Figure 3.10, as $C_{\varepsilon 1}$ increases, velocity outside the recirculation zone increases, but recirculation region remains the same. If $C_{\varepsilon 1}$ increases more, recirculation region grows and velocity increases gradually. As velocity increase can be explained due to the decrease in effective flow area, growth in the recirculation zone can be explained due to the decrease in turbulence production. According to the Eq. 58-59, as $C_{\varepsilon 1}$ increases, production to dissipation term decreases. Hence, turbulence production decreases or turbulence dissipation increases. On the other hand, $C_{\varepsilon 2}$ is proportional to the turbulence production. As $C_{\varepsilon 2}$ increases, the opposite situations occur. However, it is important to note that $C_{\varepsilon 2}$ affects the velocity profile linearly but $C_{\varepsilon 1}$ does not. The last closure coefficient σ_ε shows similar characteristics on velocity profile with $C_{\varepsilon 1}$. Calibration of σ_ε is performed with log-layer calculations and σ_ε is inversely proportional to $(C_{\varepsilon 2} - C_{\varepsilon 1})$ parameter. As σ_ε increases, the difference decreases; hence, the similar results can be observed with the increase of $C_{\varepsilon 1}$. It is easy to see that σ_ε variation affects the velocity profile less than other two closure coefficients and $C_{\varepsilon 1}$ has bigger impact on the result than $C_{\varepsilon 2}$.

As mentioned in the previous paragraph, as $C_{\varepsilon 1}$ increases, the turbulence production decreases. When the turbulence decreases, friction between the air molecules and the wall increases. Hence, turbulent viscosity increases. The opposite situation is valid for $C_{\varepsilon 2}$. This situation can be seen from Figure 3.11, which shows turbulent viscosity ratio results of the preliminary analyses.

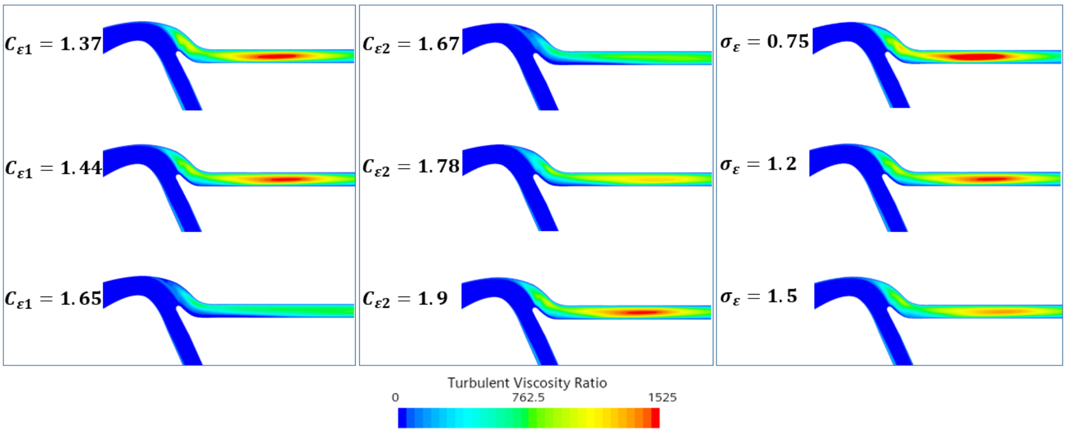

Figure 3.11. Turbulent viscosity ratio results of the preliminary analyses.

Some comments on the size of the recirculation region are made in terms of height in the previous paragraphs. However, the length is another important parameter for recirculation region. Streamlines of the IPS flow are presented in Figure 3.12 to examine the recirculation region.

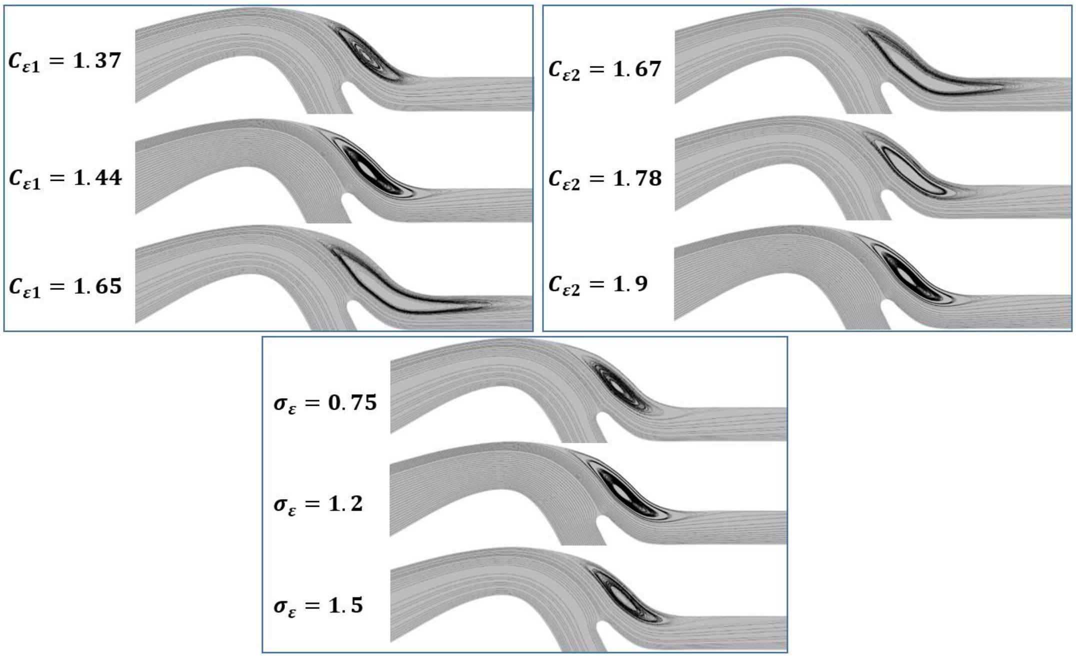

Figure 3.12. Streamlines of the IPS flow-field for the preliminary analyses.

As it can be seen from the Figure 3.12, length of the recirculation region enlarges in axial direction as $C_{\varepsilon 1}$ increases and as $C_{\varepsilon 2}$ decreases. This kind of separation is not observed in experimental results or simulation results given in Chapter 2. Modification of σ_{ε} again shows similar characteristics with $C_{\varepsilon 1}$ modification, however its effect is negligible when compared with results of $C_{\varepsilon 1}$ modification. At the end, it is deduced that decreasing the $C_{\varepsilon 1}$ and increasing the $C_{\varepsilon 2}$ provide smaller error.

In the most of the previous studies unlike this work, these closure coefficients are modified one by one. In the further part of this study, combination of these closure coefficients are analyzed within an optimization process by using HEEDS MDO software. In total, 100 analyses are performed. As 86 analyses were successfully ended, 13 of them diverged. Just one of the analyses were found as unfeasible due to β constraint. At the end, HEEDS found the best result at the 36th option. The new closure coefficients are presented with the baseline values in Table 3.3.

Table 3.3. New closure coefficients

	$C_{\varepsilon 1}$	$C_{\varepsilon 2}$	σ_k	σ_ε
Design 36	**1.37**	**1.91**	**0.8**	**1.5**
Baseline	1.44	1.9	1	1.2

Percentage error with respect to baseline results are plotted for closure coefficient variation for each coefficient in Figure 3.13-3.16 with the baseline turbulence model, modified turbulence model (Case 36) and trend line.

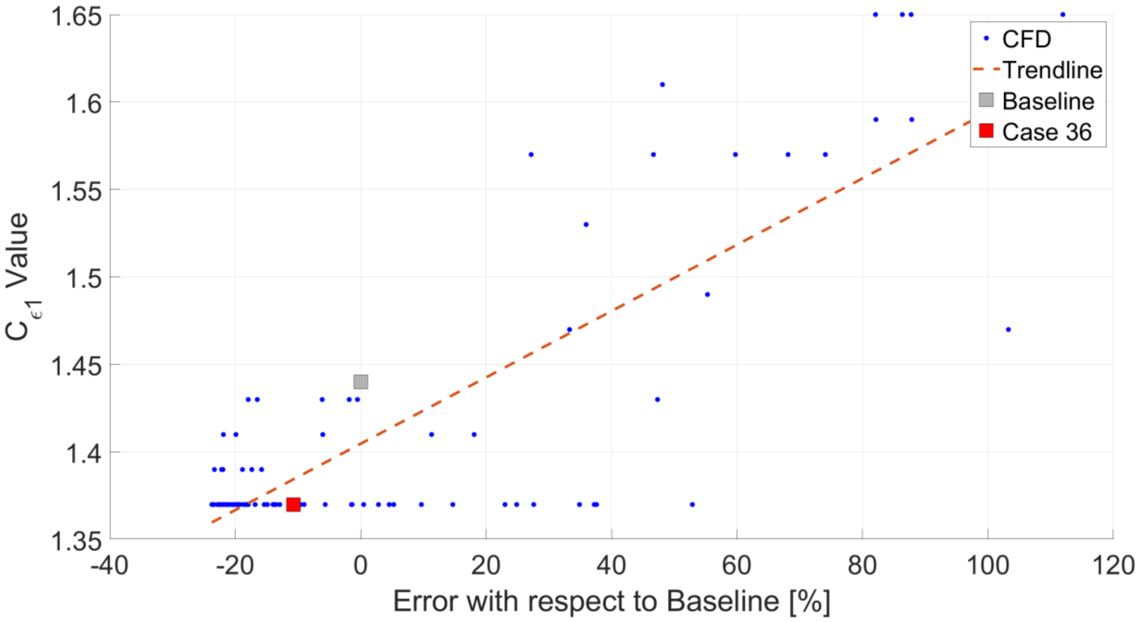

Figure 3.13. Percentage error with respect to baseline vs. $C_{\varepsilon 1}$

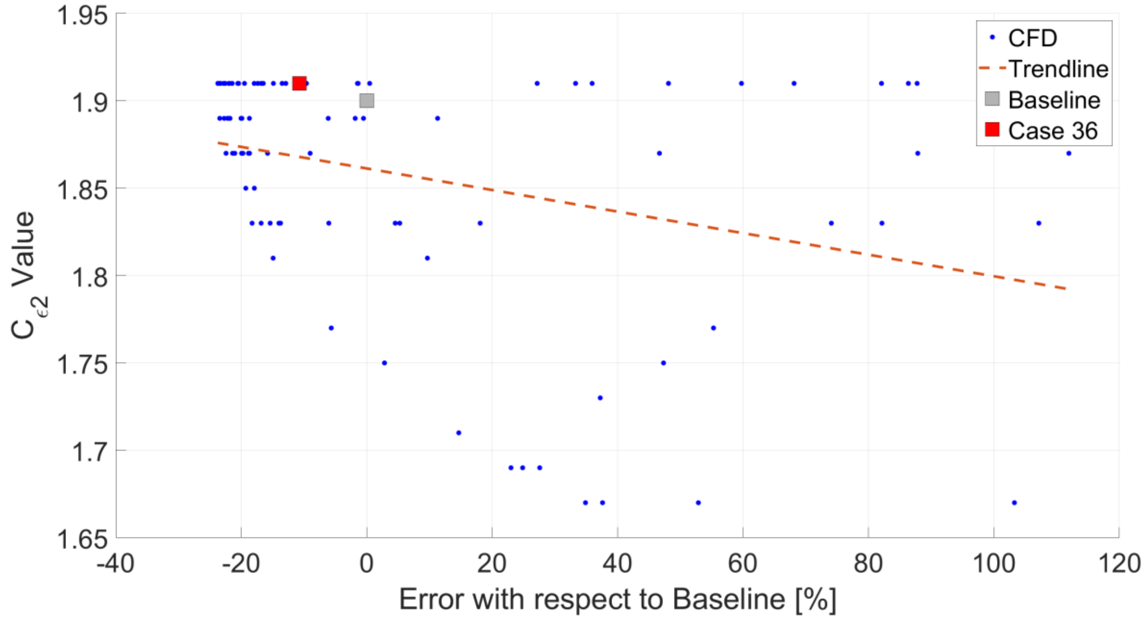

Figure 3.14. Percentage error with respect to baseline vs. $C_{\varepsilon 2}$

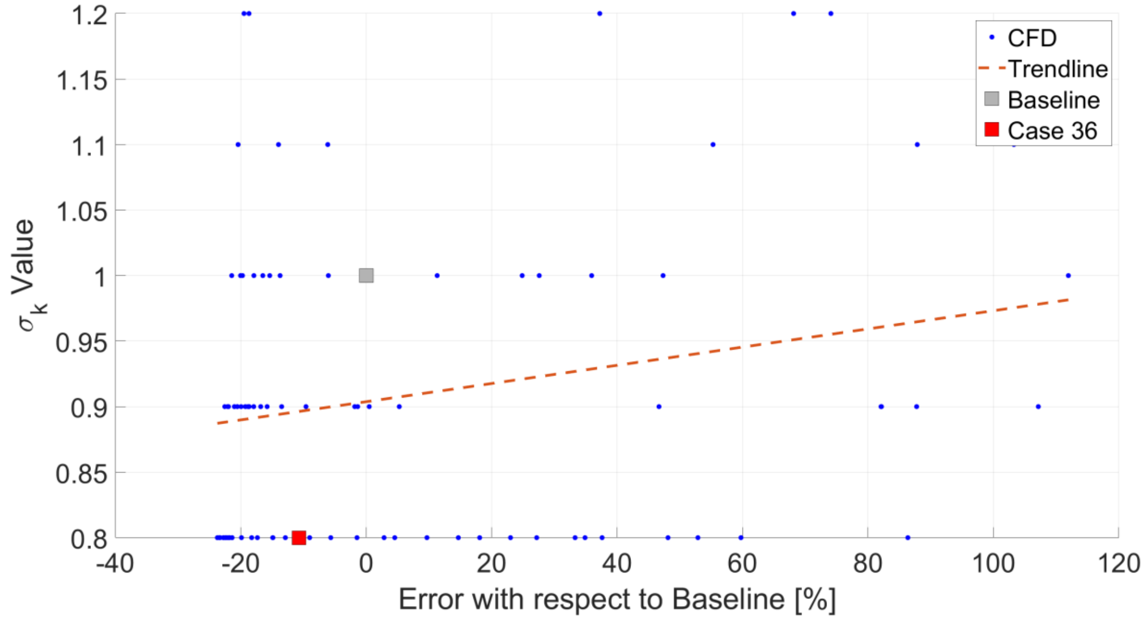

Figure 3.15. Percentage error with respect to baseline vs. σ_k

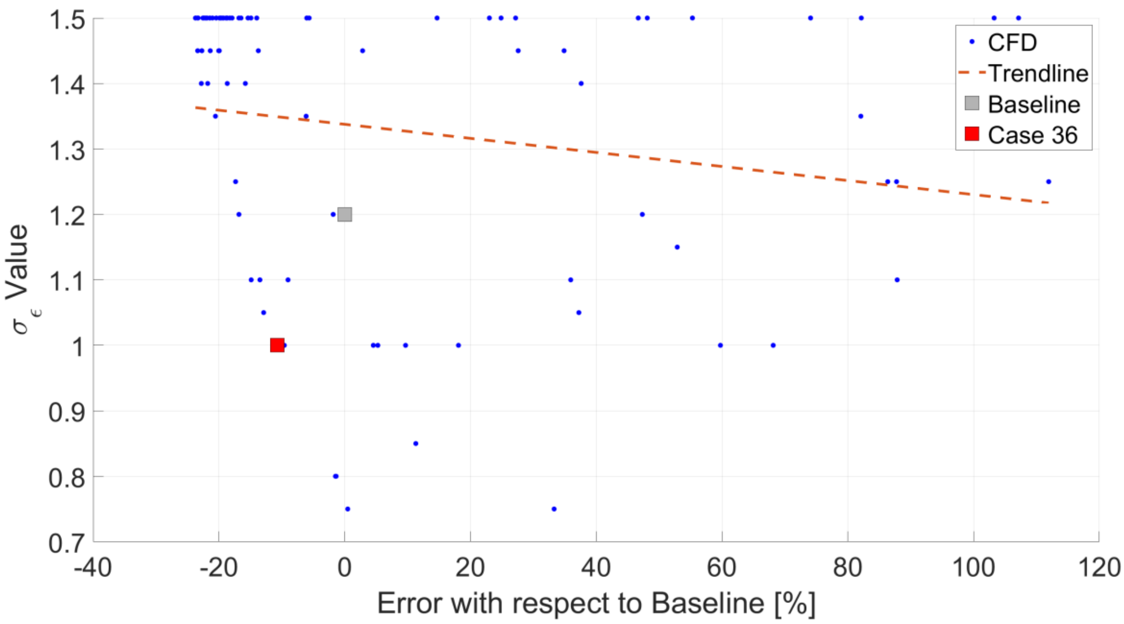

Figure 3.16. Percentage error with respect to baseline vs. σ_ε

In Figure 3.13-3.16, the slope of the trend line shows how much the closure coefficient variation affects the results. The slope of the $C_{\varepsilon 1}$, $C_{\varepsilon 2}$, σ_k and σ_ε are 0.83, -0.33, 0.22 and -0.18, respectively. As the most critical closure coefficient is determined as $C_{\varepsilon 1}$ for 2-D IPS solution, the least significant closure coefficient is found as σ_ε unlike literature.

Some improvement is gained at the end of the fine-tuning study for this problem. The comparison of the velocity profile at the scavenge leg is illustrated in Figure 3.17 for both original and modified turbulence model.

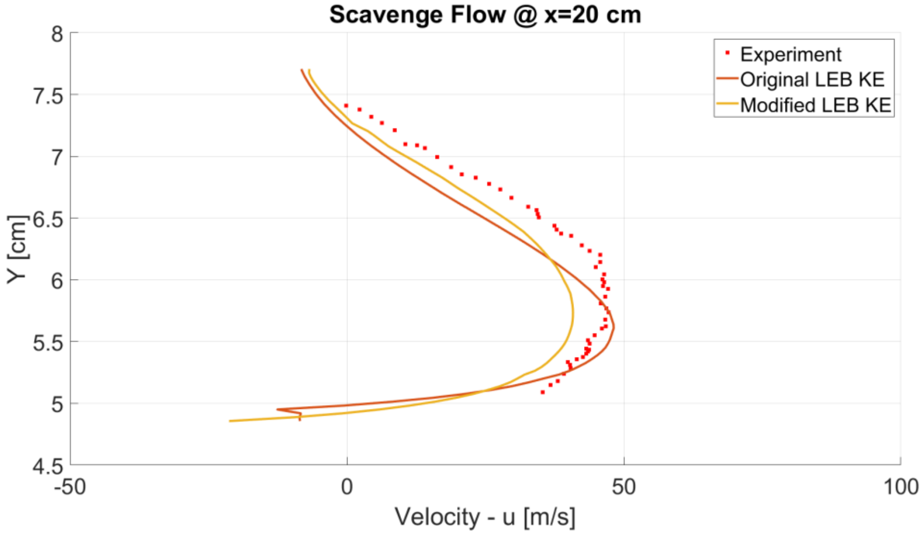

Figure 3.17. Velocity profiles at the scavenge leg for original and modified turbulence model.

As shown in Figure 3.17, velocity profile of the original model at the scavenge leg overestimates the mean experimental velocity profile around y=5.5 cm and underestimates at the rest of the regions. The modified turbulence model predicts the shape of the velocity profile better than the original turbulence model. It has almost the same profile with a small shift. As error of the new turbulence model is higher around y=5.5 cm, it is smaller at all other regions.

Moreover, flow-field is investigated in terms of velocity, turbulent viscosity ratio and turbulent kinetic energy. Velocity contour of the original turbulence model and its difference with the modified turbulence model are shown in Figure 3.18. Velocity difference is given with different color bar due to the same reason defined in Figure 3.5.

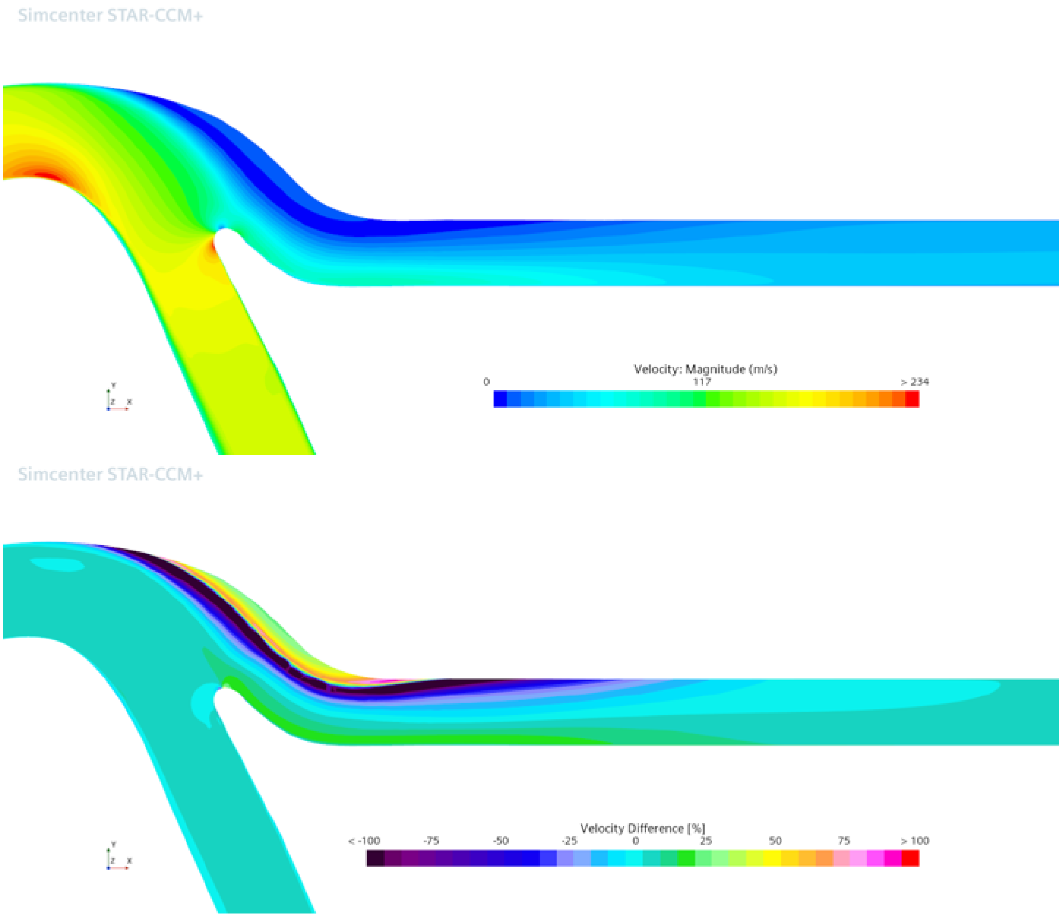

Figure 3.18. Velocity contour of the original turbulence model and velocity difference contours according to the modified turbulence model

Figure 3.18 shows the velocity differences between original model and modified model. The positive values mean velocity decrease in the modified model. Velocity is the same for most of the regions. However, it differs in the recirculation zone and scavenge channel. Velocity decreased in the scavenge flow can also be seen from the green zones on the splitter.

Streamlines are also investigated to see how closure coefficients affect the flow characteristics around the bifurcation zone and it is illustrated in Figure 3.19.

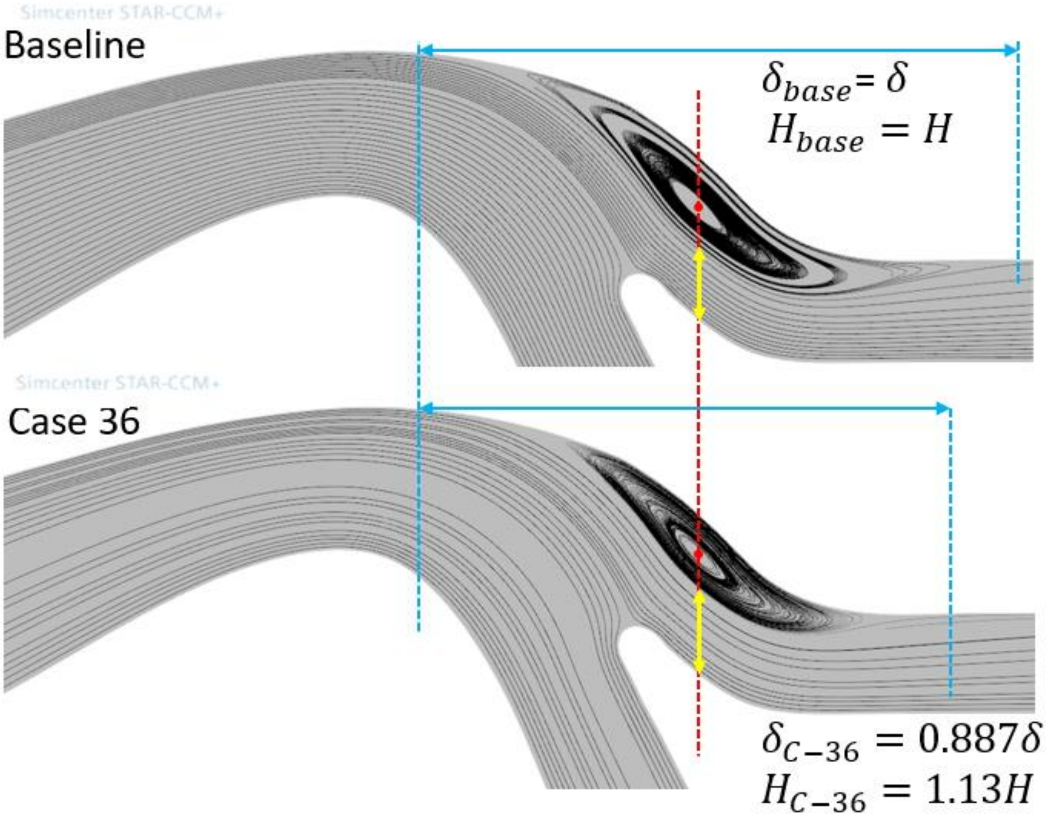

Figure 3.19. Streamlines around the bifurcation region for baseline and modified turbulence model.

As it can be seen in Figure 3.16, center of the recirculation does not change at all in axial direction; however, height of the recirculation decreases. As scavenge flow height of the baseline turbulence model is taken as reference, the scavenge flow height increases 13% for the modified turbulence model. Reattachment length of the flow is also shown in the same figure with blue arrow. As the baseline turbulence model is taken as reference, the reattachment length decreases 12% for the modified turbulence model.

Moreover, turbulent viscosity ratio is examined in the flow-field. Turbulent viscosity ratio contour is presented for both baseline and modified turbulence models in Figure 3.20.

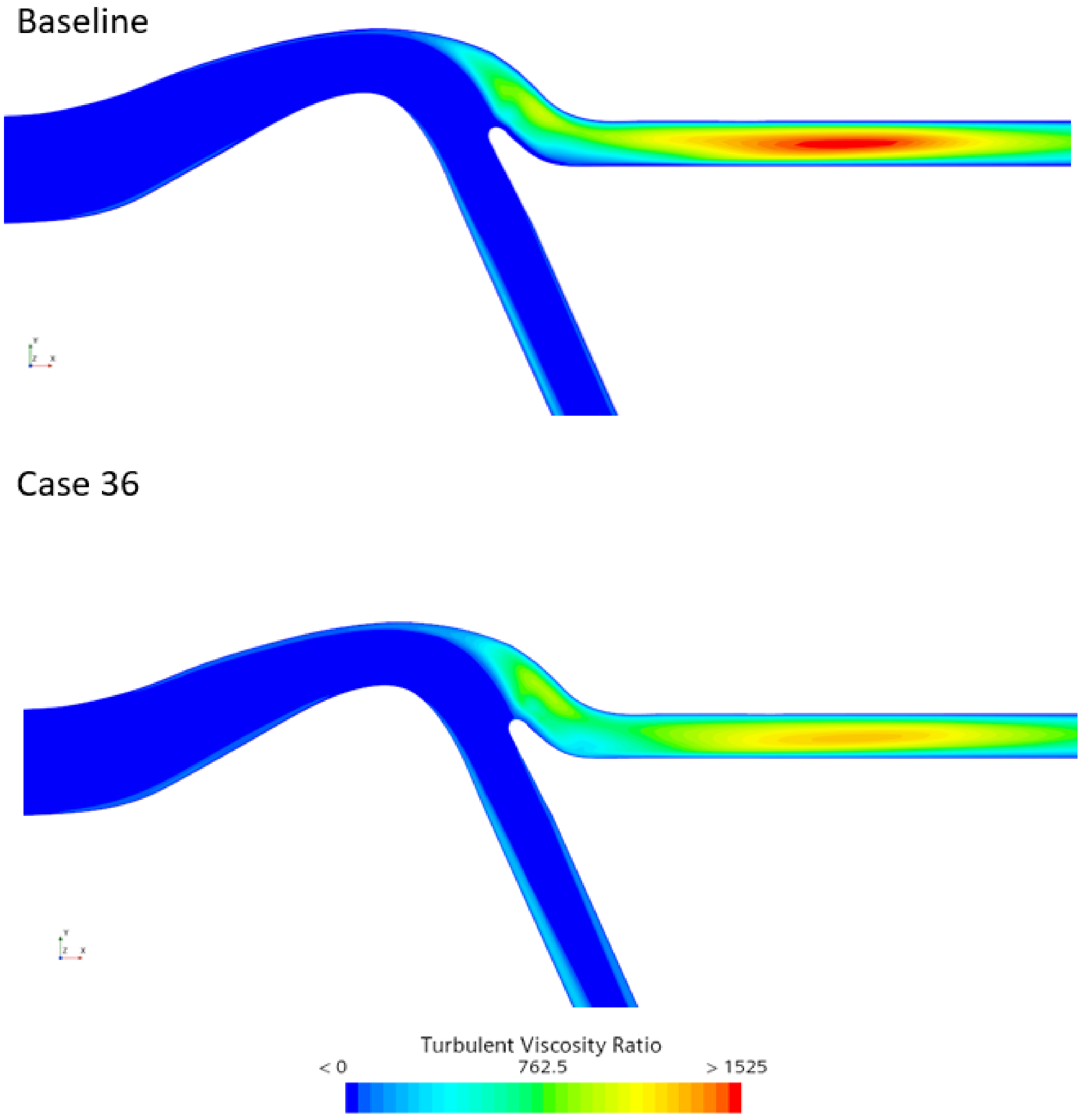

Figure 3.20. Turbulent viscosity ratio contours for baseline and modified turbulence models

According to the Figure 3.20, both turbulence models estimate the zero turbulent viscosity ratio for similar regions. The largest difference is observed in the scavenge channel. Turbulent viscosity ratio is lower for most of the regions in the scavenge channel for new turbulence model.

Turbulent kinetic energy contour is also presented in Figure 3.21 for both turbulence models. Similar characteristics are observed with the turbulence viscosity ratio.

Turbulent kinetic energy is decreased for new model at the entrance and inside of the scavenge duct. Velocity difference contour shows parallel results with turbulent kinetic energy contour where less turbulent kinetic energy equivalent to the low velocity fluctuation.

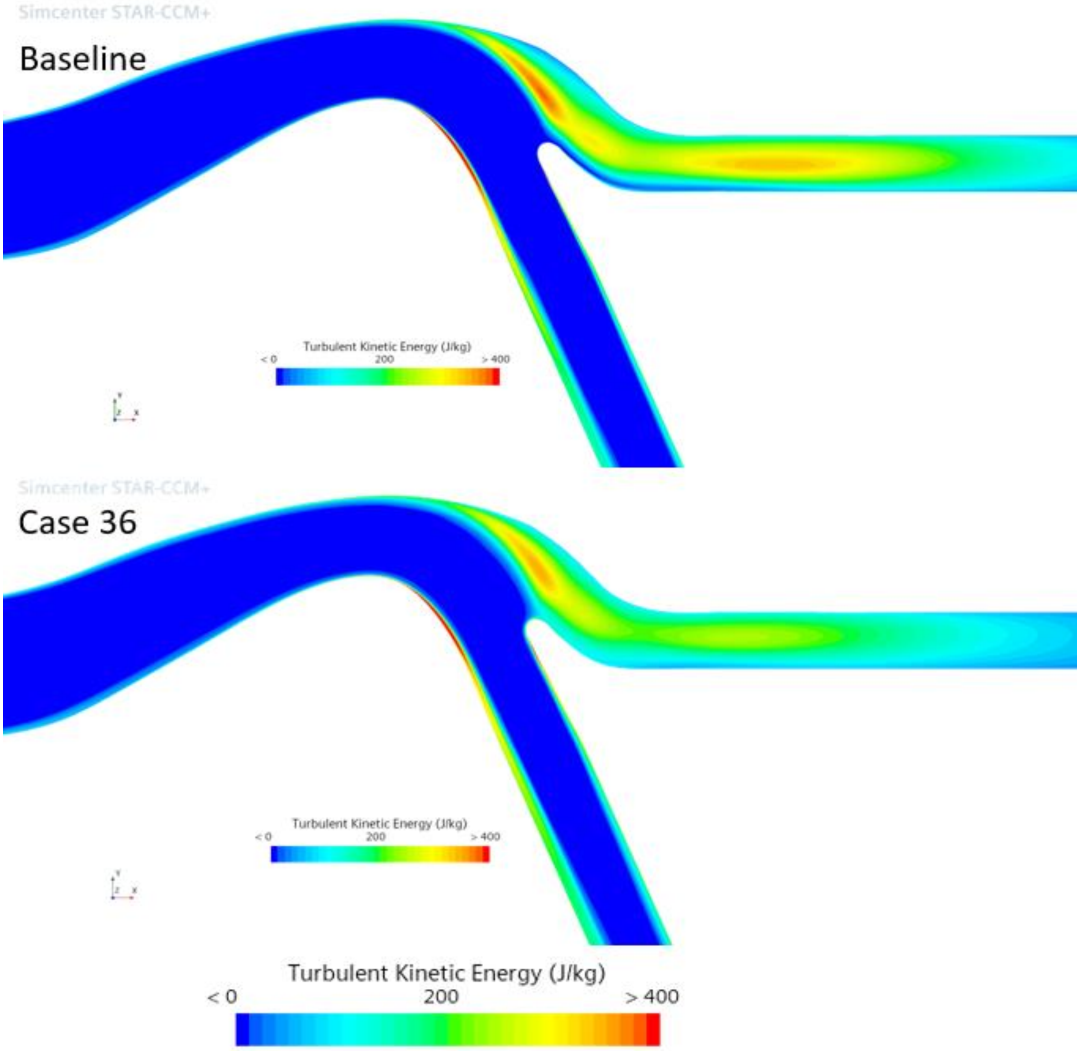

Figure 3.21. Turbulent kinetic energy contours for baseline and modified turbulence models

Root mean squared error of the modified turbulence model is presented in Figure 3.22. Root mean squared error of the modified turbulence model is reduced from 10 to 7.64, which brings 24% improvement.

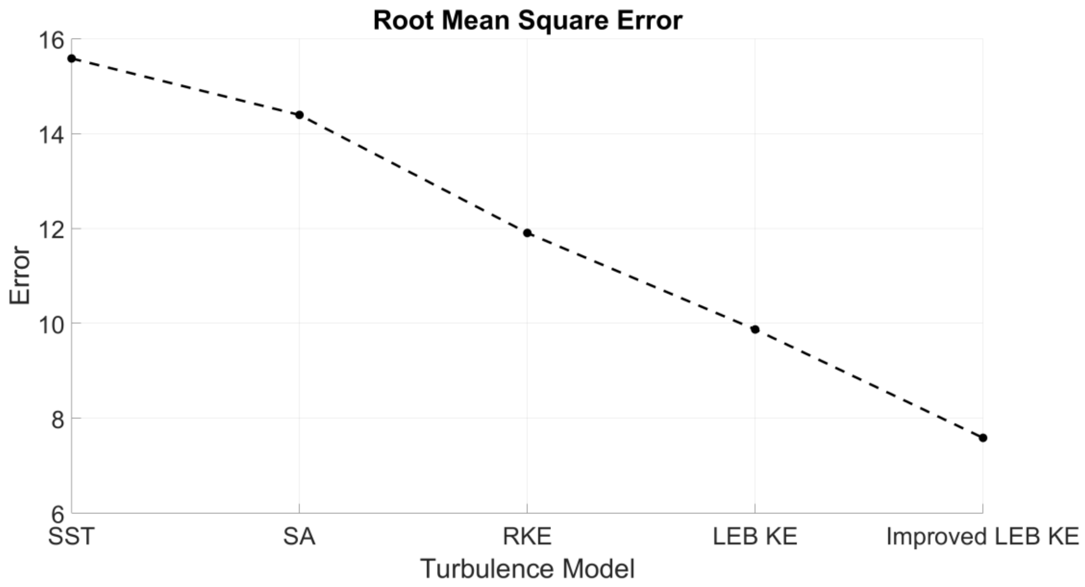

Figure 3.22. Root mean squared error of all turbulence models.

3.4 Conclusion

In this study, SA, SST, RKE and LEB KE turbulence models are investigated for 2-D IPS analysis and results are compared with the experiment in terms of mean velocity profile at the scavenge channel. The best-resulted turbulence model is found as LEB KE turbulence model. SST and SA resulted with the largest error, which is approximately 8% higher than LEB KE error. Each turbulence model uses several closure coefficients, which are determined by previous experiments or by using assumptions that are not valid for every problem type. For this reason, a sensitivity study is performed to calibrate these closure coefficients according to 2-D IPS problem. $C_{\varepsilon 1}, C_{\varepsilon 2}, \sigma_k$ and σ_ε closure coefficients are examined in this study. Their ranges are determined and preliminary analysis are performed. Preliminary study shows that minimizing the $C_{\varepsilon 1}$ and maximizing the $C_{\varepsilon 2}$ provide better accuracy. σ_ε shows similar trend with the $C_{\varepsilon 2}$; however, σ_ε modification has less effect on the results than $C_{\varepsilon 2}$ modification. After that, an optimization study is performed by using the Siemens HEEDS MDO software. Closure coefficients are used as design variables in the optimization software and objective function, which defines the error between the velocity profiles of CFD and experiment, is minimized. At the end, a set of closure coefficients given in Table 3.3 are obtained as the best fit. Final improvement is found as 24% according to baseline turbulence model. Modification of these closure coefficients sometimes affect the stability, hence the duration of the analysis. However, durations are already too short due to two-dimensional approach. Output of these modifications improves accuracy without any disadvantage.

CHAPTER 4

CONCLUSION

The main purpose of this thesis is to gain broader perspective for IPS simulations. It is determined that turbulence model is a very important phenomenon for not only flow analysis, but also for particle analysis. RANS based turbulence models are still very effective, cheap and suitable for internal flows in the preliminary design phase. However, higher accuracy methods like DES/LES are the only options except experiment or test in the later design phases, which requires more details about the flow. Two studies are performed for IPS with RANS based turbulence models and IDDES turbulence model.

At the first study, one of the intake design parameter, which is known as swirl, is investigated in terms of IPS performance. Axisymmetric 3-D IPS is analyzed with the method that provides the most accurate results in the literature for the first time. It is proved that swirling flow formed at the intake has a positive impact on the separation efficiency at low β. Separation efficiency of AC Coarse dust is increased 4% for $\beta=0.1$ condition. Swirling flow effect on separation efficiency depreciates with the increase of β. This study requires high amount of computation power due to the unsteady approach and scale-resolving turbulence model. However, this amount of computational power may not available or this kind of accuracy may not be required. In these type of situations, RANS methods or even 2-D approach can be used for IPS analysis.

At the second study, RANS turbulence models are examined with 2-D IPS model in terms of accuracy. LEB KE turbulence model is found as the most accurate model for this problem, but there is still some amount of error when compared to the experimental data. A fine-tuning study, which is lately become popular, is performed for 2-D IPS model. In this study, modified LEB KE turbulence model performed

24% better results than the baseline LEB KE model. As $C_{\varepsilon 1}$ modifiacaiton is found as the most influential parameter for IPS flow, σ_{ε} modification has minor effect on the solution. A fine-tuning study is performed for the first time for LEB KE turbulence model and IPS problem.

As the flow analysis of the first study, which is performed in a HPC cluster, takes 26 hours with 400 CPU cores (10,400 core hours) for one β condition, the flow analysis of the second study, which is performed in a workstation with a single CPU, takes only 30 minutes with 2 CPU cores (1 core hour). The second study is almost 10,000 times cheaper than the first study and this situation shows that RANS methods are life-saving in CFD world. In spite of the fact that DES/LES methods are so expensive, they are required in the later phases of a design study.

Separation efficiency is one of the most important parameter for engine life. Since, performing an experiment or a test is an expensive and time consuming process, determining the separation efficiency with high accuracy via analysis save huge amount of time and money. More specific examples about separation efficiency are:

- Any improvement in the IPS separation efficiency, reduces the engine deterioration hence, decreases specific fuel consumption (SFC) at the same power level. This shows that increasing separation efficiency reduces the CO_2 emissions which is beneficial for the environment.

- Maintenance and inspection intervals of the several engine sections depend on the IPS separation efficiency. Keeping the time between inspections/maintenance operations shorter brings loss of time, supplies and money. However, keeping it longer may result with loss of equipment or even loss of aircraft.

CHAPTER 5

FUTURE WORK

In the future, the following studies might be beneficial for engine industry, helicopter manufacturers and environment:

- Axisymmetric IPS model, which is more likely to demonstrate a real engine IPS, can be experimentally investigated and present more accurate evidences about IPS flow-field and separation efficiency.
- A newly created set of closure coefficients in this study can be used for 3-D IPS analysis to check whether flow-field and separation efficiency results are also improved for 3-D geometry or not.
- A particle analysis can be performed for both baseline and modified turbulence models to check how separation efficiency is affected with 2-D IPS model.
- There are lots of studies investigating the compressor blade deformation due to FOD ingestion by intake. However, ingested particles also deform the IPS itself. This deformation can be examined in terms of engine deterioration and separation efficiency.

REFERENCES

[1] Head E., What it's like flying the CH-53K helicopter into a brownout. Vertical Mag. (n.d.). Retrieved December 12, 2021, from https://verticalmag.com/news/flying-ch-53k-helicopter-into-brownout.

[2] J. P. V. D. Van Der Walt and A. Nurick, Erosion of dust-filtered helicopter turbine engines part i: Basic theoretical considerations, Journal of Aircraft, vol. 32, pp. 106–111, Jan. 1995.

[3] Witek, L., Bednarz, A., & Stachowicz, F. 2015. Fatigue analysis of compressor blade with simulated foreign object damage. Engineering Failure Analysis, 58, 229–237.

[4] Bojdo, N.M. (2012). Rotorcraft Engine Air Particle Separation. [Doctoral dissertation, University of Virginia].

[5] Potts, J. T. 1990. Why an engine air particle separator (EAPS)? Volume 2: Aircraft Engine; Marine; Microturbines and Small Turbomachinery.

[6] Pall Aerospace, Pall Pureair Introduction. Retrieved October 12, 2022, from https://www.pall.com/ content/dam/pall/aerospace-defense/literature-library

[7] Helicopter engines and operational impact in Harsh Environments. (2019, December 20). Retrieved December 19, 2021, from https://aviationweek.com/knowledge-center/helicopter-engines-operational-impact-harsh-environments.

[8] Bojdo, N., Filippone, A. (2014). Comparative study of helicopter engine particle separators. Journal of Aircraft, 51(3), 1030-1042. doi:10.2514/1.c032322

[9] Appadvice. (2019, June 13). Donaldson IBF by PerspectX Studios. Retrieved December 26, 2021, from https://appadvice.com/app/donaldson-ibf/599200238

[10] Bainbridge, R. (2019, June 17). Donaldson celebrates the success of its new IBF. Retrieved January 01, 2022, from https://www.airmedandrescue.com/latest/news/donaldson-celebrates-success-its-new-ibf

[11] Donaldson Company, Inc., Aerospace Defense Group. (2016). ROTORCRAFT ENGINE INLET BARRIER FILTER SYSTEMS for MILITARY AIRCRAFT [Brochure].

[12] Barone, D., Loth, E., & Snyder, P. 2012. A 2-D inertial particle separator research facility. 28th Aerodynamic Measurement Technology, Ground Testing, and Flight Testing Conference.

[13] Connolly, B. J. (2020). Inertial Particle Separators Experiments, Simulations, and Design Insights. [Doctoral dissertation, University of Virginia].

[14] Vittal, B. R. (1988). A design system for erosion tolerant helicopter engines. Journal of the American Helicopter Society, 33(1), 47–54. https://doi.org/10.4050/jahs.33.1.47

[15] Barone, D. L., Hawkins, J., Loth, E., Snyder, P. H. (2013). Inertial particle separator efficiency using spherical particles. 49th AIAA/ASME/SAE/ASEE Joint Propulsion Conference. https://doi.org/10.2514/6.2013-3666

[16] Barone, D., Loth, E., Snyder, P. H. (2014). Particle Dynamics of a 2-D inertial particle separator. Volume 1A: Aircraft Engine; Fans and Blowers. https://doi.org/10.1115/gt2014-26922

[17] Barone, D., Loth, E., Snyder, P. (2013). Efficiency of an inertial particle separator. 51st AIAA Aerospace Sciences Meeting Including the New Horizons Forum and Aerospace Exposition. https://doi.org/10.2514/6.2013-1080

[18] Barone, D., Loth, E., Snyder, P. (2017). Influence of particle size on inertial particle separator efficiency. Powder Technology, 318, 177–185. https://doi.org/10.1016/j.powtec.2017.04.044

[19] Snyder, P. H., Barone, D., & Loth, E. (2015). Unsteady flow dynamics within an inertial particle separator. Volume 1: Aircraft Engine; Fans and Blowers; Marine. https://doi.org/10.1115/gt2015-43783

[20] Barone, D. 2014. Inertial Particle Separator Multiphase Dynamics. [Doctoral dissertation, University of Virginia].

[21] Barone, D. L., Loth, E., & Snyder, P. H. 2014. Fluid dynamics of an inertial particle separator. 52nd Aerospace Sciences Meeting.

[22] Connolly, B. J. 2020. Inertial Particle Separators Experiments, Simulations, and Design Insights. [Doctoral dissertation, University of Virginia].

[23] Connolly, B. J., Loth, E., & Smth, C. F. 2019. Unsteady simulation of an inertial particle separator. AIAA Propulsion and Energy 2019 Forum.

[24] Connolly, B. J. 2016. A Parametric Study of Inertial Particle Separator Geometry. [Master’s thesis, University of Virginia].

[25] Goss, C. M., Connolly, B. J., Loth, E., & Smth, C. F. 2019. Scaling effects on inertial particle separator performance. AIAA Propulsion and Energy 2019 Forum.

[26] Connolly, B. J., Loth, E., & Frederic Smith, C. 2022. Unsteady separated flows in an S-duct and a bifurcating duct. Journal of Aircraft, 59(1), 47–57.

[27] Chen, H., Tan, H.-jun, Yuan, Y.-qing, Du, M.-chen, & Xie, M.-xiang. 2017. Separated flows in bifurcated region of a vaneless inertial particle separator. Journal of Aircraft, 54(3), 1234–1237

[28] Paoli, F., & Wang, T. 2011. Numerical Study of internal flow field and flow passage improvement of an inlet particle separator. Frontiers in Energy.

[29] Hamed, A. 1982. Particle dynamics of inlet flowfields with swirling vanes. Journal of Aircraft, 19(9), 707–712.

[30] Hamed, A., Jun, Y., & Yeuan, J. 1993. Particle dynamics simulations in inlet separator with an experimentally based bounce model. 29th Joint Propulsion Conference and Exhibit.

[31] Ghenaiet, A., & Tan, S. C. 2004. Numerical study of an inlet particle separator. Volume 2: Turbo Expo 2004

[32] Taslim, M. E., Khanicheh, A., & Spring, S. 2009. A numerical study of sand separation applicable to engine inlet particle separator systems. Journal of the American Helicopter Society, 54(4), 042001.

[33] Taslim, M. E., & Spring, S. 2010. A numerical study of sand particle distribution, density, and shape effects on the scavenge efficiency of engine inlet particle separator systems. Journal of the American Helicopter Society, 55(2), 22006–220069.

[34] Smith, C. F. (2010). Six sigma methods applied to an inlet particle separator design. 13th AIAA/ISSMO Multidisciplinary Analysis Optimization Conference. https://doi.org/10.2514/6.2010-9398

[35] Jiang, L. Y., Benner, M., & Bird, J. 2012. Assessment of scavenge efficiency for a helicopter particle separation system. Journal of the American Helicopter Society, 57(2), 41–48

[36] Zhang, K.-ke, Hu, H.-yang, Wang, Q. (2015). Simulation of gas-solid flow in inlet particle separator on probabilistic restitution model. Proceedings of the 2015 International Forum on Energy, Environment Science and Materials. https://doi.org/10.2991/ifeesm-15.2015.121

[37] Chen, N., Du, J., Hu, Y., Ji, H., & Yuan, Y. 2020. Study of the flow and impingement of water droplets inside an inertial particle separator. AIP Advances, 10(4), 045313.

[38] Siemens Industries Digital Software. 2021. Simcenter STAR-CCM+ User Guide, version 2021.3. Turbulence.

[39] ISO 12103-1. 2016. Road Vehicles -- Test Contaminants for Filter Evaluation -- Part 1: Arizona Test Dust

[40] Tabakoff, W., Murugan, D., & Hamed, A. 1994. Effect of target materials on the particle restitution characteristics for turbomachinery application. 32nd Aerospace Sciences Meeting and Exhibit.

[41] Tabakoff, W., Malak, M., & Hamed, A. 1985. Laser measurements of solid particles rebound parameters impacting on 2024 aluminum and 6A1-4V titanium alloys. 18th Fluid Dynamics and Plasma dynamics and Lasers Conference.

[42] S-16 Turbine Engine Inlet Flow Distortion Committee. (2022). A methodology for Assessing Inlet Swirl Distortion. https://doi.org/10.4271/air5686

[43] Narjisse, A., Abdellatif, K. (2021). Assessment of RANS turbulence closure models for predicting airflow in neutral ABL over hilly terrain. International Review of Applied Sciences and Engineering, 12(3), 238–256. https://doi.org/10.1556/1848.2021.00264

[44] Bounds, C. P., Zhang, C., & Uddin, M. (2020). Improved CFD prediction of flows past simplified and real-life automotive bodies using modified turbulence model closure coefficients. Proceedings of the Institution of Mechanical Engineers, Part D: Journal of Automobile Engineering, 234(10-11), 2522–2545. https://doi.org/10.1177/0954407020916671

[45] Fu, C., Bounds, C., Uddin, M., Selent, C. (2019). Fine tuning the SST $k - \omega$ turbulence model closure coefficients for improved NASCAR Cup racecar aerodynamic predictions. SAE International Journal of Advances and Current Practices in Mobility, 1(3), 1226–1232. https://doi.org/10.4271/2019-01-0641

[46] Da Ronch, A., Panzeri, M., Drofelnik, J., d'Ippolito, R. (2019). Sensitivity and calibration of turbulence model in the presence of epistemic uncertainties. CEAS Aeronautical Journal, 11(1), 33–47. https://doi.org/10.1007/s13272-019-00389-y

[47] Taghizadeh, S., Witherden, F. D., Girimaji, S. S. (2020). Turbulence closure modeling with data-driven techniques: Physical compatibility and consistency considerations. New Journal of Physics, 22(9), 093023. https://doi.org/10.1088/1367-2630/abadb3

[48] Shirzadi, M., Mirzaei, P. A., Naghashzadegan, M. (2017). Improvement of K-epsilon turbulence model for CFD simulation of atmospheric boundary layer around a high-rise building using stochastic optimization and Monte Carlo Sampling Technique. Journal of Wind Engineering and Industrial Aerodynamics, 171, 366–379. https://doi.org/10.1016/j.jweia.2017.10.005

[49] Erb, A., Hosder, S. (2021). Analysis and comparison of turbulence model coefficient uncertainty for canonical flow problems. Computers Fluids, 227, 105027. https://doi.org/10.1016/j.compfluid.2021.105027

[50] Stefano, M. A. D. (2020). Effect of turbulence model closure coefficient uncertainty on scramjet flow field analysis. [Doctoral dissertation, University of Virginia].

[51] Fu, C., Uddin, M., Robinson, C., Guzman, A., Bailey, D. (2017). Turbulence models and model closure coefficients sensitivity of NASCAR racecar rans CFD aerodynamic predictions. SAE International Journal of Passenger Cars - Mechanical Systems, 10(1), 330–344. https://doi.org/10.4271/2017-01-1547

[52] SPALART, P., ALLMARAS, S. (1992). A one-equation turbulence model for aerodynamic flows. 30th Aerospace Sciences Meeting and Exhibit. https://doi.org/10.2514/6.1992-439

[53] Shih, T.-H., Liou, W. W., Shabbir, A., Yang, Z., Zhu, J. (1995). A new K-ϵ Eddy viscosity model for high reynolds number turbulent flows. Computers Fluids, 24(3), 227–238. https://doi.org/10.1016/0045-7930(94)00032-t

[54] Jones, W. P., Launder, B. E. (1972). The prediction of laminarization with a two-equation model of turbulence. International Journal of Heat and Mass Transfer, 15(2), 301–314. https://doi.org/10.1016/0017-9310(72)90076-2

[55] Menter, F. R. (1994). Two-equation eddy-viscosity turbulence models for engineering applications. AIAA Journal, 32(8), 1598–1605. https://doi.org/10.2514/3.12149

[56] Lardeau, S., Billard, F. (2016). Development of an elliptic-blending lag model for industrial applications. 54th AIAA Aerospace Sciences Meeting. https://doi.org/10.2514/6.2016-1600

[57] Manceau, R. (2015). Recent progress in the development of the elliptic blending Reynolds-stress model. International Journal of Heat and Fluid Flow, 51, 195–220. https://doi.org/10.1016/j.ijheatfluidflow.2014.09.002

[58] Durbin, P. A., Pettersson, R. B. A. (2011). Statistical theory and modeling for turbulent flow. Wiley.

[59] Siemens Industries Digital Software. 2021. HEEDS MDO User Guide, version 2020.1.

[60] Billard, F., Laurence, D. (2012). A robust k−ε−/k elliptic blending turbulence model applied to near-wall, separated and buoyant flows. International Journal of Heat and Fluid Flow, 33(1), 45–58. https://doi.org/10.1016/j.ijheatfluidflow.2011.11.003

[61] Billard, F., Revell, A., Craft, T. (2012). Application of recently developed elliptic blending based models to separated flows. International Journal of Heat and Fluid Flow, 35, 141–151. https://doi.org/10.1016/j.ijheatfluidflow.2012.04.012

[62] Wilcox, D. (2007). Formulation of the K-omega turbulence model revisited. 45th AIAA Aerospace Sciences Meeting and Exhibit. https://doi.org/10.2514/6.2007-1408

[63] Zhang, C. (2018). Numerical Simulation Based Analysis of road vehicle aerodynamic flows. [Doctoral dissertation, The University of North Carolina at Charlotte].

[64] Kraus, A. R., Yuan, H., Merzari, E. (2018). Evaluation of turbulence modeling approaches for cross-flow in a helical tube bundle. Volume 8: Computational Fluid Dynamics (CFD); Nuclear Education and Public Acceptance. https://doi.org/10.1115/icone26-82486

APPENDICES

A. Annular IPS Geometry